# INFLUENCE OF ROCK TYPES ON SEISMIC MONITORING OF $CO_2$ SEQUESTRATION IN CARBONATE RESERVOIRS

A Thesis

by

ELNARA MAMMADOVA

Submitted to the Office of Graduate Studies of
Texas A&M University
in partial fulfillment of the requirements for the degree of

MASTER OF SCIENCE

August 2011

Major Subject: Geology

Influence of Rock Types on Seismic Monitoring of $CO_2$

Sequestration in Carbonate Reservoirs

# INFLUENCE OF ROCK TYPES ON SEISMIC MONITORING OF $CO_2$ SEQUESTRATION IN CARBONATE RESERVOIRS

A Thesis

by

ELNARA MAMMADOVA

Submitted to the Office of Graduate Studies of
Texas A&M University
in partial fulfillment of the requirements for the degree of

MASTER OF SCIENCE

Approved by:

| | |
|---|---|
| Chair of Committee, | Yuefeng Sun |
| Committee Members, | Wayne Ahr |
| | Daulat D. Mamora |
| Head of Department, | Andreas Kronenberg |

August 2011

Major Subject: Geology

# ABSTRACT

Influence of Rock Types on Seismic Monitoring of $CO_2$ Sequestration in Carbonate Reservoirs. (August 2011)

Elnara Mammadova, B.S., Azerbaijan State Oil Academy

Chair of Advisory Committee: Dr. Yuefeng Sun

Although carbonates hold more than 60% of the world's oil reserves, they, nevertheless, exhibit much lower average recovery factor values than terrigenous sandstone reservoirs. Thus, utilization of advanced enhanced oil recovery (EOR) techniques such as high pressure $CO_2$ injection may normally be required to recover oil in place in carbonate reservoirs. This study addresses how different rock types can influence the seismic monitoring of $CO_2$ sequestration in carbonates.

This research utilizes an elastic parameter, defined in a rock physics model of poroelasticity and so-called as the frame flexibility factor, to successfully quantify the carbonate pore types in core samples available from the Great Bahama Bank (GBB). This study shows that for carbonate samples of a given porosity the lower the frame flexibility factors the higher is the sonic wave velocity. Generally, samples with frame flexibility values of <4 are either rocks with visible moldic pores or intraframe porosity; whereas, samples with frame flexibility values of >4 are rocks with intercrystalline and microporosity. Hence, different carbonate pore geometries can be quantitatively predicted using the elastic parameters capable of characterizing the porous media with a representation of their internal structure on the basis of the flexibility of the frame and pore connectivity.

In this research, different fluid substitution scenarios of liquid and gaseous $CO_2$ saturations are demonstrated to characterize the variations in velocity for carbonate-specific pore types. The results suggest that the elastic response of $CO_2$ flooded rocks is mostly governed by pore pressure conditions and carbonate rock types. Ultrasonic P-wave velocities in the liquid-phase $CO_2$ flooded samples show a marked decrease in the order of 0.6 to 16%. On the contrary, samples flooded with gaseous-phase $CO_2$ constitute an increase in P-wave velocities for moldic and intraframe porosities, while establishing a significant decrease for samples with intercrystalline and micro-porosities. Such velocity variations are explained by the stronger effect of density versus compressibility, accounting for the profound effect of pore geometries on the acoustic properties in carbonates.

The theoretical results from this research could be a useful guide for interpreting the response of time-lapse seismic monitoring of carbonate formations following $CO_2$ injection at depth. In particular, an effective rock-physics model can aid in better discrimination of the profound effects of different pore geometries on seismic monitoring of $CO_2$ sequestration in carbonates.

# ACKNOWLEDGEMENTS

I would like to thank many people who contributed and supported me in reaching this goal. First and foremost, I would like to thank my committee chair, Dr. Yuefeng Sun, who has contributed much to this research; plus, he has always been patient, helpful, and encouraging. I specifically would like to thank Dr. Flavio Anselmetti for providing the data and support for this research. I also thank my committee members, Dr. Wayne Ahr and Dr. Walter Ayers, for providing productive and thoughtful feedback.

Thanks also go to my friends and colleagues and the department faculty and staff for making my time at Texas A&M University a great experience. I also want to extend my gratitude to ExxonMobil for providing a summer research grant and ConocoPhillips for their fellowship necessary for the completion of my degree.

I would like to thank my dad, Galib, who as a geologist himself has always been supportive and encouraging of my accomplishments. My parents have always encouraged my academic endeavors, but were particularly relentless regarding this effort. My dog, Misha, has taught me that when the going gets tough, it’s time to go for a walk outside to clear your mind.

# TABLE OF CONTENTS

Page

# LIST OF FIGURES

## LIST OF TABLES

# 1. INTRODUCTION

## 1.1 Motivation and Significance

The subject of carbonates and predicaments associated with their exploration and production has become increasingly important for both researchers and oil industry within the last decade. Carbonates account for approximately 60% of the world's oil and 40% of the world's gas reserves (Schlumberger, 2007). Hence, the commercial importance of carbonates has made them a significant component of future petroleum endeavors. Nevertheless, carbonates exhibit lower average recovery factor values of about 20-35% as compared to terrigenous sandstone reservoirs, which can be governed by a recovery factor of up to 70%. It is merited by complexities of carbonate pore geometries than their siliciclastic counterparts, thus, offering a greater challenge for exploration and production.

Most of the previous experimental and theoretical studies on acoustic properties mainly focus around siliciclastic rocks, which are unlikely to be applicable in carbonates. It would certainly create a big challenge for us to understand carbonates based on those insights gained from siliciclastics. Thus, growing attention has been converging towards the development of new technologies and processes related to challenges and opportunities associated with carbonates.

---

This thesis follows the style and format of Geophysics.

Porosity and permeability are very important parameters in reservoir estimation and characterization, however these properties can be very different in carbonates relative to their siliciclastic counterparts. Carbonates exhibit much more complex pore geometries than siliciclastic rocks. While the primary porosity in siliciclastic rocks is almost exclusively interparticle, carbonate rocks can have variety of pore types, owing it to the complexities of associated pore and pore-throat systems, which are often developed by important role of diagenetic processes (Ahr, 2008). The carbonate pore geometries may represent both isolated pores and connected networks occupied by pore fluids. Thus, porosity and permeability in carbonates are conversely related to individual pore types and pore to pore-throat relationships rather than to the total porosity. This factor contributes to a highly heterogeneous distribution of different permeabilities within a single reservoir, ranging from less than 1 millidarcy to a few darcies. Such heterogeneities in carbonates can be a huge obstacle in characterizing the reservoir properties in carbonates. It can especially be extremely difficult to find a relationship between seismic properties and individual carbonate pore geometries, making the direct identification of hydrocarbons nearly impossible. By and large, carbonate porosities and permeabilities vary as independent parameters, and it requires an accurate rock-physics model to make them somewhat predictable.

Nearly three quarters of hydrocarbons in place are not recoverable by conventional methods (Wang and Nur, 1989), which require the utilization of Enhanced Oil Recovery (EOR) techniques. Primary recovery of hydrocarbons is gravity drive oil or by natural pressures of the reservoir, which may only consist of about 10 percent of a reservoir's original oil in place. During the secondary recovery, the oil is displaced towards the wellbore through the injection of water or gas, resulting maybe in further recovery of the original oil in place. Enhanced oil recovery (EOR) may offer ultimate production of the reservoir's original oil in place. One EOR method includes high pressure $CO_2$ injection for recovering residual oil and gas. This new generation technique has recently emerged to meet the demands of effective exploration and recovery. $CO_2$ injection technique can be used in reducing green-house emission without hindering the rising global energy demand and consumption, while sustaining oil production from existing fields. As $CO_2$ is being injected into the subsurface, geologists and geophysicists need to image and monitor the $CO_2$ to be able to quantify the amount of injected fluid, and whether or not it fills the subsurface storage target efficiently as predicted (Lumley, 2010). The $CO_2$ injection responds to local variations in rock properties. Therefore, seismic monitoring has to be initiated for quantitative and qualitative characterization of such variations induced by the properties of the injected fluid and/or those of the rock frame.

As carbonates are known for their large variations in sonic velocities their seismic response is poorly understood. Since rock velocity is a key parameter in understanding the seismic signatures induced by the flooding, it is especially important to explain such variations in sonic velocities. This would provide more reliable velocity estimation, as well as improved characterization of the effects of carbonate pore types on elastic properties of the rock. That is where the studies of modern carbonates become practical as valuable analogs to unraveling individual pore geometries present in the rock record, which will assist in understanding the lateral and vertical variations in sonic velocities.

Geological sequestration of $CO_2$ has never been an easy task for the oil industry. Depending on the depth of storage, pore pressure and temperature $CO_2$ will behave in various phases. It may exist in the pore space of the subsurface lithology both as in gaseous or liquid phase (Wang and Nur, 1989). The ability to model the elastic properties of rocks saturated in $CO_2$ depends on the detailed knowledge of the effects of $CO_2$ as a pore fluid. The compressibility and density of pure $CO_2$ can vary as much as one order of magnitude across the pressure-temperature range (Lumley et al., 2008; Lumley, 2010).

Because $CO_2$ is not an inert fluid, it can geochemically react with the reservoir rock. This can cause significant decrease in dry frame modulus, which can make it difficult to isolate the $CO_2$ flooding effect alone (Lumley et al., 2008). Previous field experiments on enhanced oil recovery projects have shown that apart from changes in the seismic rock properties, $CO_2$ can also react with the rock matrix to alter or dissolve the rock frame leading to secondary porosities (Lumley, 2010; Vanorio et al., 2010). Other mechanisms during the diffusion of injected $CO_2$ into oil-saturated porous media involve oil swelling and viscosity reductions, which in turn, enhances the oil mobility and increases the oil recovery efficiency. Hence, knowledge of the physical and chemical interactions between $CO_2$ and reservoir oil in addition to their effect on oil recovery are very important for correct projection of any successful flooding process.

## 1.2 Statement of the Problem

This study investigates the controls of different pore types on seismic monitoring of $CO_2$ sequestration in carbonates. Initially, carbonates are known for their large variations in velocity. Hence, it is important to examine why rocks with the same porosity can have extremely different sonic velocities. This requires an accurate rock physics model and a detailed sedimentological and geological analysis. Particularly, the investigation involves how and to what extend rock-physics models can be used to identify different carbonate rock types in terms of their elastic behavior. The later stage of the research involves the study of fluid substitution in carbonates and the influence of individual carbonate rock types on seismic monitoring of $CO_2$ sequestration. It is essential to assess the reliability and quality of appropriate rock-physics model as a key element for time-lapse seismic monitoring of $CO_2$ sequestration in carbonate rocks.

## 1.3 Objectives

As indicated previously, influence of carbonate rock type variations on the sufficiency of seismic monitoring of $CO_2$ flooding has not been addressed to our best knowledge. The aim of this study is therefore to predict the variations in rock properties induced by $CO_2$ flooding, with the comprehension of the elastic behavior of observable pore structures in the rock. Following the scientific problems identified above for this research, we investigate the rock-physics model dealing specifically with the problems surrounding elastic behaviors of carbonates. The main objective of this research is linking rock parameters such as frame flexibility factors (Sun, 2000; Sun, 2004) and pore space compressibilities to observable pore structure in the rock, both to infer the significance of detectable variations (i.e., qualitative interpretation) and to convert them into actual properties of the reservoir rocks (i.e., quantitative interpretation). The second objective of this research involves assessing the influence of individual rock types on seismic monitoring of $CO_2$ sequestration in carbonates

## 1.4 Previous Work

Literature on effects of $CO_2$ sequestration on the seismic properties of carbonate reservoir rocks is relatively scarce. Several theoretical rock-physics models have been introduced (Hamilton et al., 1956; Rafavich et al., 1984; Anselmetti and Eberli, 1993; Sayers, 2008; Xu and Payne, 2009) on the primary factors controlling the acoustic velocities in carbonates. Hamilton et al. (1956) were the first to study the problems associated with the elastic behavior of carbonates and observed a positive correlation between the velocity and pore sizes.

Anselmetti and Eberli (1993) introduced a qualitative rock-physics model relating porosity and pore types to sonic velocities in carbonates. Their model acknowledges the effect of porosity and pore types on variations of acoustic properties in carbonates. However, problems in linking the elastic parameters to observable pore structure in carbonates remain unresolved.

Several authors have studied the pore shape effect on elastic properties, through the quantification of carbonate pore structures and geometrical parameters (Kumar and

Han, 2005; Weger et al., 2009). Sun (2000) established a simplified rock-physics velocity model by introducing a new pore structure parameter, called frame flexibility factor that characterize the structural media with a representation of their internal structure. Because these frame flexibility factors are less dependent on porosity than sonic velocity, they can be easily related to the profound effects of carbonate pore geometries and pore connectivity on elastic properties.

Due to their simplicity many empirical relationships and theoretical equations have been practiced for years by the industry. Despite their widespread use, such empirical fits do not or insufficiently account for the variations in carbonate pore types and diagenetic textures. Therefore, the classic velocity transforms: Wyllie's time-average equation (Wyllie et al., 1958) and other theoretical relationships (Gardner et al., 1974; Raymer et al., 1980) do not adequately explain the velocity variations in carbonates.

Several studies on the effect of $CO_2$ flooding on wave velocities in rocks (Wang and Nur, 1989; Xue and Ohsumi, 2004; Siggins, 2006) have proven to be the useful guides for interpreting the response of time-lapse monitoring following $CO_2$ injection at depth. Resent rock-physics study of Wang et al. (1998) on seismic monitoring of $CO_2$ flooding in a carbonate reservoir has shown that the largest compressional ($V_p$) and shear ($V_s$) wave velocity changes caused by $CO_2$ injections are associated with high-porosity, high-permeability rocks. However, influence of carbonate rock type variations on the sufficiency of seismic monitoring of $CO_2$ flooding has not been addressed to our best of knowledge.

## 1.5 Study Area and Dataset

In order for this analysis to have the validity and to conform with the accuracy of our rock-physics study, a modern analogue of carbonates has been selected. This research uses a publicly available dataset from Bahamas Drilling Project (Ginsburg, 2001). The total of 89 samples was collected from two core borings (Clino and Unda) on the western flank of Great Bahama Bank (Figure 1.1). The sedimentology of these cores has been described in detail elsewhere (Kenter et al., 2001), and therefore only a brief description is included here.

GBB is a low-angle, prograding carbonate edifice, where progradation is a result of sea-level fluctuations, switching the carbonate factory on, upon which progradation took place. However, several erosional and condensed surfaces are also furnished when sea level dropped below the margin. Two continuous core borings, Unda and Clino are located 8.5 km apart from each other on the prograding margin of Northwest Great Bahama Bank (GBB). Unda is penetrated mostly the topset of the prograding sequence, whereas the second hole Clino is drilled on the inclined forsets (Figure 1.2). Unda and Clino are penetrated to depth of 442 and 662 m below seafloor, respectively. The oldest drilled sediments are middle Miocene of age, which corresponds to the well Unda, whereas the bottom of Clino reaches the age of Late Miocene only. The retrieved lithologies are platform interior to platform-margin and slope carbonates, with no siliciclastics (Ginsburg, 2001).

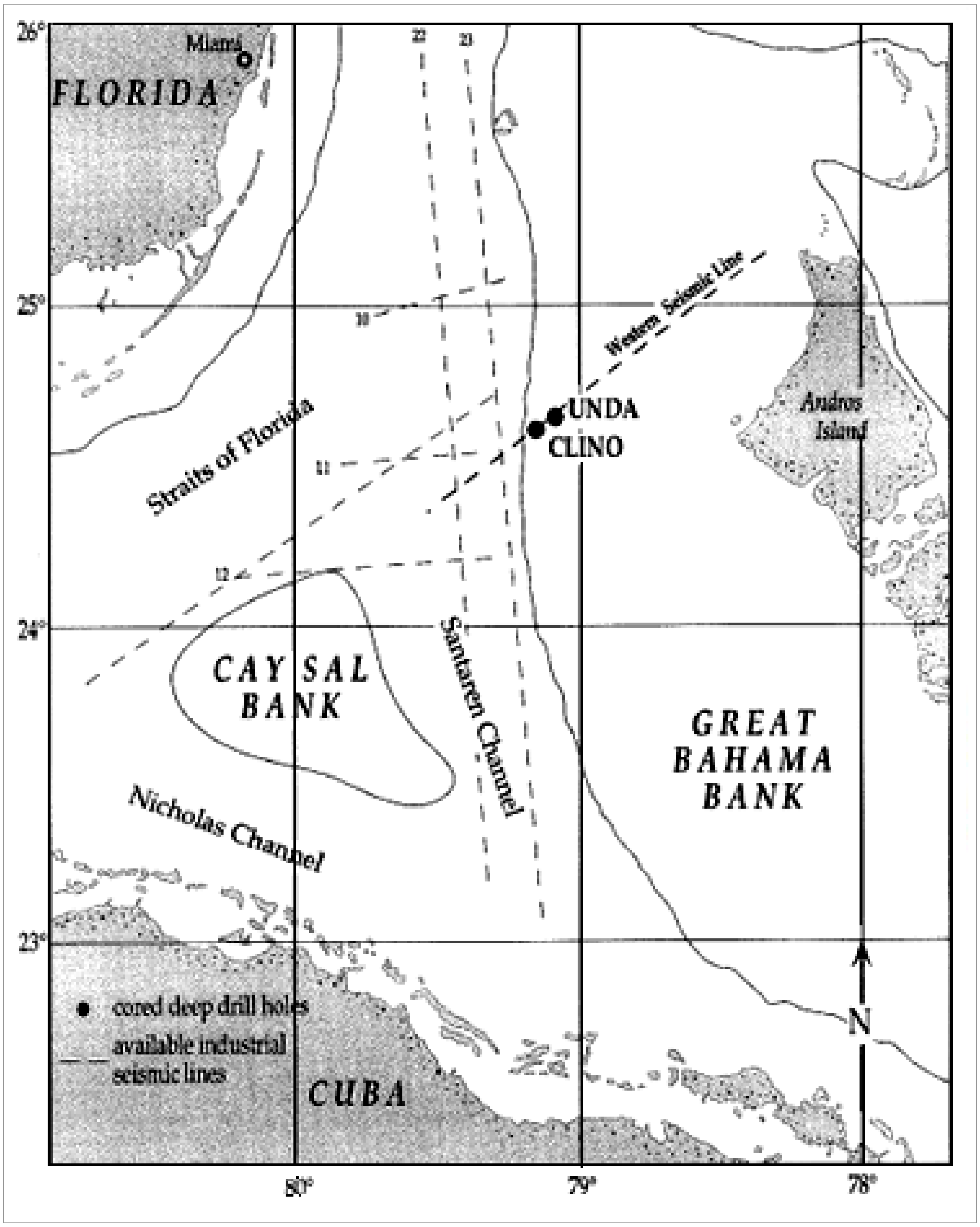

**Figure 1.1** The map of Great Bahama Bank (GBB) showing the locations of the Western seismic line and the two core borings, Clino and Unda, located 8.5 km from each other (Ginsburg, 2001).

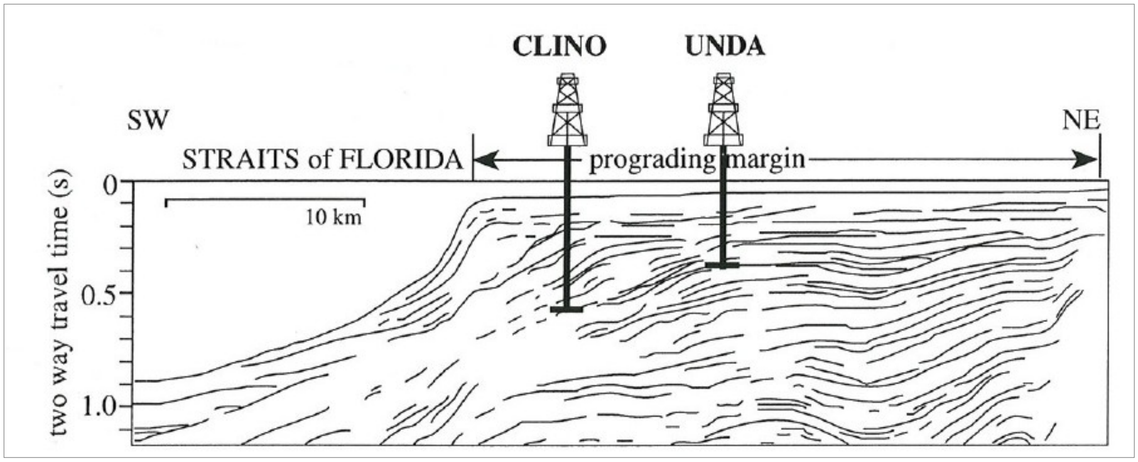

**Figure 1.2** Part of western seismic line, with the location of two continuous core borings, Clino and Unda, penetrating the western prograding margin of Northwest GBB (Ginsburg, 2001).

The experimental dataset in support of this research contains the results from analysis of physical properties on discrete samples from Northwestern Great Bahama Bank (GBB). Our carbonate samples are from two continuous core borings, Clino and Unda, in a single prograding carbonate edifice from Miocene to Pleistocene age, with platform, reef and slope depositional environments. In order to simulate the in situ reservoir conditions in the laboratory, ultrasonic compressional-wave and shear-wave velocities of 89 carbonate samples were measured under varying confining and stable pore-fluid pressures (Anselmetti and Eberli, 1993). Other petrophysical data such as porosity, density and permeability, with lithological parameters taken from thin section observations and X-ray analyses are also included in the dataset. All petrophysical and lithological data of measured minicore samples are listed in Appendix A. Altogether, the available dataset and information is combined into an integrated reservoir rock physics model in provision of our simulated $CO_2$ fluid substitution.

## 1.6 Methods

This research is the integration of geology and geophysics via rock-physics model as follows:

(1) Qualitative and quantitative characterization and identification of individual carbonate rock types in GBB, based on 89 samples collected from cores of Unda and Clino from various depths and from all representative lithologies;

(2) Linking pore geometries to elastic properties using physically sound rock physics models;

(3) Analyses of the influence of different carbonate rock types on seismic monitoring of $CO_2$ sequestration under different injection and effective pressures;

The first part of the research involves the examination of physical and elastic properties, with the pressure dependence analyses of sonic velocities in carbonates from GBB (Ginsburg, 2001). Based on the geological background from the area, including depositional environment and diagenetic history, both qualitative and quantitative interpretations are delivered. The interpretations are then used to identify individual carbonate rock types and their influences on elastic properties.

The second part of the research focuses on the application of available rock-physics models capable of quantifying the different carbonate pore geometries. The elastic parameter introduced through Sun (2000) model provides a characterization of structural media with a representation of their internal structure. In order to quantify the velocity deviations at given porosity we introduce a different rock-physics model (Baechle et al., 2006) involving the pore space compressibility of the rock. By providing a non-linear relationship, this model quantifies of the profound effect of pore structure and its connectivity on the elastic properties in carbonates.

The last part of the research investigates how different rock types have an influence on seismic monitoring of $CO_2$ sequestrations in carbonates. The fluid substitution model based on Gassmann equation (1951) is used to estimate the elastic moduli of initially water-wet rock types before and after the fluid substitution. Taking into account that the quality of Gassmann fluid substitution model is highly dependent on the accuracy of fluid parameters, $CO_2$ properties in gaseous and liquid phases are estimated (Batzle and Wang, 1992). Having a correct estimation of $CO_2$ properties is especially important when varying injection pressures are involved in the substitution model. Since $CO_2$ must be injected at a higher pressure than the original formation pore fluid pressures, $CO_2$ injection decreases the effective/differential reservoir pressure. As the pore pressure increases, both the bulk modulus and the bulk density of $CO_2$ increase considerably which consequently results in different phase behavior of $CO_2$ (liquid or gas). Using measurements from core samples with equal porosities we simulate fluid saturations ranging from water to oil and oil to $CO_2$. This will shed light on the relative effects of $CO_2$ sequestration on sonic properties of the rock.

# 2. GEOLOGICAL ANALYSIS OF ACOUSTIC PROPERTIES OF CARBONATE ROCKS

## 2.1 Introduction

Because of the peculiarity of carbonates to diagenesis, their characterization of acoustic properties has always been a challenge. Over the past century, many studies have increased our knowledge of acoustic wave propagation in siliciclastic rocks (Marion et al., 1992; Vernik and Nur, 1992). However, the concepts derived from such studies have not proven to be fully applicable in carbonates.

Acoustic wave propagation in rocks is affected by many factors such as pore fluid content, rock framework and pore space, among others. The rock framework and pore space in carbonates are controlled by both the nature of depositional environment and diagenetic history of the rocks. Nonetheless, porosity is considered to be the main controlling factor in determining the sonic velocities in rocks. However, in carbonates pore structures are nearly equally important as the total porosity in determining the acoustic wave propagation (Anselmetti and Eberli, 2001).

Post-depositional processes especially, such as mechanical, chemical or biological events can cause a wide velocity distribution in carbonates. Because carbonate minerals are prone to chemical changes, diagenesis is more prevalent. Diagenesis can fundamentally modify the pore structure and mineralogy of the rock, particularly, dissolution, recrystallization and cementation processes can continuously rework the pore structure to either create or destroy porosity. These diagenetic alterations and associated changes in the rock frame and the pore structure result in a wide range of sonic velocity measurements at a given porosity. In concert, velocity is a combined effect of many processes, during and after deposition.

This section investigates and characterizes the carbonate specific pore types, their velocity patterns, and the relationships between the physical rock properties and the lithological variations. The detailed laboratory measurements from two core borings on the prograding western margin of GBB (Ginsburg, 2001) provide an excellent opportunity to study the lithological factors that control the sonic velocities in carbonates. There are 89 samples in total, with variety of diagenetic features enabling the characterization of velocity patterns with respect to different diagenetic stages.

## 2.2 Velocity Analysis

Both compressional and shear wave velocities (Vp and Vs) of 89 minicore samples from different depositional environments and geological ages were measured at 10 MPa confining and 2 MPa pore fluid pressures (Anselmetti and Eberli, 1993). Samples are highly porous, so the resulting effective pressure of 8 MPa was sufficient for good signal transmission without causing any significant fracturing in the rocks (Anselmetti, 1994). Samples range from unconsolidated mud to lithified sediments. The successions of both two continuous core borings, Clino and Unda, correspond to the prograding part of the platform margin. Nevertheless, the intervals of deeper-water sediments record periods of rapid rise of sea level and possible backstepping of the platform and reefal units (Anselmetti, 1994).

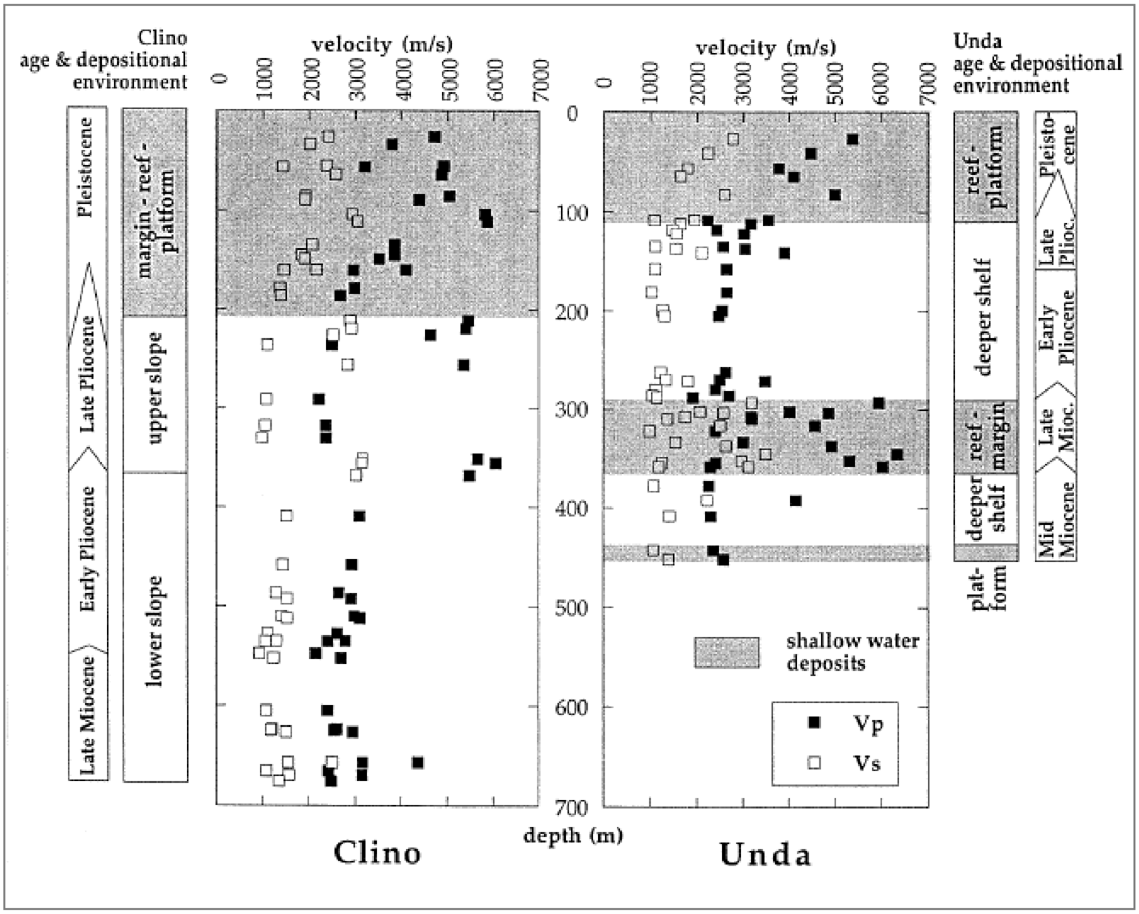

**Figure 2.1** Correlation of Vp and Vs (at 8 MPa effective pressure) relative to depth, depositional environment and age. Total of 89 minicore samples collected from the two drillholes Unda (right) and Clino (left) on Great Bahama Bank (GBB). Shaded areas in graph correspond to the shallow water platform deposits (Anselmetti, 1994).

Unda is located 10 km from the modern platform edge and penetrates to 454.15 m below the mud pit datum (Figure 2.1). The top of the rock section is of Pleistocene, and the bottom is of Middle Miocene age. Unda is characterized by three successions of shallow-water platform and reefal deposits that alternate with deeper shelf deposits. Clino, on the other hand, is 8.5 km west-southwest of Unda, penetrating to 677.70 m below the mud pit datum (Figure 2.1). Clino is characterized by a single interval of shallow water platform and reefal sediments overlying a thick succession of slope sediments subdivided into upper and lower units.

The usual assumption of velocity increasing with depth (Hamilton, 1980; Japsen, 1993) is not valid for samples from GBB. Figure 2.1 reveals that there is no clear relationship between depth/age, and velocity trends. However, there is a visible correlation between the depositional environments and the velocity distributions. Both drillholes display higher velocity and velocity variations for shallow water platform deposits relative to deeper water sediments.

Depositional environments are important in terms of the established lithologies and their susceptibility to future diagenetic alterations. The different lithologies would have different response mechanisms to diagenetic processes (Schlanger and Douglas, 1974). Shallow water sediments are coarser than deep water sediments. Hence, coarse grains allow higher fluid flow and higher concentration of metastable minerals (aragonite) during deposition, thus resulting in more rapid diagenetic alterations. Meanwhile, deeper water deposits generally undergo less diagenetic alterations and are therefore lower-velocity zones compared to reefal units and platform margin carbonates. The younger sediments of both drillholes at shallow depths have higher velocities due to intense diagenetic alterations that take place much faster than compaction (Anselmetti, 1994). Hence, the velocity distribution of GBB is more a function of a depositional environment and diagenetic history, rather than the compaction or burial depth/age.

The block diagram of depositional environments against acoustic velocities implies that the majority of the samples are comprised of slope deposits, which are low velocity samples (Figure 2.2). Only about 9% of all the slope samples show higher velocities above 4500 m/s corresponding to skeletal-rich turbidities of platform-derived material in slope intervals. The platform deposits show highest velocity average. Reef deposits exhibit both low and high velocities triggered by different diagenetic processes, such as dissolution and cementation that can alter the pore space either by increasing or reducing the porosity. The average velocity for reefal deposits has a transitional value between slope and platform facies (4227 m/s).

Porosity distributions do not show much consistency with depositional environments (Figure 2.3). However, 50% of all the samples display porosities between 40 and 50% much of which consists of unconsolidated mud of slope deposits and intervals with vuggy to cavernous porosity of shallow water platform and reefal facies altered during extensive meteoric diagenesis. Lowest porosities, on the other hand, correspond to the well cemented samples of reefal units.

The measured velocities of 89 samples from both cores of Clino and Unda at an effective pressure of 8 MPa display a wide range of velocities with Vp ranging from 1500 to 6500 m/s and Vs ranging from 900 to 3500 m/s. The average compressional and shear wave velocities are approximate 3500 and 1800 m/s, respectively. However, the velocity average of both Vp and Vs is higher in Unda, than in Clino. This is because Unda penetrates three separate successions of higher-velocity shallow water deposits, whereas Clino penetrates only one shallow-water succession (Figure 2.1).

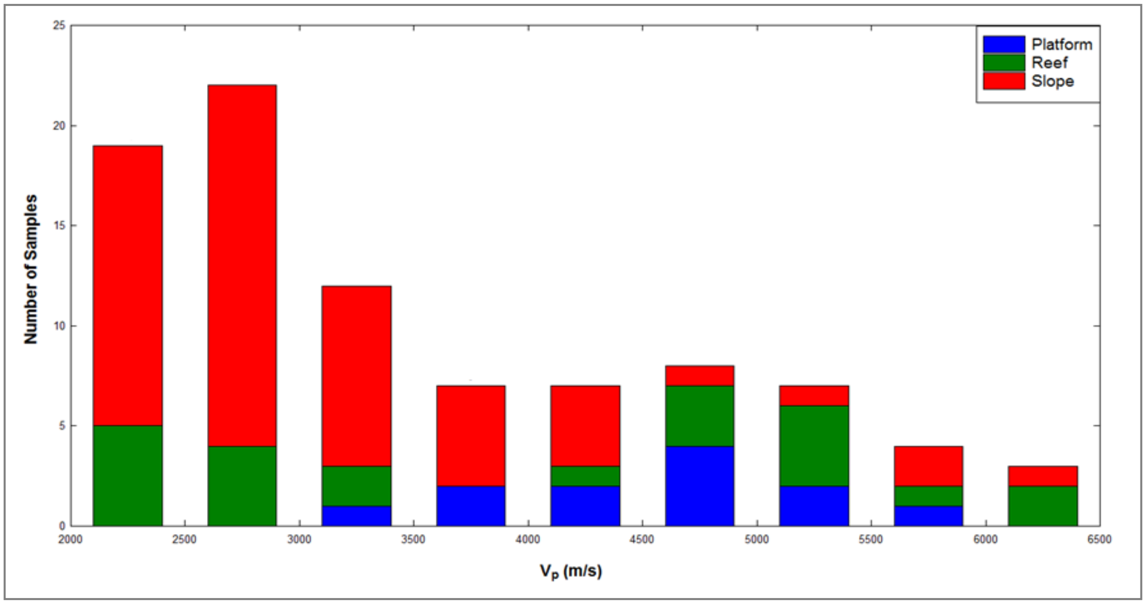

**Figure 2.2** Block diagram of velocity against three main depositional environments of two continuous core borings, Clino and Unda.

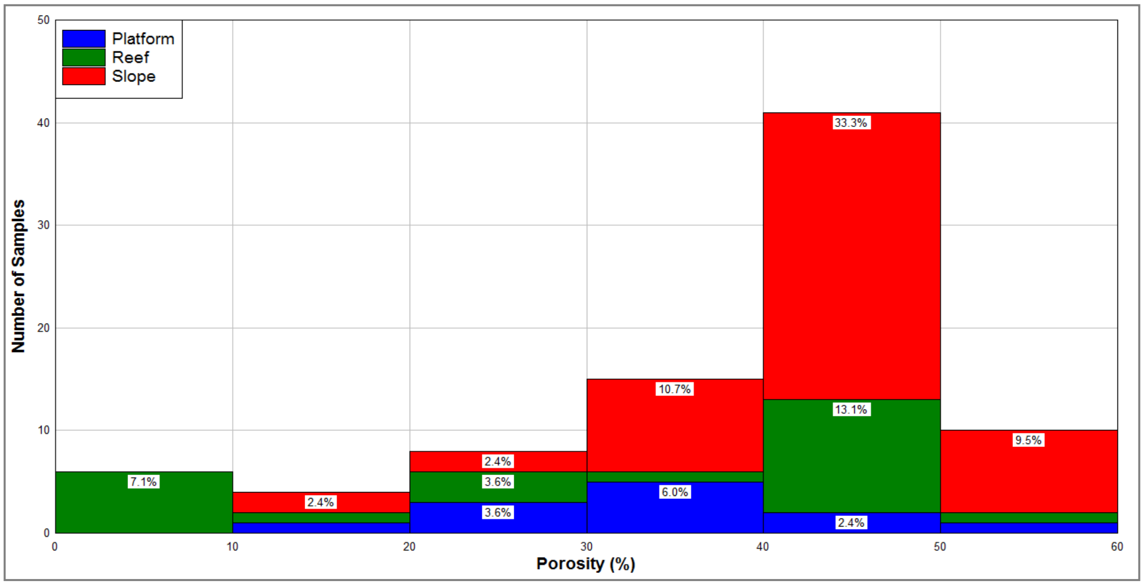

**Figure 2.3** Block diagram of porosity against three main depositional environments of two continuous core borings, Clino and Unda.

The measured velocities of 89 samples from both cores of Clino and Unda at an effective pressure of 8 MPa display a wide range of velocities with Vp ranging from 1500 to 6500 m/s and Vs ranging from 900 to 3500 m/s. The average compressional and shear wave velocities are approximate 3500 and 1800 m/s, respectively. However, the velocity average of both Vp and Vs is higher in Unda, than in Clino. This is because Unda penetrates three separate successions of higher-velocity shallow water deposits, whereas Clino penetrates only one shallow-water succession (Figure 2.1).

Unlike siliciclastic rocks, where variations in mineralogy can cause large velocity contrasts, carbonates are less influenced by the mineral content of the rock (Anselmetti and Eberli, 1993). Our data show limited variability in mineralogy (Figure 2.4), where calcite, dolomite and aragonite have somewhat very similar physical properties. For two samples of the same mineralogy the acoustic wave speeds can differ 2-3 times of its magnitude (Table 2.1). For example, two rock samples from Unda are both composed of 100% dolomite. Sample Unda at 321 m has Vp of 2405 m/s and a Vs of 991 m/s. The second sample from the same well at 345 m has a Vp and Vs of 6350 and 3490 m/s, respectively. Here, the high-velocity sample is highly cemented reefal dolomite with a total porosity of 6%, whereas the low-velocity sample is a sucrosic dolomite with intercrystalline porosity of 46% (Anselmetti, 1994). Hence, the mineralogy has little direct influence on variations in sonic velocity.

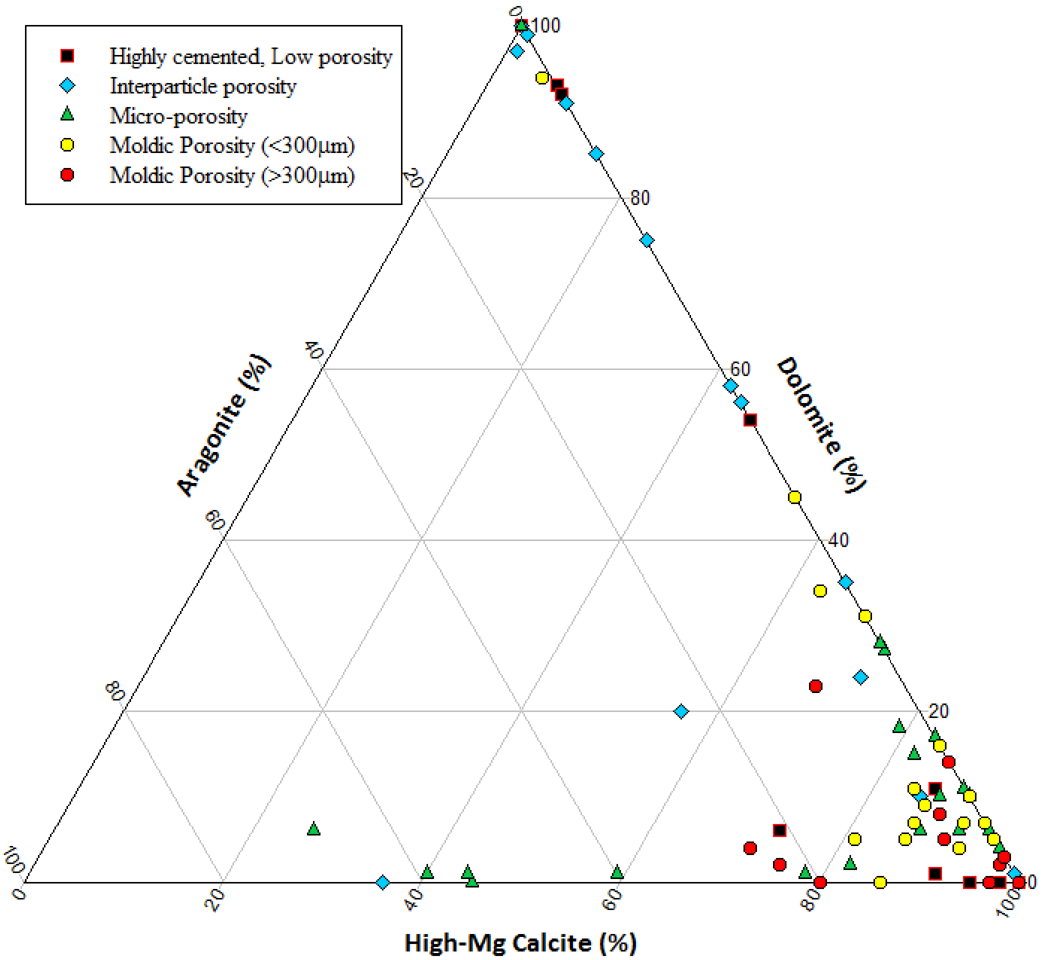

**Figure 2.4** The variations in mineralogy expressed in a ternary plot of 3 variables (aragonite, dolomite and high-Mg calcite) showing the relative compositions of corresponding carbonate pore types. The proportions of the three variables plotted always sum to a constant of 100%.

**Table 2.1** Velocity and porosity data for two samples with the same mineralogy. The velocity spans nearly three times as a result of the different pore structures and pore sizes, ineffective of the similar mineralogy.

| Depth (m) | Mineralogy | Vp (m/s) | Vs (m/s) | Porosity | Pore type |
|---|---|---|---|---|---|
| 321m | 100% Dolomite | 2405 | 991 | 46% | Intercrystalline |
| 345m | 100% Dolomite | 6350 | 3490 | 6% | Highly cemented |

As mentioned earlier, porosity is the main factor controlling the sonic wave velocities in rocks. However, carbonates with equal porosity can have very different velocities, which are directly related to different pore types rather than the amount of the available pore spaces. In general, velocity displays inverse correlation with the porosity, which is also true for GBB samples. Figure 2.5 displays a velocity-porosity crossplot where an increase in porosity produces a decrease in Vp and Vs. Nevertheless, especially at higher porosities (>30%) the sonic velocities display a large variations and deviate from best-fit curves.

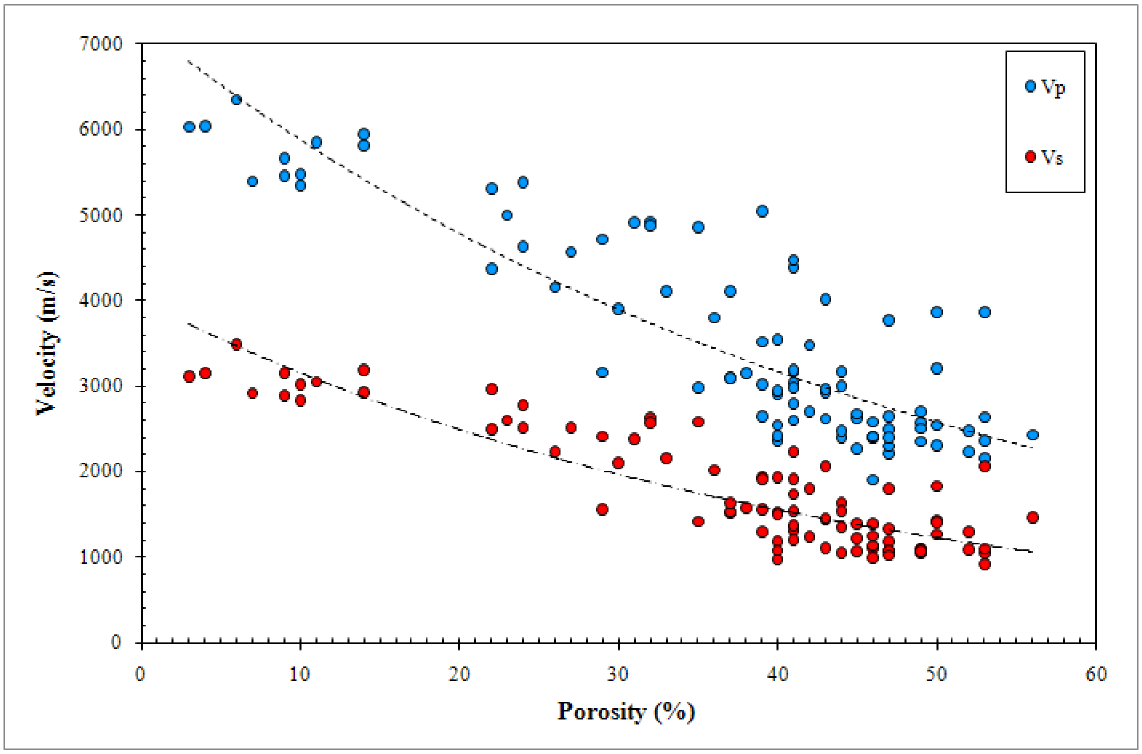

**Figure 2.5** Velocity as a function of porosity for GBB dataset. Both $V_p$ and $V_s$ display an inverse correlation with increasing porosity, but at higher porosities they clearly show a large scatter around the exponential best-fit curves.

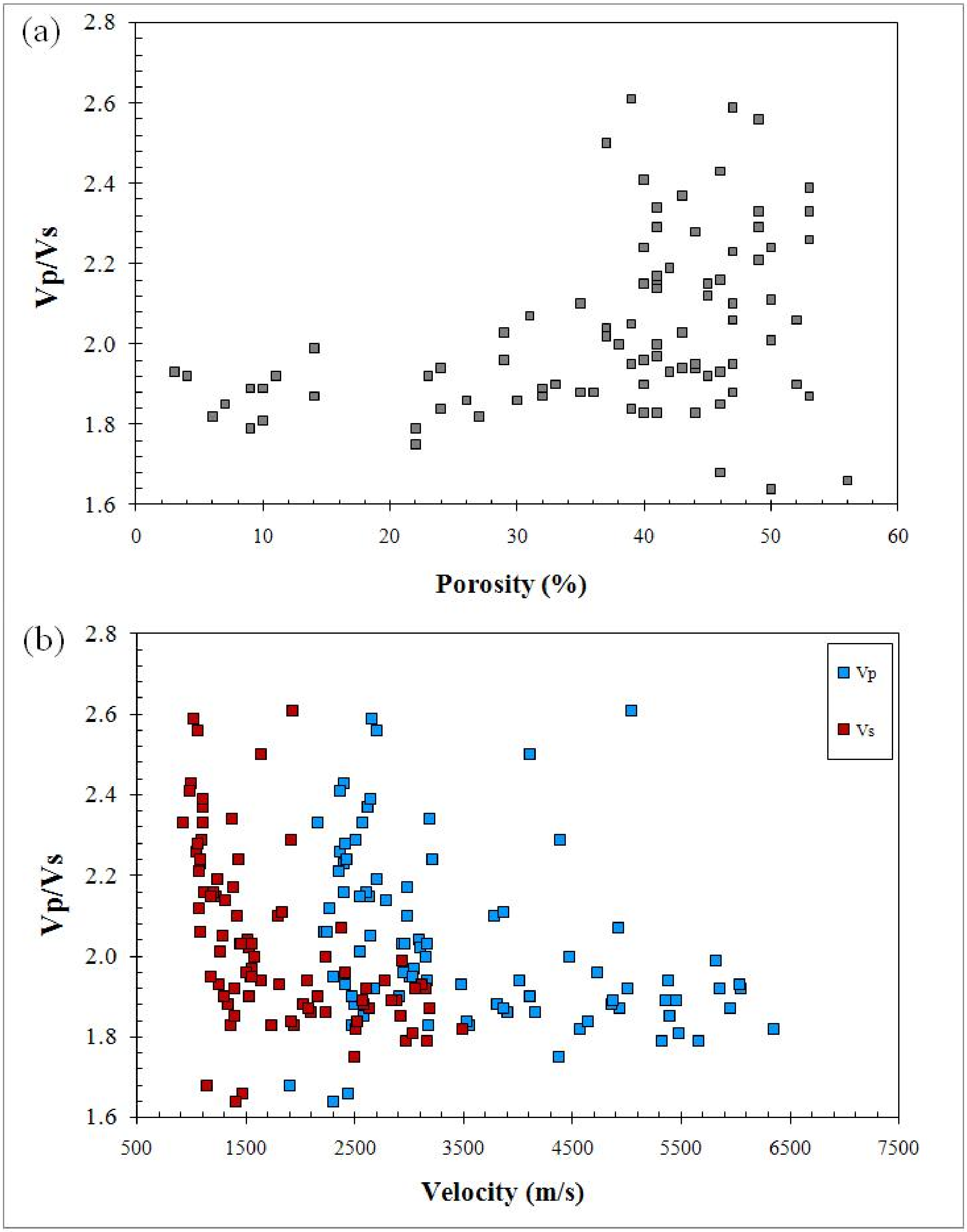

**Figure 2.6** Vp/Vs ratio as a function of porosity (a) and velocity (b). The Vp/Vs ratio reflects a much larger variability with increasing porosity and decreasing velocity.

As seen from Figures 2.5 and 2.6 sonic velocities and velocity ratios produce large scatters, especially at higher porosities. Such variations cannot be explained only by the porosity amount; this approach does not consider the distribution of pore spaces in the rock, and therefore ignores pore sizes, pore geometries and pore connectivity, which are important agents in determining the acoustic behaviors of carbonates. Hence, pore geometries of all samples have to be taken into account in order to relate carbonate rocks to sonic velocities.

## 2.3 Porosity and Pore Types

Sediments of continuous core borings, Clino and Unda have wide range of plug porosities from as low as 3% up to 60%. Based on plug data, sediments with skeletal grainstones and packstones have high porosities except for highly cemented intervals. Dolomitized intervals have porosities between 30-50%, and moldic pores ranging from 25% to 50%.

Anselmetti and Eberli (1993) were the first to classify the pore types in samples from Clino and Unda based on the Choquette and Pray (1970) classification. Several pore types exist in these samples, some of which are both primary and secondary porosities. Primary porosities include intragranular and intergranular pores. Intragranular macroporosities are commonly formed in foraminifera, corals, gastropods, articulated bivalves, and encrusting algae (Melim et al., 2001). Primary intergranular microporosity however is found in rocks with preserved aragonite needles (Melim et al., 2001).

Secondary porosities include vuggy to moldic, intercrystalline pores and minor fractures. Vuggy pores are a result of non-selective dissolution of carbonate sediments, whereas selective dissolution produces moldic pores (Choquette and Pray, 1970). Nearly 60% of macropores present in our samples constitute of moldic pores, forming either connected or isolated networks, or a combination of both. Part of the secondary porosity constitutes the sucrosic intercrystalline micropores generally present in Unda. Fracture porosity is found in Clino mainly at intervals between 365 and 450 m, some of which are cemented. Fractures are less abundant in Unda but they are open and do not contain cements (Melim et al., 2001).

Pore geometries in carbonates define the pore space available to fluid flow. Thus, permeability is mainly a function of pore type, pore size, and pore connectivity (Blatt et al., 1980). Based on thin section observations the Bahamas samples were grouped into five categories of predominant pore types (Figure 2.7 and 2.8): (1) highly cemented, low porosity, (2) interparticle, (3) intraparticle, (4) micro-porosity, (5) coarse and fine moldic porosity (Anselmetti and Eberli, 1993).

If all the samples were grouped into five categories of dominant pore types on the basis of thin section observations (Anselmetti and Eberli, 1993) each pore type will have its own characteristic pattern in the velocity-porosity plot (Figure 2.7). This velocity distribution for every group of samples with the same dominant pore geometries can explain why rocks with the same porosity can have very different sonic velocities. In Figure 2.7, Wyllie's (1958) "time-average equation" is a reference curve providing a linear relationship between velocity and porosity:

$$\frac{1}{V} = \frac{\varphi}{V_{fl}} + \frac{1-\varphi}{V_m} \tag{2-1}$$

where, $\varphi$, $V_{fl}$, $V_m$ are porosity, fluid velocity and matrix velocity, respectively. Wyllie's equation has been used for years by the industry for its simplicity. However, comparison of the measured velocities with the velocities obtained from Wyllie's theoretical equation (2.1) shows that the velocity predictions from time-average equation are generally underestimate the much faster Bahamian carbonates (Figure 2.7).

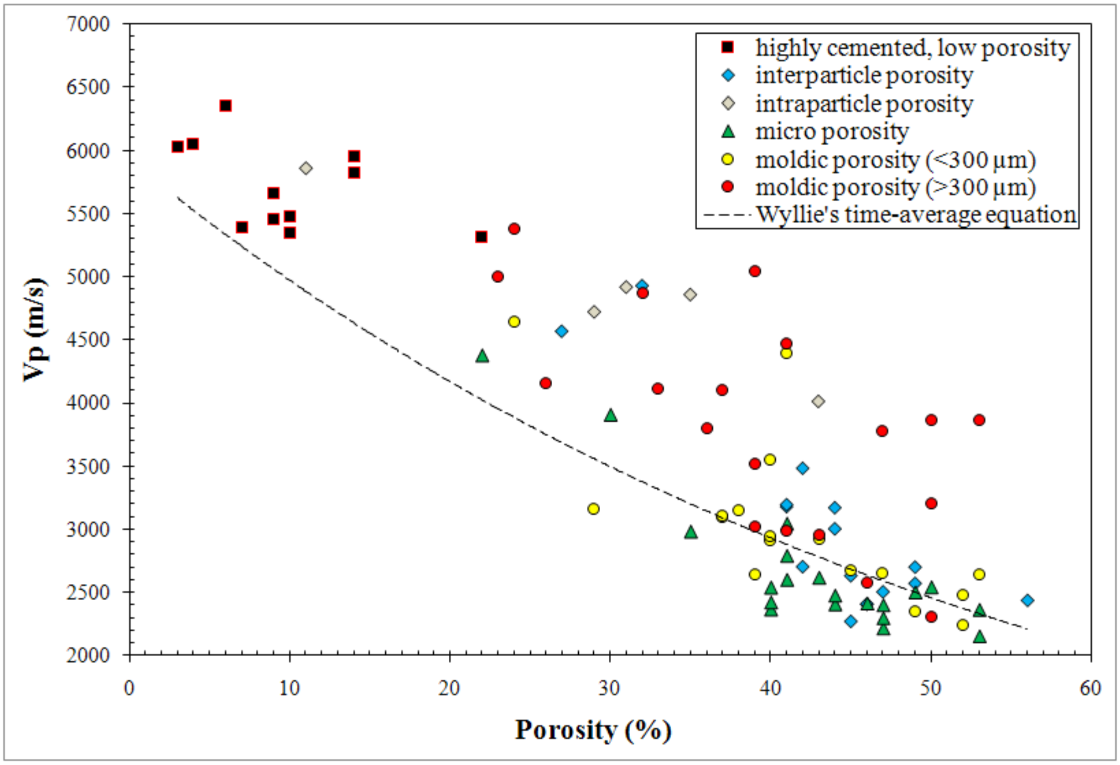

**Figure 2.7** Compressional velocity against porosity plot relative to carbonate-specific pore types. All pore types have characteristic clustering with reference to Wyllie's time-average curve.

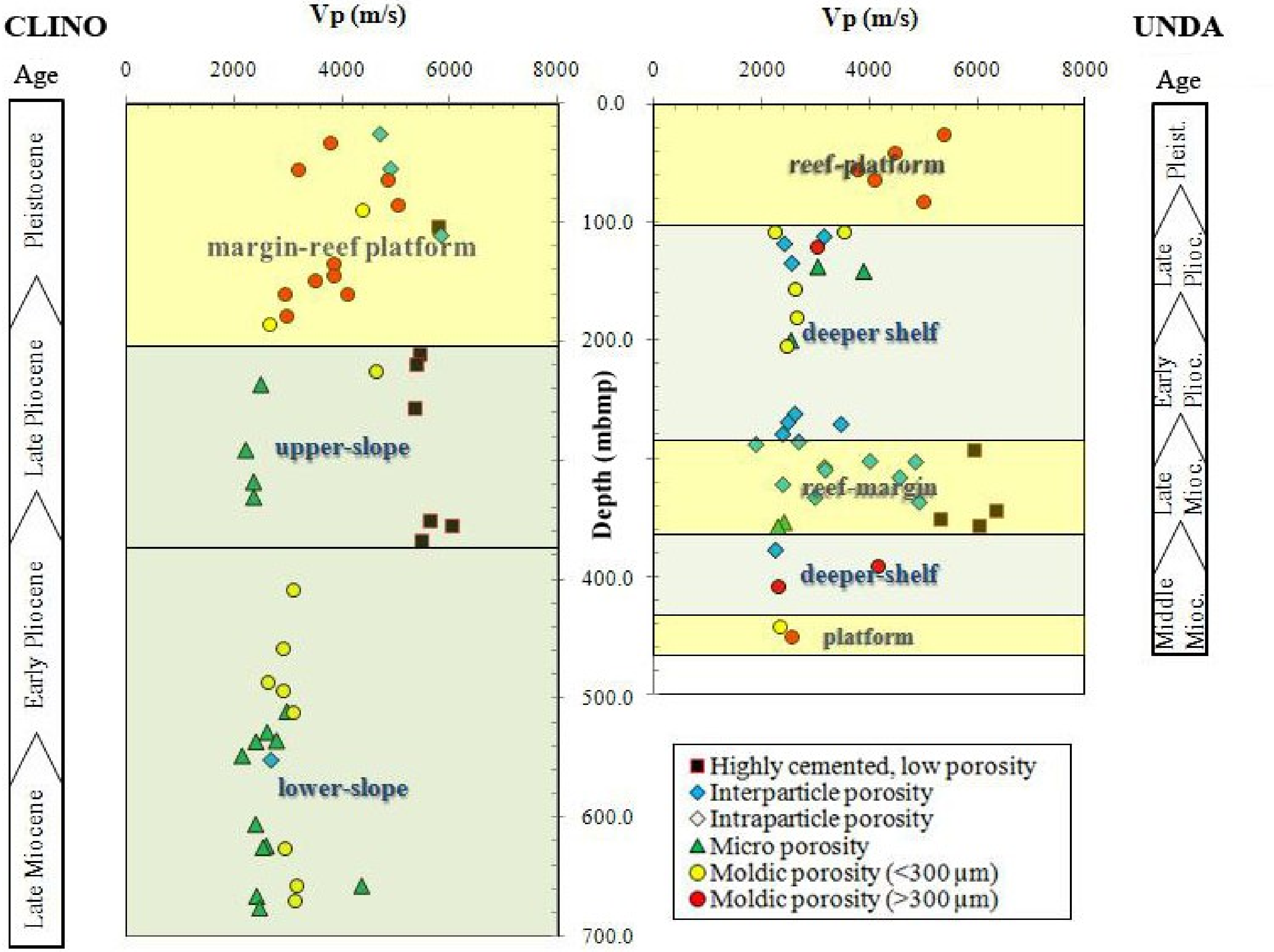

**Figure 2.8** Correlation of $V_p$ and $V_s$ (at 8 MPa effective pressures) with depth, depositional environment and age with the knowledge of pore types in Unda and Clino from GBB (modified from Anselmetti, 1994).

(1) Highly cemented, low porosity samples (Figure 2.9) have plug porosities of 20% and less, characteristic of final stages of diagenesis. They have extensive blocky cementation and are found in reef-platform and upper slope intervals of Clino and Unda. The velocity-porosity diagram of highly cemented rocks forms a cluster at the upper end of the time-average equation trendline with high velocities and low porosities.

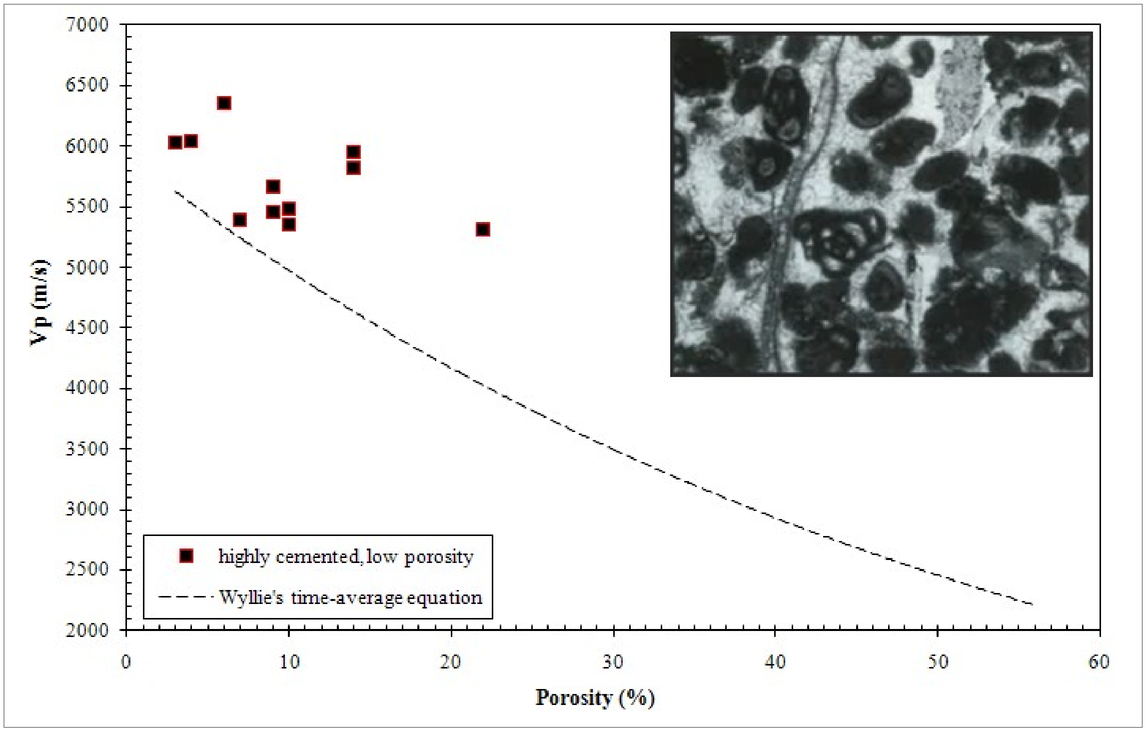

**Figure 2.9** Velocity-porosity diagram of highly cemented, low porosity carbonates, in reference to Wyllie's time-average equation trendline. The upper right hand corner image is a photomicrograph (~1mm) of a sample from Unda at 358 m, with plug porosity of 3%: mainly skeletal grainstone cemented with a blocky calcite that completely filled the former interparticle pore space (Anselmetti and Eberli, 1993).

(2) Interparticle and intercrystalline porosity (Figure 2.10): The pore space between the grains formed after deposition is classified as interparticle porosity

(Choquette and Pray, 1970). Intercrystalline porosity on the other hand occurs through dolomitization process, where minerals are crystallized to form dolomite rhombohedra. These pore types are mainly limited to Unda at 108-377m (Figure 2.8). The porosity is 30% and higher and the velocity-porosity relationship displays a negative departure from Wyllie's time-average curve. Interparticle porosities with their higher velocities and lower porosities distinguish themselves from intercrystalline samples.

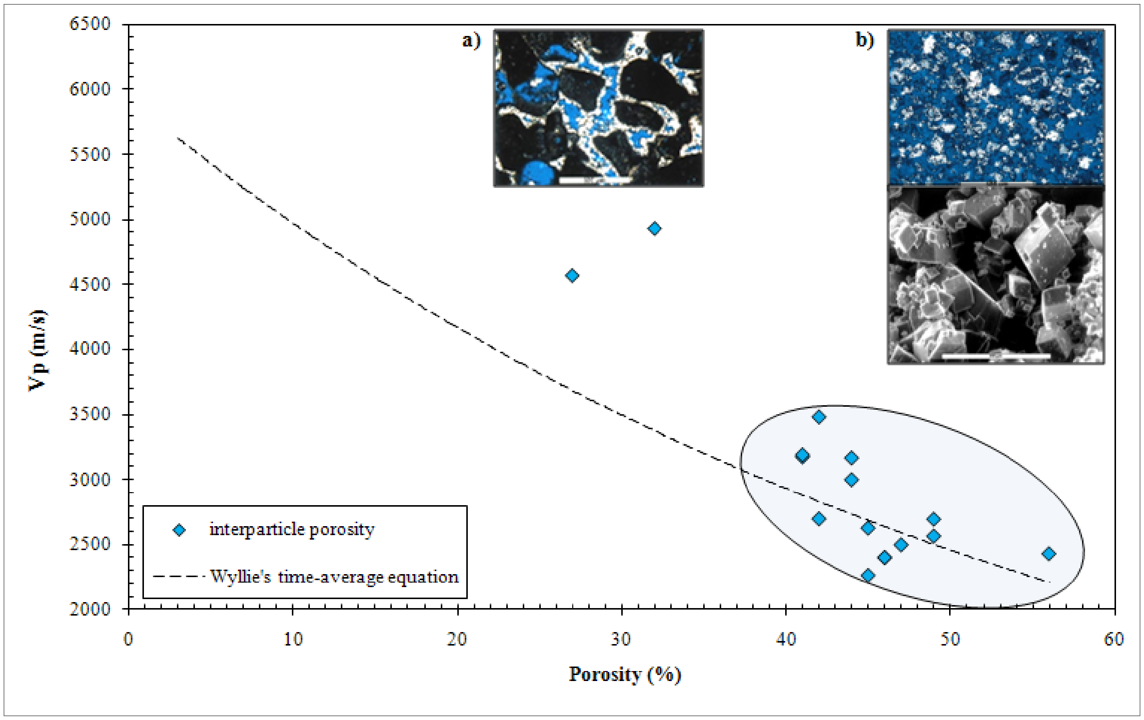

**Figure 2.10** Velocity-porosity diagram of interparticle/intercrystalline porosity, in respect to Wyllie's time-average equation curve. (a) Photomicrograph (~500µm) of a bioclastic grainstone with interparticle porosity with preserved bioclasts and interparticle cement with total porosity of 23%; (b) Photomicrograph (~500µm) and Environmental Scanning Electron Microscope (ESEM) image (~200µm) of a sucrosic dolomite consisting purely of dolomite rhombohedra with total porosity of 49% (Anselmetti et al., 1998).

(3) Intraparticle porosity (Figure 2.11): Based on Choquette and Pray (1970) classification, intraparticle porosities are framestones and boundstones, where organically bound organisms such as corals and bryozoans form a rigid framework during deposition. Hence, they are present in reef-margin intervals of both drillholes. Their framework would have high elastic rigidity, resulting in lower porosities. The velocities in intraparticle porosity samples show much higher values than the time-average curve.

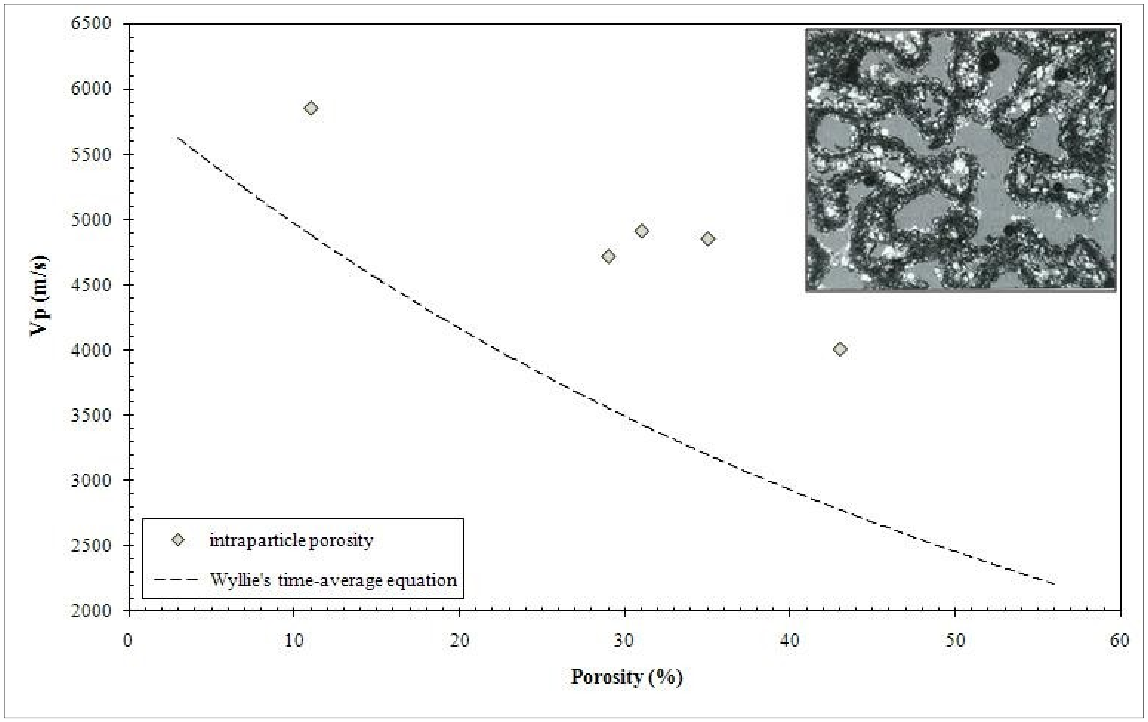

**Figure 2.11** Velocity-porosity diagram of 5 samples with dominant intraparticle porosity (framestones and boundstones). Velocities are much higher than velocities calculated with Wyllie's time-average equation. The upper right hand corner image is a photomicrograph of a coral sample from Unda at 302m. The porosity is integrated in the construction of the frames. The plug porosity is 43% (Anselmetti and Eberli, 2001).

(4) Micro-porosity (Figure 2.12): Micropores are less than 10µm in size, and are profuse in carbonate mud. The dominant micro-porosity is common in carbonates with high micritic content. Micro-porosity shows higher porosity values similar to interparticle/intercrystalline pore types, resulting in lower velocities than the time-average trendline. This pore type is present in both cores; in Clino they are more abundant, confined to slope intervals (197-677m).

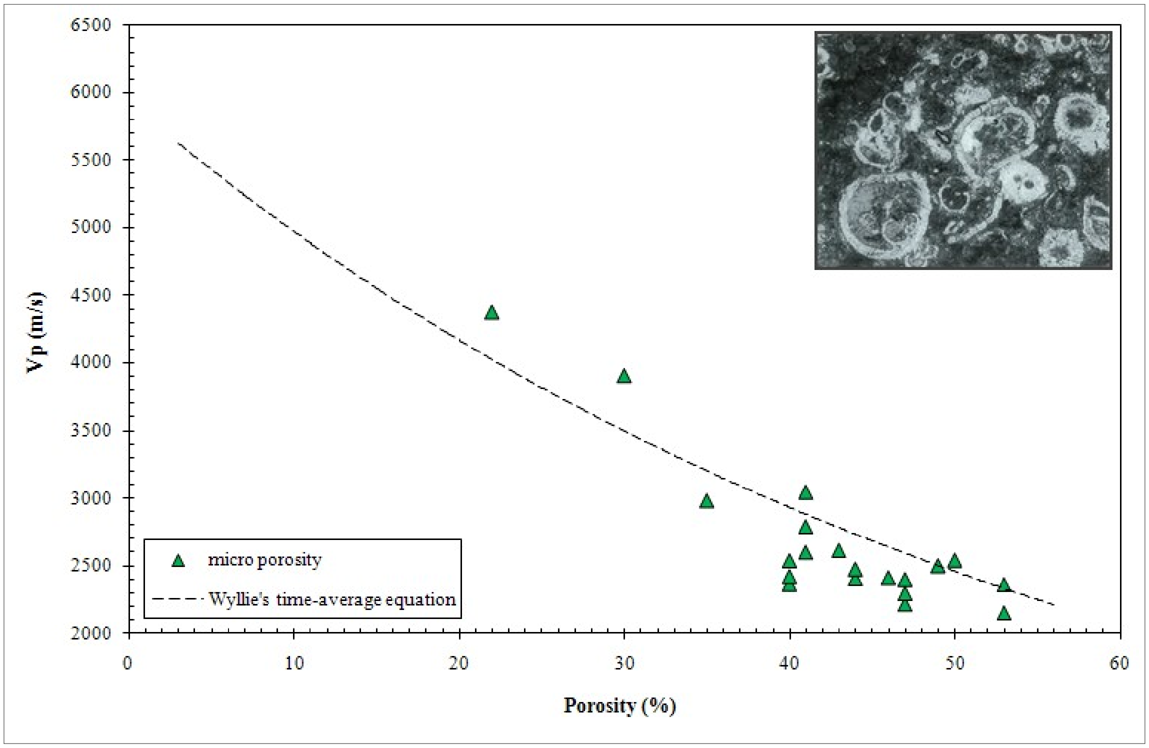

**Figure 2.12** Velocity porosity diagram of samples with dominant micro-porosity (negative departure from time-average curve). The upper right hand corner image is a photomicrograph of a sample from Clino at 510m. It is a slope deposit rich in globigerinids and micritic matrix with little compaction (Anselmetti and Eberli, 2001).

(5) Moldic porosity (Figure 2.13): Moldic porosity is a product of dissolution of metastable minerals, such as aragonite and high-Mg calcite. These samples show self-supporting framework, with high elastic rigidity. They mostly produce a positive departure from Wyllie's time-average curve. The porosities range between 20-55%, where permeability varies depending on the pore connectivity and diameter. Fine moldic porosity (<300µm) displays lower velocities than coarse moldic porosity (>300µm).

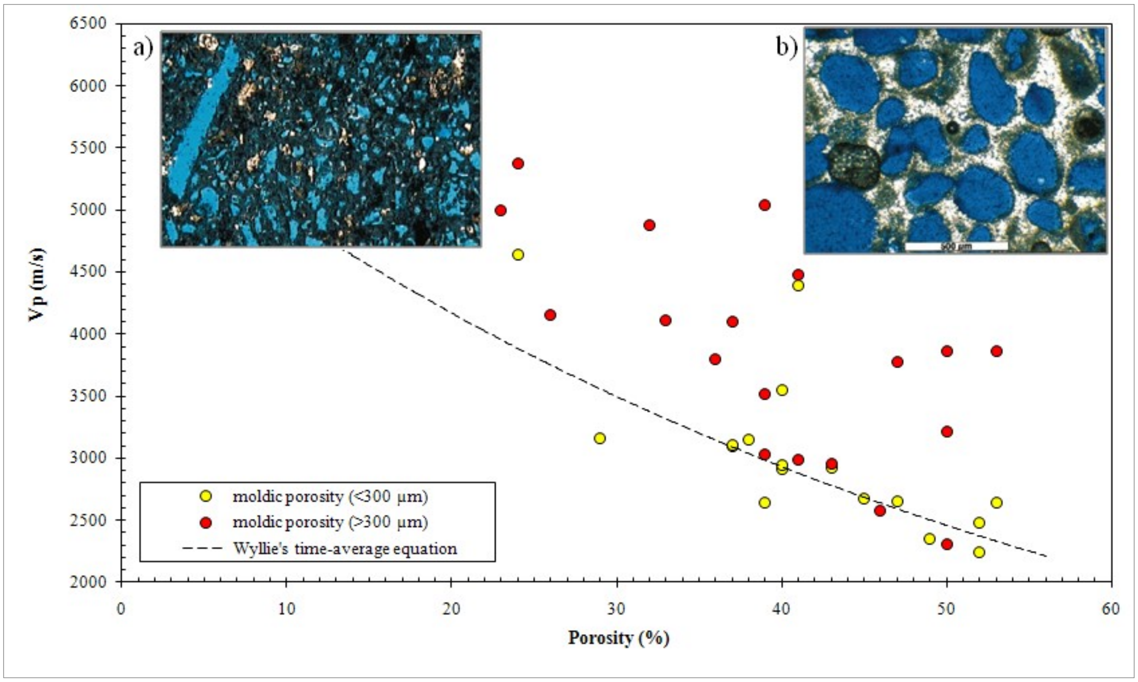

**Figure 2.13** The velocity-porosity diagram of samples with dominant moldic porosities. (a) Photomicrograph (~1mm) of a sample with fine moldic porosity (<300µm) of dissolved bioclasts with micrite matrix (plug porosity=41%, permeability=181mD) (Anselmetti et al., 1998). (b) Photomicrograph (~500µm) of a sample with coarse moldic porosity (<300µm) from Unda at 65m, (plug porosity=37%, permeability=0.79mD). The pore spaces are mostly nonconnected open molds with completely cemented interparticle pore space (Anselmetti et al., 1998).

## 2.4 Elastic Properties

Seismic waves are the principle sources of information regarding the rock material and pore fluids within the earth's interior. Compressional and shear wave velocities are sensitive to changes in material properties and depend on factors such as, pore space amount, mineralogy, pore fluid content and the nature of the grain contacts (Murphy et al., 1993). The velocity-porosity crossplots display a general inverse correlation with large scatters around best fit curves (Figure 2.5). These variations could be clearly explained by variations in elastic rigidity and compressibility of the rock samples. Carbonates have the ability to form special fabrics that can lead to increased elastic properties without filling the pore space (Massaferro et al., 2002). Based on the equations for predictions of velocities high elastic moduli will result in higher velocities:

$$V_p = \sqrt{\frac{K + \frac{4}{3}\mu}{\rho}} \qquad \textbf{(2-2)}$$

and,

$$V_p = \sqrt{\frac{\mu}{\rho}} \qquad \textbf{(2-3)}$$

where K and μ are bulk and shear moduli, respectively. Therefore, the elastic behavior and rock framework of individual pore types should be studied to further discriminate the velocity variations in carbonates.

The bulk and shear moduli corresponding to the measurements were calculated from compressional- and shear-wave velocities (Equations 2.2 and 2.3), using the density measurements reported by Anselmetti and Eberli (1993) (Apendix A). Results are shown in Figure 2.14 where bulk and shear moduli show an inverse correlation with the porosity. If compared to Figure 2.5 of velocity-porosity crossplot, it can be seen that high velocities correspond to high elastic moduli. There is also a large scatter around exponential best-fit curves at porosities higher than 35%.

Figure 2.5 and Figure 2.14 show five dominant pore types that are characteristic of carbonate crocks with respect to elastic moduli and velocity. The stiff pores generally represent the rounded moldic pores or vugs and intraparticle pores in carbonate rocks. Intraparticle porosities are framestones and boundstones that form a rigid rock frame with better grain contacts resulting in positive departure from best-fit curves. The moldic porosity also has a self-supporting rigid framework comprising of cement and micrite that surrounds the molds. Coarse moldic pores have higher rigidities than fine moldic pores, hence resulting in higher elastic moduli and velocities. The interparticle and micro-porosity samples are generally insensitive to stress and have no preferred orientation. Hence, Interparticle/intercrystalline and micro-porosity results in low elastic moduli due to the absence of rigid framework with lack of cement or matrix and therefore these rocks exhibit lower sonic velocities

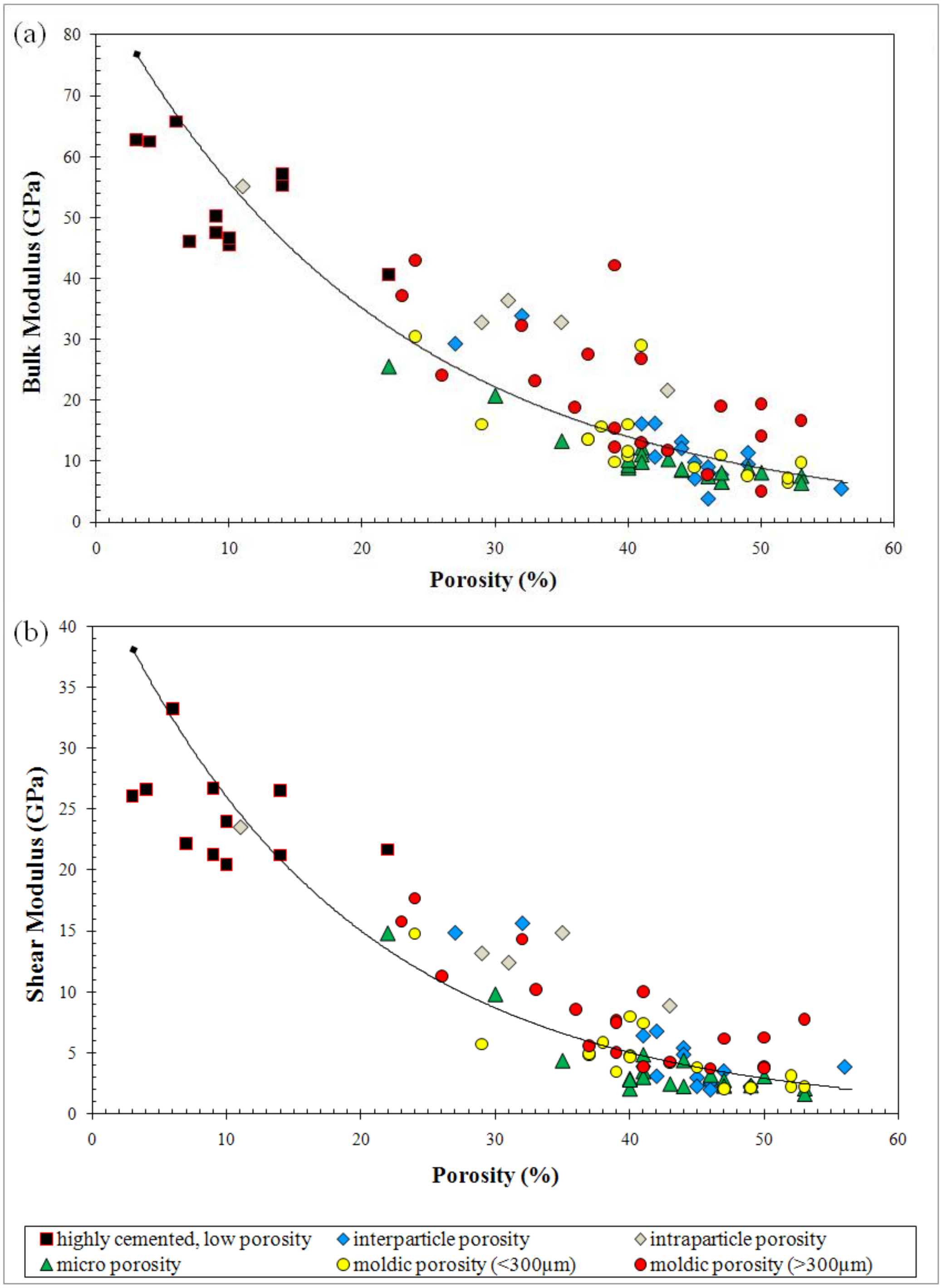

**Figure 2.14** A crossplot of bulk (a) and shear (b) moduli against porosity. Plots of porosity versus elastic moduli show an inverse trend: an increase in porosity produces a decrease in both bulk and shear moduli. There is also a large scatter around best-fit curves at porosities higher 35%.

## 2.5 Permeability

Pore types define the space that is available for fluid flow. Permeability is controlled by the difference in pore geometries, pore sizes and connectivity, rather than the total porosity (Blatt et al., 1980). The goal of this subsection is to find a correlation between carbonate pore geometries and permeability.

Permeability values were measured from 32 samples from Bahamas boreholes, which showed a high range of permeabilities from 0 to 678 millidarcies (md) (Anselmetti, 1994). The permeabilities on core plugs were determined by measuring the glow of nitrogen gas through plugs of known dimensions (Anselmetti and Eberli, 1993). The logarithmic plot of available permeabilities with porosity shows a general positive correlation (Figure 2.15a), while the permeability-velocity diagram shows a moderate negative correlation (Figure 2.15b). Due to limited number of permeability measurements available to us it is hard to make any reliable interpretations based on porosity/velocity data. Nevertheless, as seen from the plot we can suggest that different pore geometries result in different porosities, also causing variable permeabilities.

Highest permeabilities (678 md and 571 md) are recognized on two intercrystalline porosity samples, with fully connected sucrosic dolomites (Figure 2.15a and 2.15b); whereas the lowest permeabilities correspond to highly cemented and low porous samples, as expected. Most micro-porosity samples also show lower permeabilities despite of their high porosities. In other instances highly porous moldic pores exhibit low permeabilities where porosity does not contribute to permeability due to little connectivity between pores. This proves that the permeability in carbonates is not a function of total porosity, but rather a pore size and connectivity.

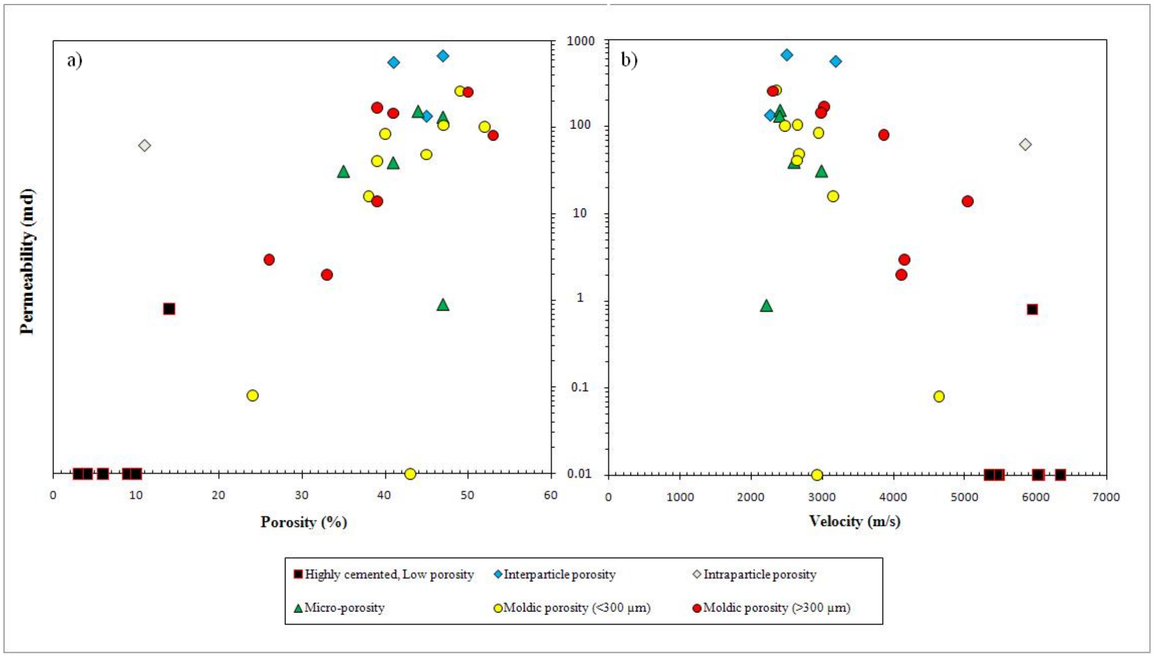

**Figure 2.15** Logarithmic plot of permeability with porosity (a) and velocity (b).

The minipermeameter permeabilities and neutron porosities were also measured by Anselmetti and Eberli (1993), this time to detect the effect of microporosity, macroporosity, and pore connectivity on permeabilities of 101 samples from both drillholes (Figure 2.16, 2.17). The amount of macroporosity were measured directly from point counting, included all pores large enough to identify petrographically, and generally pores >5µm (Anselmetti and Eberli, 1993). The amount of microporosity however was calculated indirectly from total porosity less macroporosity. The crossplot of permeability against neutron porosity (Figure 2.16) shows a large scatter with hardly any correlation. Nevertheless, when the pore connectivity is considered in a third dimension, a clearer relationship can be picked. The observation from the plot suggest that the high permeability carbonates is directly related to connected pores, while low permeability carbonates directly relate to disconnected and isolated pore spaces, neglecting any effect of total porosity.

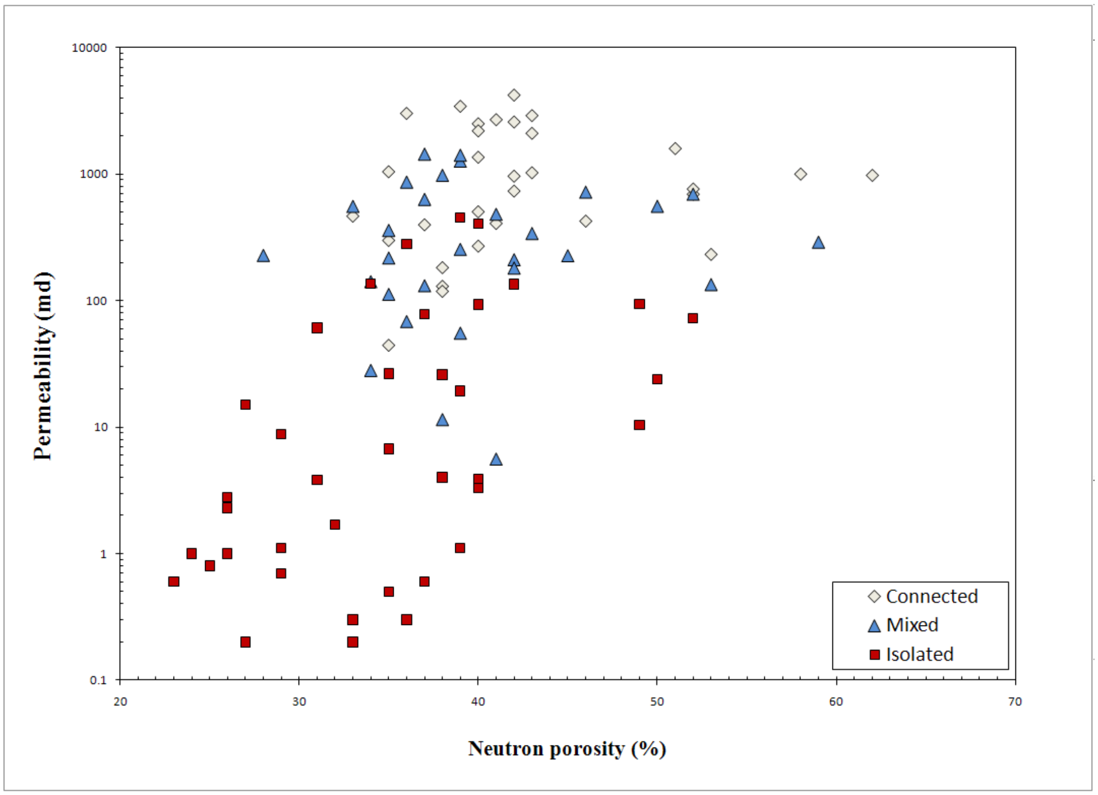

**Figure 2.16** Crossplot of minipermeameter permeability versus neutron porosity (N=101), with respect to pore connectivity of rock samples (adopted from Anselmetti and Eberli, 2003).

A crossplot of total macroporosity against permeability (Figure 2.17a) shows a better correlation than a crossplot of total microporosity against permeability (Figure

2.17b). This either indicates that macroporosity has a stronger influence on permeability than microporosity, or that the indirect measurement of microporosity does not allow a statistically-provable correlation to be used in discriminating the effect of microporosity on permeability. Hence, the role of microporosity on permeability is overshadowed by the much stronger influence of macroporosity as described by Anselmetti and Eberli. (2001).

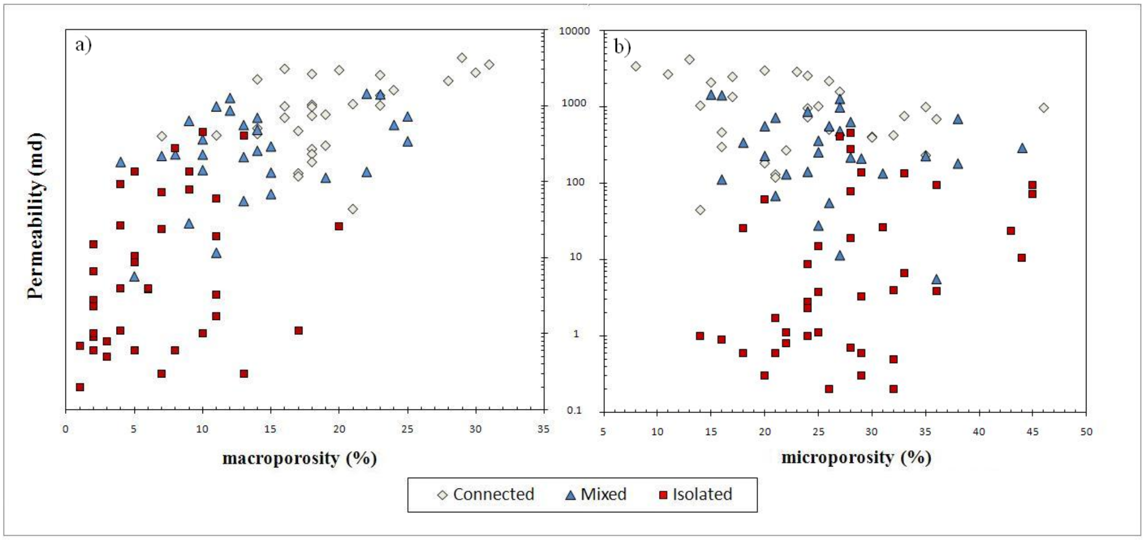

**Figure 2.17** (a) Permeability versus macroporosity derived from point counting. (b) Permeability versus microporosity measured indirectly (adopted from Anselmetti and Eberli, 2003).

## 2.6 Velocity Evolution with Diagenesis

This subsection will describe the effects of diagenesis on velocity evolution in carbonates using the velocity-porosity path (Figure 2.7). Carbonate rocks can follow a number of diagenetic events and stages through its burial history. Hence, finding the correct diagenetic pathway for carbonate rocks can be difficult depending on the diagenetic history and related pore geometries.

Diagenesis in carbonates is a very important process, which can alter the porosity and transform the sediment into a different rock type. Modern samples from Bahamas offer a great opportunity to study the velocity evolution of rocks at different diagenetic stages. Investigated samples have several stages of diagenetic history which lead to different pore types and have characteristic patterns on velocity-porosity diagrams (Figure 2.18). The velocity-porosity path of each sample starts at deposition and ends at their measured velocities, which correspond to final stage of their diagenetic history. Based on the thin section information Anselmetti and Eberli (1993) inferred the diagenetic evolution of four samples on velocity-porosity diagrams (Figure 2.18).

Figure 2.18a is an example of inferred velocity-porosity path of periplatform slope sediment with globigerinids. This sample is from Clino at 676 m depth with 44% porosity. Despite the deep burial depth this sample has undergone only little compaction, so that most *globigerina* shells are intact. Because of such limited diagenetic history, Anselmetti and Eberli (1993) described the velocity-porosity path of this sample with only a short arrow from conditions at deposition to present time.

Figure 2.18b represents a coarse moldic porosity of a former ooid-grainstone (oomoldic). After early consolidation the rock has undergone intense blocky cementation of marine waters, and later the dissolution of ooid grains leaving molds behind. Hence, the interparticle ooid grainstone has been transformed to coarse moldic porosity of 37%, leading to number of diagenetic stages. In concert, the diagenetic history of the rock resulted in more complicated loop shape.

Figure 2.18c corresponds to a highly cemented grainstone sample with only 9% porosity. The intense dolomitic cementation after the dissolution of components resulted in reduced porosity and increased velocity.

Figure 2.18d represents a sucrosic dolomite with 46% porosity. The dominant intercrystalline porosity has completely destroyed the depositional fabric leading to lower velocities than best-fit curve. As a result all described velocity-porosity paths were related to characteristic processes. Nevertheless, the absolute direction of the path depends on the succession and the timing of the different processes (Anselmetti, 1994).

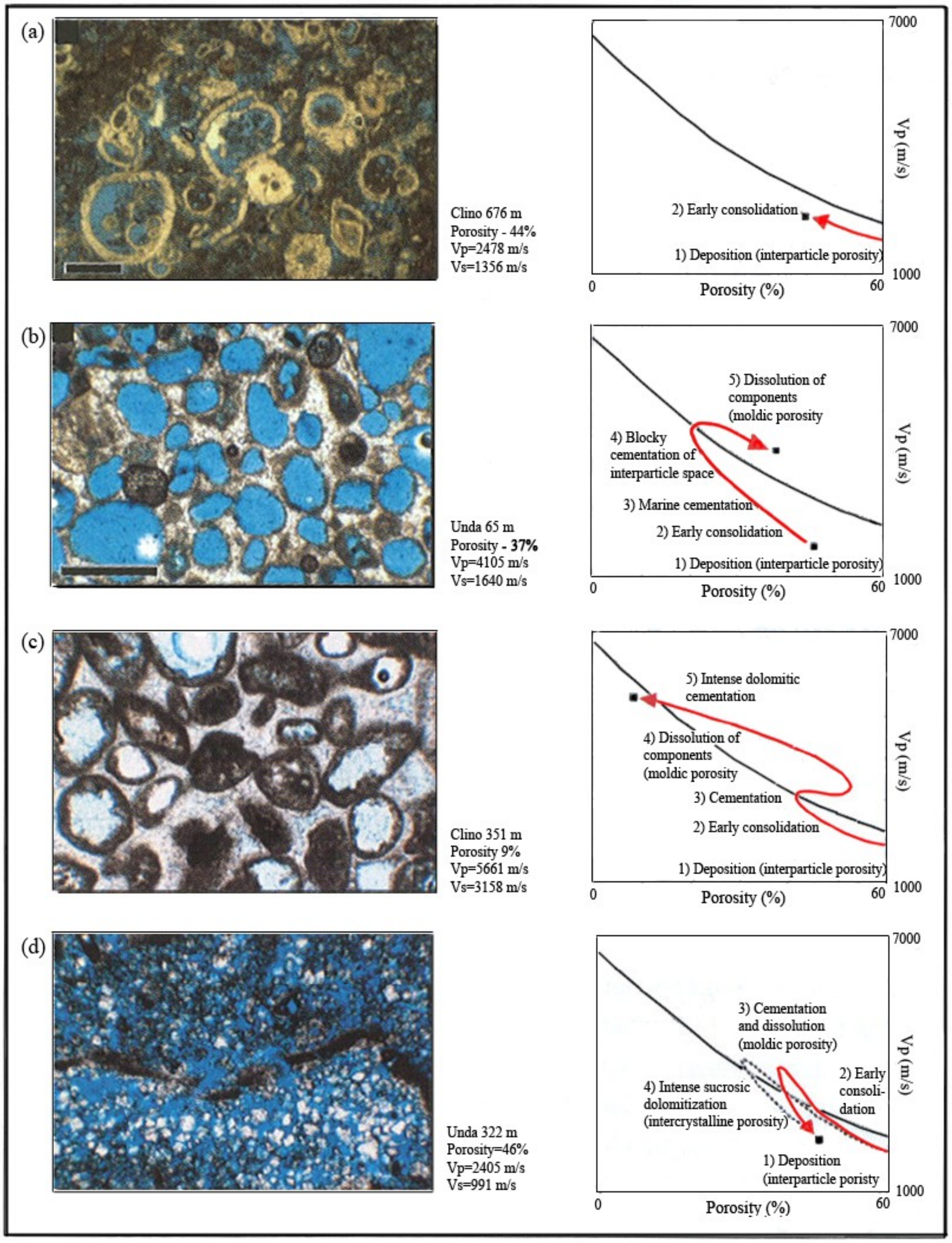

**Figure 2.18** Examples of inferred velocity-porosity paths for specific Bahamas samples shown in photomicrographs (left). The black square in the velocity-porosity diagrams (right) marks the measured velocity and porosity values for that sample. (a) micro-porosity; (b) coarse moldic porosity; (c) highly cemented, low porosity; (d) intercrystalline porosity (Anselmetti and Eberli, 1993; Massaferro et al., 2002).

## 2.7 Pressure Dependence Analysis

Laboratory ultrasonic velocities of all carbonate plugs were measured by Anselmetti and Eberli (1993) under varying effective pressures by increasing the confining pressure in a series of small steps of 2 MPa up to 80 MPa during which the pore pressure was kept constant at 2 MPa, to observe the pressure dependence of Vp (Figure 2.19f). All slow samples show an increase in compressional velocity with increasing effective pressure, whereas consolidated and dense samples are usually less affected by higher pressures, resulting in minimal gradients in the diagram.

Characteristic of many samples velocities can reach maximum values upon which a sudden decrease above a critical pressure can take place (Figure 2.19f). This increase and subsequent decrease in velocities is due to initial compaction of the sample in the pressure vessel, after which continuous collapsing can take place above critical pressure (Anselmetti, 1994). In contrast, other samples may exhibit a decrease in the gradient caused by disintegration of partly cemented grain contacts which are responsible for transmitting the acoustic signals. But eventually the velocities can increase again, as newly formed fractures in the sample are now being closed by further increase in effective pressure (Anselmetti, 1994). Depending on the lithology the critical pressure may vary. Soft, unconsolidated samples show lower critical pressures than dense, indurated rocks, which may show no signs of fabric destruction up to 100 MPa.

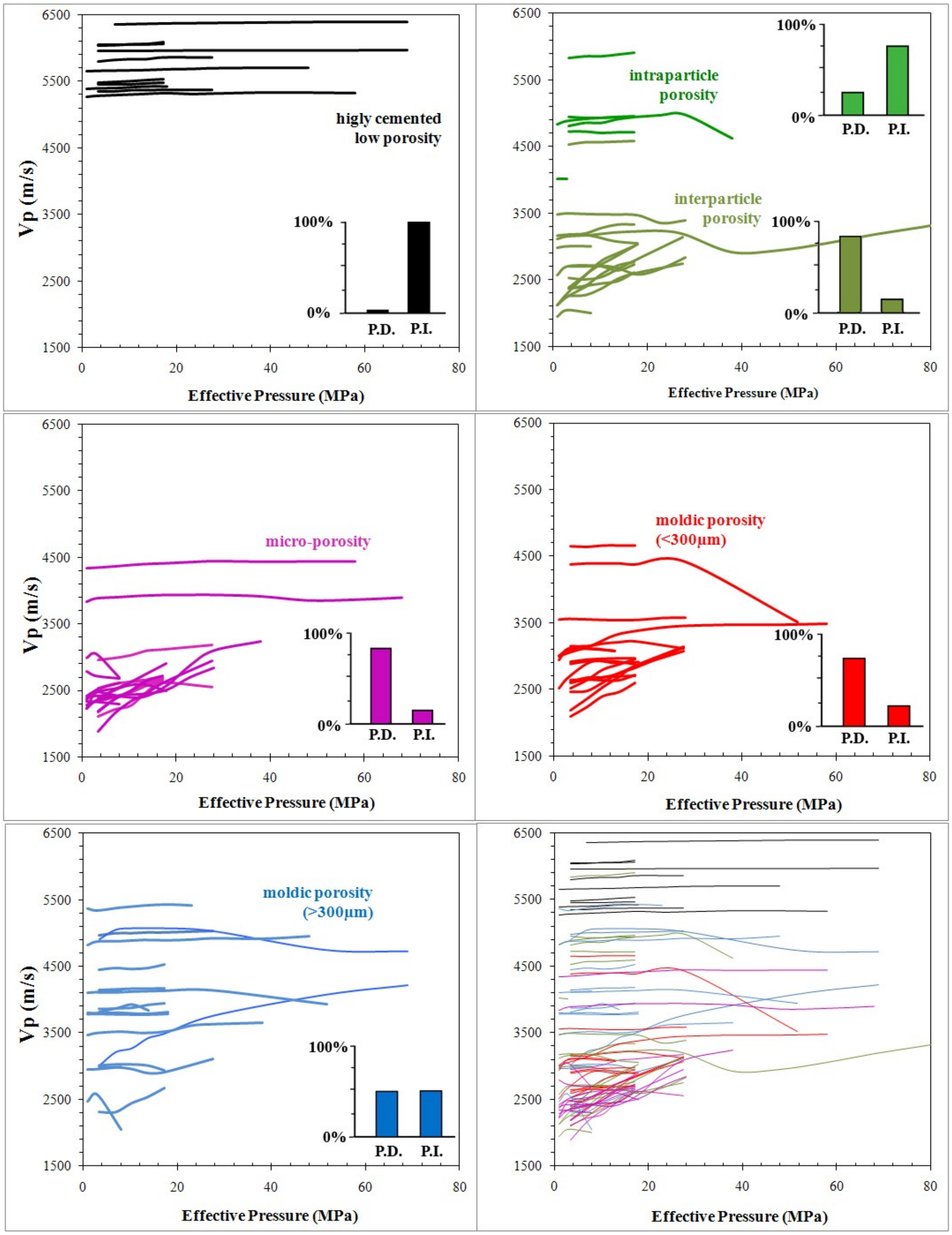

**Figure 2.19** Velocity of all samples at increasing effective pressures. Each trace represents the velocities at different pressures for different pore types. (a) highly cemented, low porosity; (b) interparticle porosity; (c) intraparticle porosity; (d) coarse moldic porosity; (e) fine moldic porosity; (f) All 89 samples at increasing effective pressures. P.D.-Pressure Dependent, P.I.-Pressure Independent (adopted from Anselmetti and Eberli, 1994).

The velocity evolution of carbonates under varying effective pressures also depends on the pore types and lithologies (Figure 2.19). Highly cemented, low porosity rocks display a systematic pattern of minimal gradients in the velocity-pressure plot (Figure 2.19a). These dense and indurated samples show almost no compaction or fabric destruction under increasing pressures. Rocks with interparticle porosity generally show increase in velocity with increasing pressure, whereas intraparticle porosity displays little variation in velocity as they are in general insensitive to stress due to their rigid framework (Figure 2.19b and 2.19c). Micro-porosity rocks are in general slow samples which show increase in velocities. Moldic porosity shows various behaviors under increasing effective pressures, depending on their pore size and connectivity. But the general trend indicates that fine moldic pores display more disintegration of the sample in the pressure vessel than more rigid coarse moldic pores (Figure 2.19d and 2.19e).

## 2.8 Conclusion

Carbonate rock samples from GBB have a wide range of pore types, rock textures and bulk porosities where rock age, mineralogy and origin were minor considerations. The goal of this study was to correlate variations in sonic velocities to lithology, porosity and predominant pore types. The five predominant pore types were classified as highly cemented, interparticle, intraparticle, micro- and moldic porosities. The measured velocities show a wide range of distribution and large scatter around best-fit curves. Thin section observations (Anselmetti and Eberli, 1993) revealed that GBB samples show limited variability in mineralogy, where calcite, dolomite and aragonite have somewhat very similar physical properties. Hence, the limited compositional variations were not held accountable for velocity contrasts in this province.

As in every other setting, we would expect the acoustic velocities in carbonates to be decreasing with increasing compaction and depth, where overburden pressure is an important process in reducing porosity. Nevertheless, Bahamian carbonates show little correlation with burial depth and age. Due to high susceptibility of carbonates to diagenesis, some diagenetic alterations such as cementation and dissolution can occur more rapidly prior to any compaction, either reducing or enhancing the porosity in the rock. Thus, burial depth and time are less pronounced in velocity trends of Clino and Unda.

We noticed clear relationship with sonic velocity and depositional environments, where shallow water carbonates have higher velocities and velocity contrasts than deeper water carbonates. Such velocity distribution among depositional environments can be explained with shallow water platform and reef sediments having higher content of metastable minerals (aragonite) and coarse grain sizes which are more prone to diagenesis than deeper water sediments.

The ultrasonic velocity measurements from GBB pure carbonate province reveals that sonic velocity and the permeability are not only a function of total porosity but also of the predominant pore geometries. The measured permeabilities showed no clear correlation with acoustic behaviors of our carbonate samples; however, samples with higher pore connectivity show higher permeability values than isolated pores. Our porosity-velocity correlation exhibits a general negative correlation, but significant deviations also exist. The velocity contrasts in the velocity-porosity relationship were related to different pore geometries. Pore types that are not embedded in a frame such as interparticle and micro-porosity result in lower velocities than certain moldic and intraframe porosities. Therefore, samples of equal porosity may exhibit different velocities due to presence of different pore types.

The velocity evolution of carbonates revealed that a sample passes though different stages in diagenesis resulting in different pore categories during its burial history. The velocity-porosity evolution in carbonates is not only a function of initial depositional lithology but also subsequent diagenetic alterations which can alter the rock frame and pore geometries transforming them to new pore categories (Anselmetti and Eberli, 2001).

The velocity as a function of effective pressure showed wide range of elastic behaviors under pressure vessel. Nevertheless, all velocity-pressure traces displayed in fact a systemic pattern for slow and fast samples. Slow samples show higher gradients where there is an increase in compressional velocity with increasing effective pressures. In contrast consolidated and dense samples with higher velocities are usually less affected by higher pressures, resulting in minimal gradients in the velocity versus effective pressure diagram.

# 3. CARBONATE ROCK-PHYSICS MODELS

## 3.1 Introduction

Rock-physics contains a link between intrinsic geological parameters (e.g., mineralogy, porosity, saturation, etc.) and quantitative geophysical measurements (e.g., sonic and elastic properties). However, developing an accurate and physically sound rock-physics model for carbonates hasn't been an easy task, representative of their complex pore geometries. Over the past couple of years, significant progress has been made in the study of various effects of carbonate rock types on sonic velocities (Rafavich et al., 1984; Wang et al., 1991; Anselmetti and Eberli, 1993; Eberli et al., 2003; Sayers, 2008; Xu and Payne, 2009); however no unified theory has yet been established. Therefore, the question remains: what is the physically sound, fundamental relationship between seismic wave velocities and the pore types in a carbonate system?

This section will focus ultimately on application of available rock-physics models in carbonates. A valid rock-physics model capable of quantifying the pore types is essential in effective characterization of carbonate rocks. Thus, the main purpose is to use a simple carbonate model to relate seismic signatures to subsurface carbonate geology or vise versa.

## 3.2 Sun Model, Frame Flexibility Factors

One of the major disputes in carbonates namely concerns the characterization of structural media with a representation of their internal structure (Sun, 2000). This subsection defines a simplified carbonate rock-physics velocity model that considers all dominant factors important for carbonate reservoir characterization.

Over the years, Biot's theory of wave propagation in porous media and its various modifications have been widely used in seismic reservoir studies (Russell et al., 2003). Based on extended Biot's theory of poroelasticity, a two-parameter elastic velocity model was derived. This velocity model introduced by Sun (1994, 2000) is able to effectively quantify the profound effect of pore structure and its connectivity on elastic property of the rock. Sun model (1994, 2000) defines key elastic parameters called "frame flexibility factors" that has been used previously by numerous authors for carbonate reservoir characterization (Massaferro et al., 2004; Gartner et al., 2005; Dou and Sun, 2008).

The frame flexibility factor introduced by Sun (1994, 2000) provides a proxy to the connectivity tensor in a very simplified form. This parameter characterizes the effect of pore structure, grain contacts and grain coupling, cementation and pore connectivity on the flexibility and elasticity of a porous rock (Sun, 2004). A set of working formulas for this model is:

$$V_p = \sqrt{\frac{K + \frac{4}{3}\mu}{\rho}} \tag{3-1}$$

$$V_p = \sqrt{\frac{\mu}{\rho}} \tag{3-2}$$

$$\rho = (1-\varphi)\rho_m - \varphi\rho_{fl} \tag{3-3}$$

$$K = (1-\varphi_k)K_m - \varphi_k K_{fl} \tag{3-4}$$

$$\varphi_k = \varphi F_k \tag{3-5}$$

$$F_k = \frac{K_m - K}{\varphi(K_m - K_{fl)}} \tag{3-6}$$

$$f = \frac{1 - \frac{K_{fl}}{K_m} + 1 - \frac{K_{fl}}{K_m} \varphi \ F_k}{(1-\varphi) \ 1 - \frac{K_{fl}}{K_m} F_k} \tag{3-7}$$

$$\mu = \mu_m(1-\varphi)f_\mu \tag{3-8}$$

$$f = (1-\varphi)^{\gamma-1} \tag{3-9}$$

$$f_\mu = (1-\varphi)^{\gamma_\mu - 1} \tag{3-10}$$

$$c = \gamma_\mu / \gamma \tag{3-11}$$

where;

$\rho$ – bulk density,

$K$ – bulk modulus of the fluid saturated rock,

$\mu$ – shear modulus,

$\rho_m$ – solid matrix density,

$K_m$ – solid matrix bulk modulus,

$\mu_m$ – solid matrix shear modulus,

$\rho_{fl}$ – fluid density,

$K_{fl}$ – fluid bulk modulus,

$\varphi$ – porosity,

$f, f_\mu$ – frame stiffness/rigidity factors,

$\gamma, \gamma_\mu$ – frame flexibility factors or coupling coefficients,

$c$ – gamma ratio.

The $f$ factor in Equation (3-7) is a function of porosity, whereas, it is assumed that $\gamma$ and $\gamma_\mu$ are independent of porosity. The $\gamma$ and $\gamma_\mu$ parameters are bulk and shear coupling coefficients, also referred to as the frame flexibility factors. The frame flexibility factor, $\gamma$, is introduced to characterize the combined effects of crack density, pore shape, and grain-to-grain coupling on elastic deformation (Sun, 2000). They characterize the flexibility of the rock when subject to compressional and shear motion, respectively (Sun, 2000). Because these frame flexibility factors are less dependent on porosity than wave velocities, they can be related to pore structure, as well as pore connectivity and grain size. Generally, higher $\gamma$ values can be related to less grain contacts and grain coupling. However, diagenesis in carbonates can create special rock textures that would result both in very high pore-connectivity as well as, rigid rock frame with better grain contacts (e.g., intraparticle porosity, moldic porosity). Hence, such frameworks may result in lower $\gamma$ values (Sun, 2004).

For the purpose of our rock-physics study, the frame flexibility factor values for all 89 Bahamian samples were calculated, as tabulated in the Appendix B. Using those values, different porosity-velocity trends can be characterized (Figure 3.1 and Figure

3.2). The study shows that for core samples at a given porosity, the lower the frame flexibility factors the higher the sonic wave velocities. Samples with the frame flexibility factor values ($\gamma$, $\gamma_\mu$) less than 4 are generally either rocks with visible moldic pores or intraframe porosity of framestones and boundstones (Figure 3.2). Quite the reverse, samples with the frame flexibility factor values greater than 4 are commonly sucrosic dolomites with dominant intercrystalline porosity, dominant micro-porosity with high micritic content, or densely cemented, indurated rocks (Figure 3.2).

As seen in Figure 3.2, the highly cemented, low porosity rocks correspond to the top right hand corner of the graph. Despite of strong grain connectivity and coupling within their rock framework, these samples show highest frame flexibility values. This is mostly governed by highly cemented rock frame and very little pore connectivity. These samples are also characteristic of low permeabilities in lab measurements. Three samples, however, show lower frame flexibility values than expected. In other words, these samples show higher flexibility of the rock frame under compressional and shear deformation. Based on the lithostratigraphic data maintained during Bahamas Drilling Project (Ginsburg, 2001), those samples can be identified as subearial exposure sediments superimposed on an erosional surface or the sequence/depositional boundary (Kenter et al., 2001). Such lithostratigraphic sites on the deposition may have resulted in higher pore connectivity relative to the established diagenesis, which consequently led to lower gamma values.

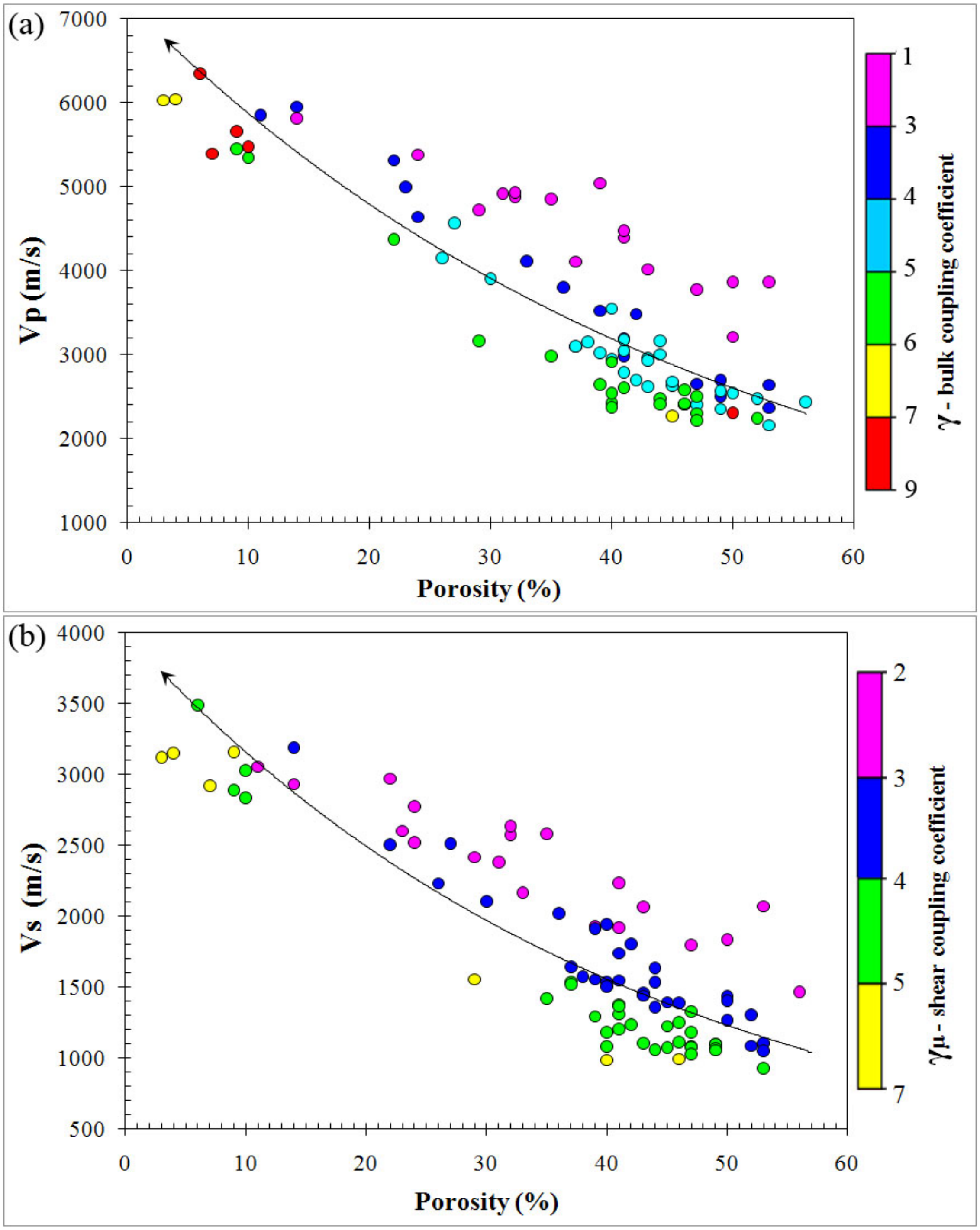

**Figure 3.1** Velocity-porosity crossplot in respect to frame flexibility factors. (a) Compressional-wave velocity (Vp) in relation to γ-bulk coupling coefficient; (b) Shear-wave velocity (Vs) in relation to $\gamma_{\mu}$-shear coupling coefficient.

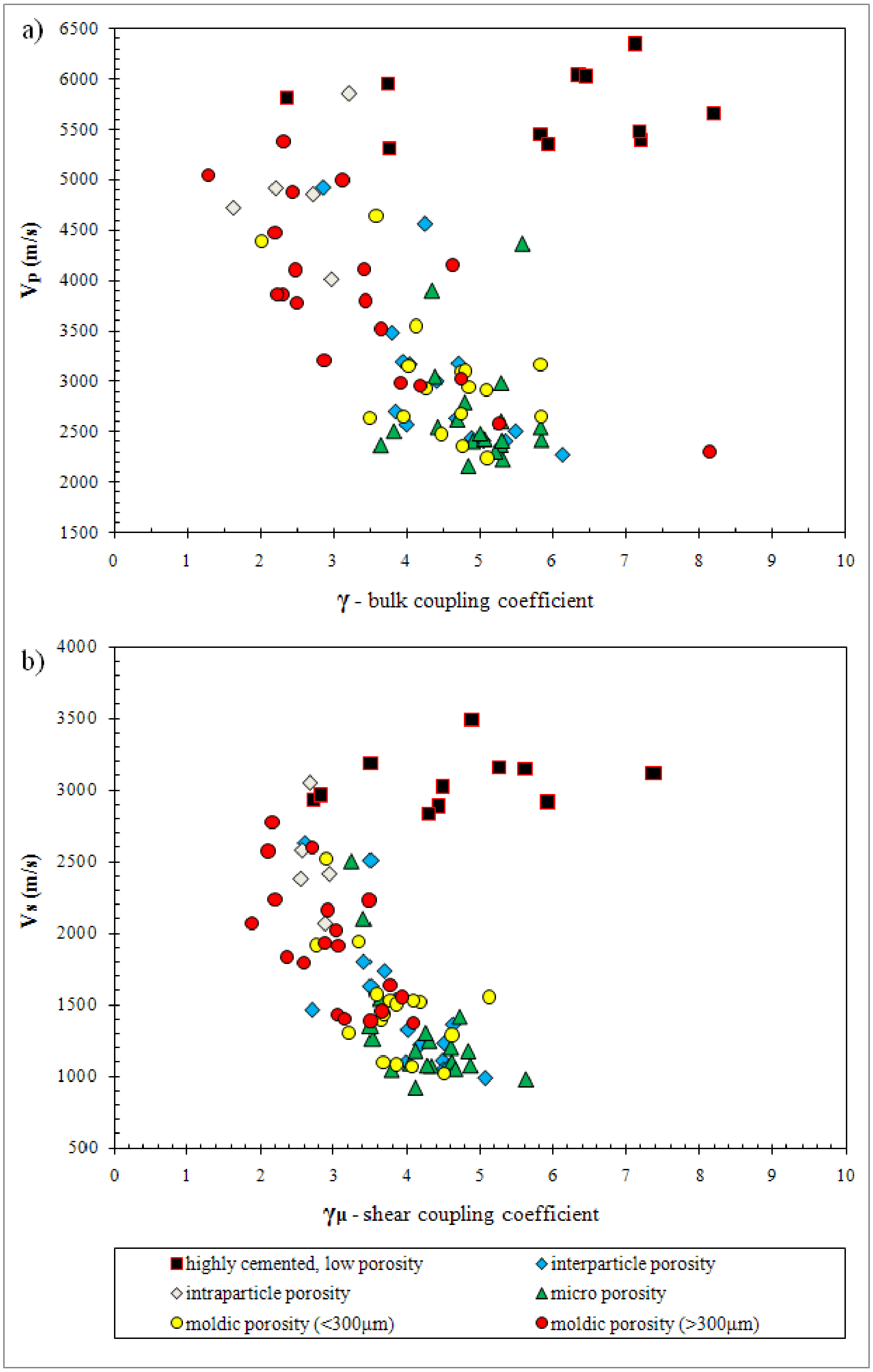

**Figure 3.2** The frame flexibility factors versus velocity diagram. (a) γ-bulk coupling coefficient vs. P-wave velocity, (b) $\gamma_\mu$-shear coupling coefficient vs. S-wave velocity.

Rocks with micro-porosities show consistent frame flexibility values ($3<\gamma$, $\gamma_\mu<6$). As mentioned before in Section 2.3, micro-porosity samples from GBB have extraordinarily high porosities, due to lack of cementation that results in an unconnected grain fabric; hence, the frame flexibility factors are relatively high. Nevertheless, these rocks have lower permeabilities than expected from their porosity. Only two microporosity samples fall out of the general cluster, corresponding to higher velocities and lower porosities (Figure 3.2). Yet, the coupling coefficients are not affected by such porosity anomalies, as these values are independent of porosity. Interparticle porosity in framestones and boundstones has flexibility values similar to those of micro-porosity.

Moldic pores generally show lower $\gamma$ and $\gamma_\mu$ values, owing it to their constructional framework with a porosity that is embedded in the solid frame. That is to say, the high elastic rigidity framework leads to lower deformation under compressional and shear motion. Moldic porosity, depending on the size of the pores (coarse and fine) and their level of connectivity may show different frame flexibilities in rocks with the same porosity. One other thing to recognize from the plot (Figure 3.2) is that coarse moldic pores show lower coupling coefficients than fine moldic ones. The lower frame flexibility values of coarse moldic pores indicate better grain contacts and more rigid rock frame than fine moldic pores.

The $f$ parameter describes the stiffness and the rigidity of the rock frame under deformation, depending on the pore structure as well as the porosity (Sun, 2004). Our study shows that for core samples at a given porosity, the lower the frame stiffness/rigidity factors the lower are the sonic wave velocities (Figure 3.3). As seen in

Figure 3.4, rocks with micro- and intercrystalline porosity display lower frame stiffness/rigidity values (≤0.3), relative to moldic, intraparticle and low porosity rocks (≥0.3). Lower $f$ (stiffness) and $f\mu$ (rigidity) values relate to rocks which can deform easily under compressional and shear motion, whereas rocks with high frame stiffness/rigidity factors are in general insensitive to stress and have high elastic rigidity of the rock frame. However, Figure 3.4 displays a large scatters around best-fit exponential curves. Based on the plots we can infer that these large deviations are due to the elastic behavior of mainly intraparticle and moldic porosities. As previously mentioned in Section 2, both of these pore types forms a special self-supporting framework with high elastic rigidity, leading to different values in frame stiffness/rigidity factors than expected from the general trend. In Figure 3.5, it also appears that higher $f$ and $f\mu$ values relate to higher stiffnesses (higher bulk moduli) and higher rigidities (higher shear moduli) respectively.

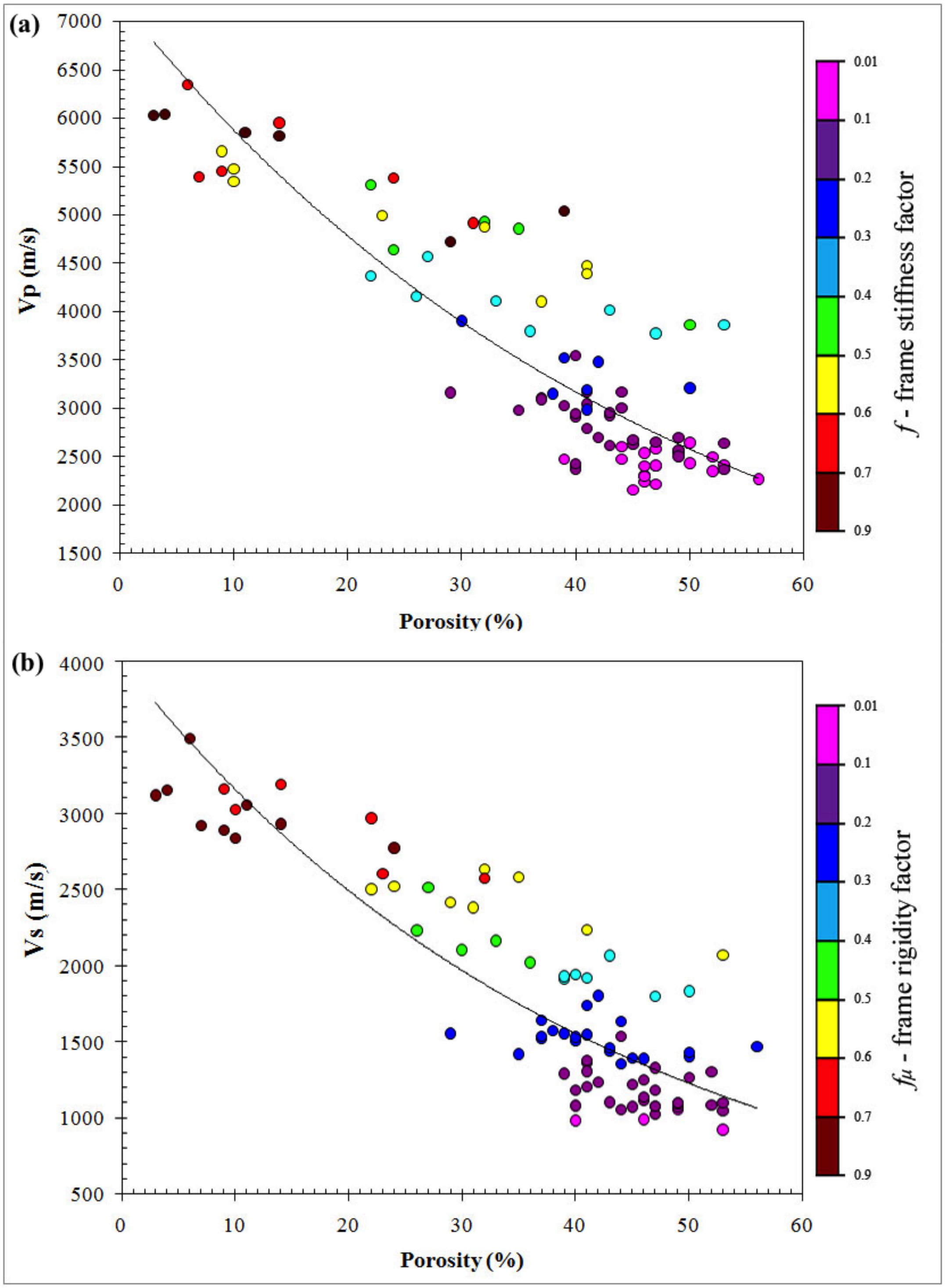

**Figure 3.3** Velocity-porosity crossplot in respect to frame stiffness/rigidity factors. (a) Compressional velocity (Vp) versus porosity relative to *f*-frame stiffness factor; (b) Shear velocity (Vs) versus porosity, relative to *fμ*-frame rigidity factor.

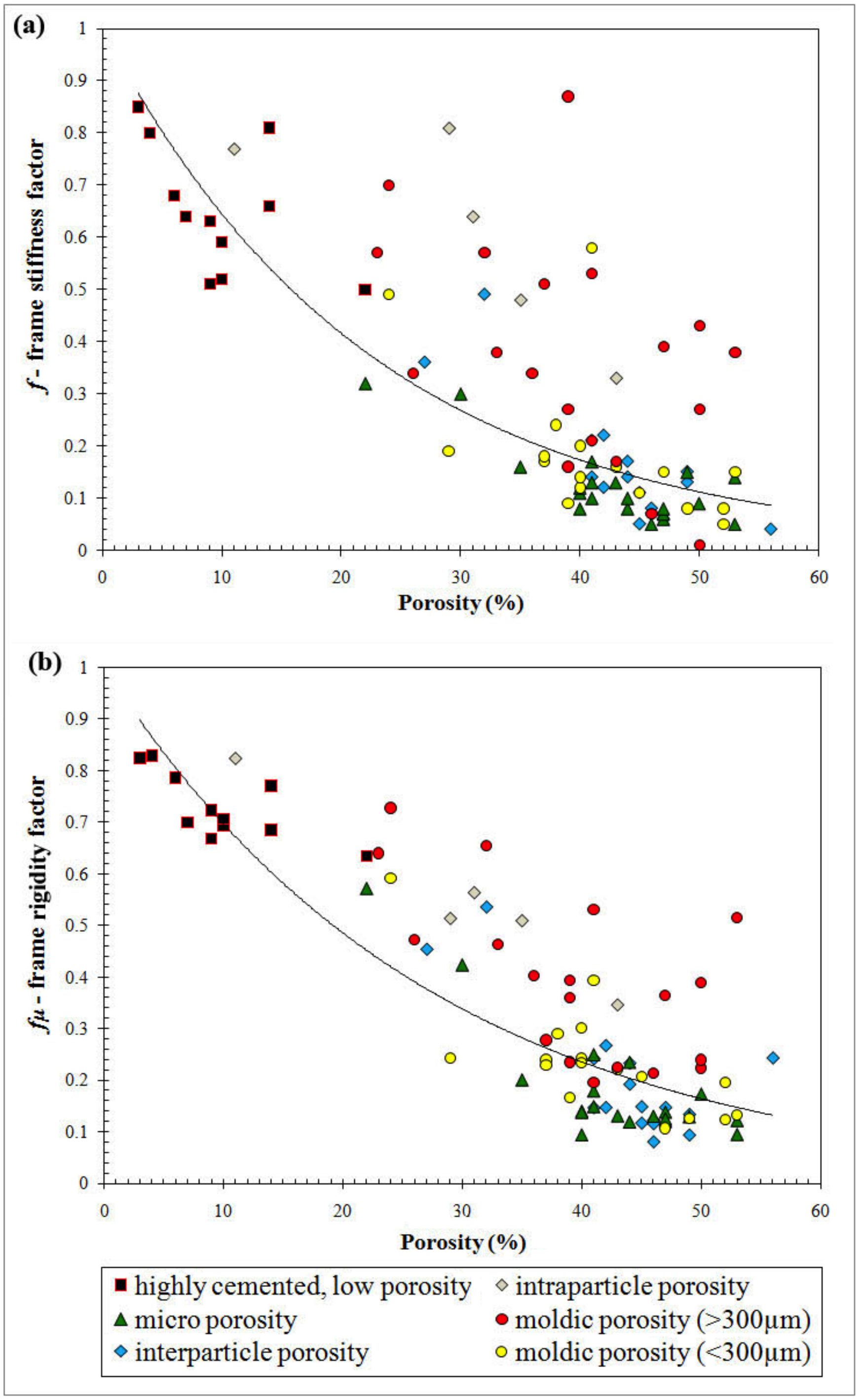

**Figure 3.4** Frame stiffness factors *f* (a) and *fμ* (b) versus porosity. Notice how frame stiffness factors depend both on pore structure and the total porosity. This figure also quantifies the ease of the rock frame (especially rocks with intraparticle and coarse moldic porosity) to undergo shear motion relative to its compressibility.

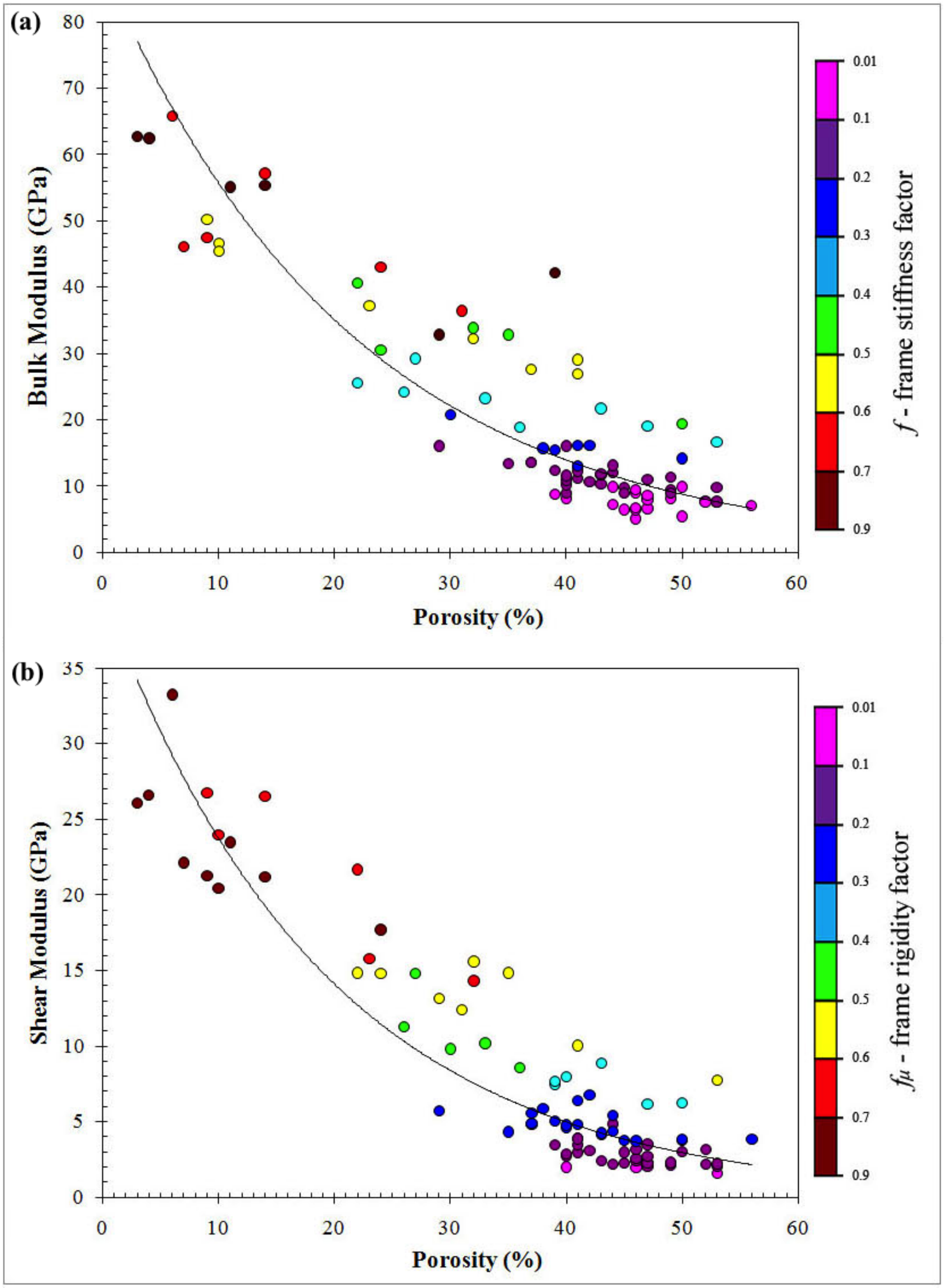

**Figure 3.5** Elastic moduli versus porosity crossplot in respect to frame stiffness/rigidity factors. (a) Frame stiffness factor versus bulk modulus; (b) frame rigidity factor versus shear modulus.

The gamma ratio ($c = \gamma_\mu/\gamma$) is another very important physical parameter in Sun's model (1994, 2000) that quantifies the shear deformation relative to compressibility. For two difference rock frames that have the same frame compressibility, they may have different resistance to shear motion owing to their different pore shapes (Sun, 2004).

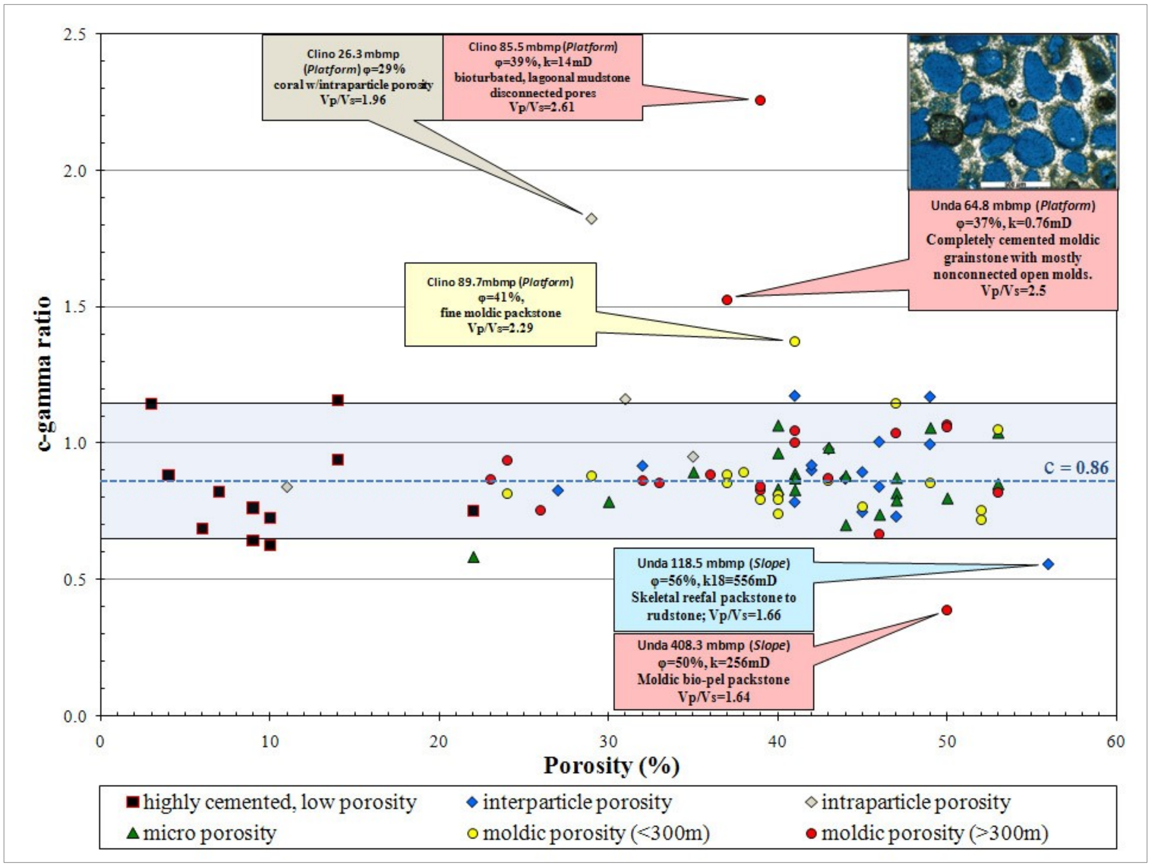

**Figure 3.6** Gamma ratio versus porosity. c=0.86 is the arithmetic mean value of gamma ratio for Bahamian dataset. Most samples cluster around the average mean value (dashed line).

As $\gamma$ and $\gamma_\mu$ are theoretically assumed to be independent of porosity to derive the Equations (3-10 and 3-11), gamma ratio would also be somewhat constant over range of porosities (Figure 3.6). The average gamma ratio, c, can be approximated using all the values determined from the core plugs or even at the well location from logs in the studied field. The average gamma ratio for our samples is equivalent to 0.86. However, several samples mainly of moldic porosity deviate from this value. Samples, which generate positive departure from the general scatter, are shallow depth (20-80mbmp), low permeable, bioturbated lagoonal mudstones or highly cemented skeletal lithoclasts with intraparticle porosity, all of which are platform sediments with extensive meteoric diagenesis. These samples have low permeabilities regardless of their high porosities. On the contrary, samples, which display negative departure from the general cluster, are highly permeable, highly porous skeletal packstones with questionably lower velocities.

The main purpose of having a single average gamma ratio, c, value is to be able to later estimate a good approximate for $\gamma_\mu$, and the pseudo-shear wave velocity from sonic (Vp) log where the shear log data is not available (Sun, 2004):

$$V_s = \sqrt{\frac{\mu_s (1-\varphi)^{c\gamma}}{(1-\varphi)\rho_s + \varphi \rho_{fl}}} \tag{3-12}$$

Figure 3.7 displays a general uniform relationship between gamma ratio and Vp/Vs ratio. Samples, which display large deviations from average gamma ratio (Figure 3.6), also correspond to endmember sonic velocity ratios (either very high or very low). From Figure 3.7 we can also relate high sonic ratios to high porosities with low permeabilities (micro-porosity and isolated moldic porosity). The lowest sonic ratio (1.6-1.7) in three highly porous samples may be the result of questionable shear-wave signals and have to be judged with caution (Anselmetti and Eberli, 2001).

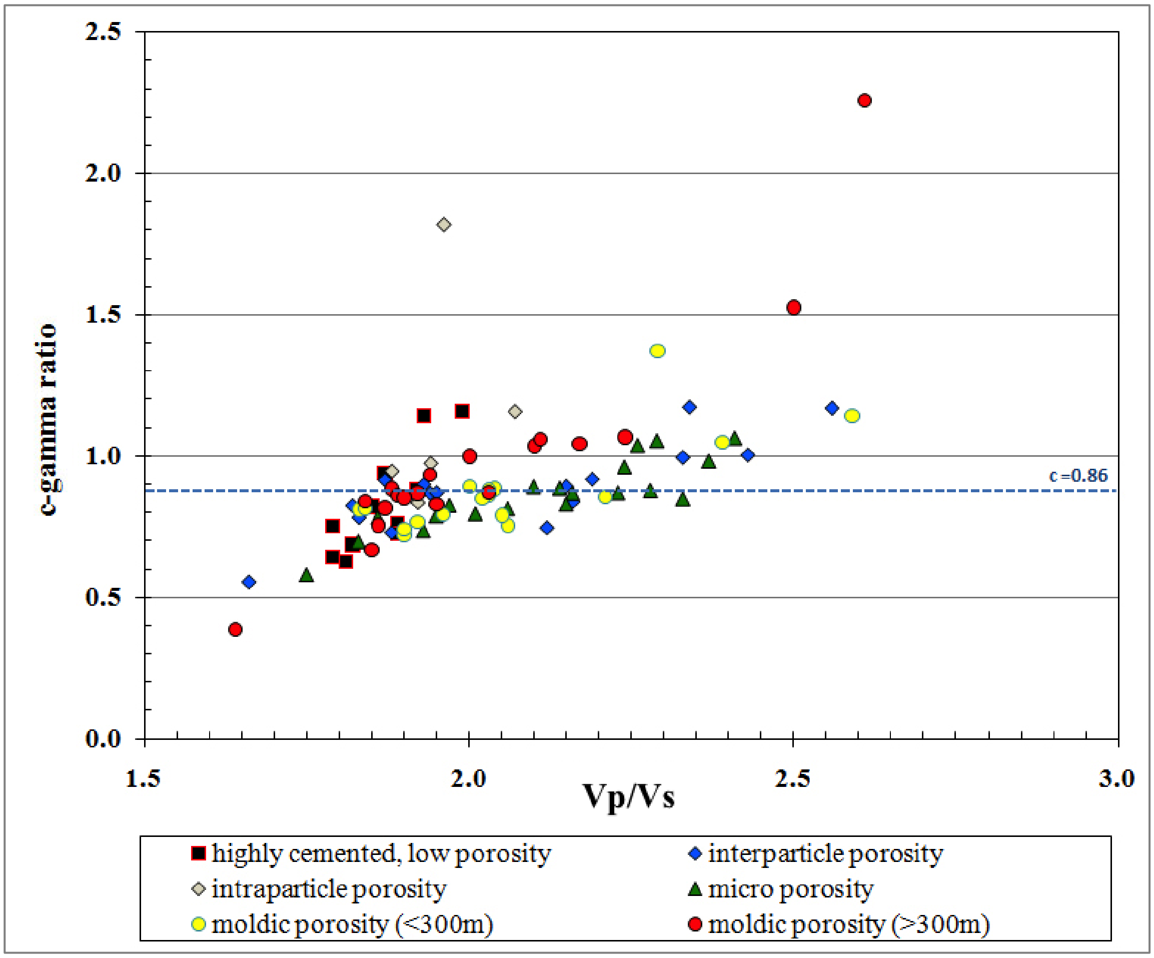

**Figure 3.7** Gamma ratio versus the sonic ratio. Notice the uniform relationship along c=0.86 line, while only number of samples show deviations from the general cluster.

If samples with gamma ratio values outside the general cluster to be excluded from the dataset, a straightforward gamma ratio-sonic ratio relationship can be obtained (Figure 3.8). Gamma ratio is especially helpful in determining the relationship between coarse and fine moldic pores.

In our previous plots (Figure 2.7) moldic porosities displayed the most unpredictable velocity-porosity trends. In gamma ratio against velocity ratio crossplot (Figure 3.8d), however, coarse moldic porosity displays higher correlation coefficient than fine moldic porosity. As coarse moldic porosities generally exhibit higher flexibility of the frame under shear deformation ($\gamma_\mu > \gamma$) than compared to fine moldic porosity, the gamma ratio values are also relatively higher for coarse moldic pores. The same is also applicable in interparticle versus intraparticle porosity rocks, where intraparticle pores exhibit higher gamma ratios and hence, lower shear deformation relative to interparticle porosity.

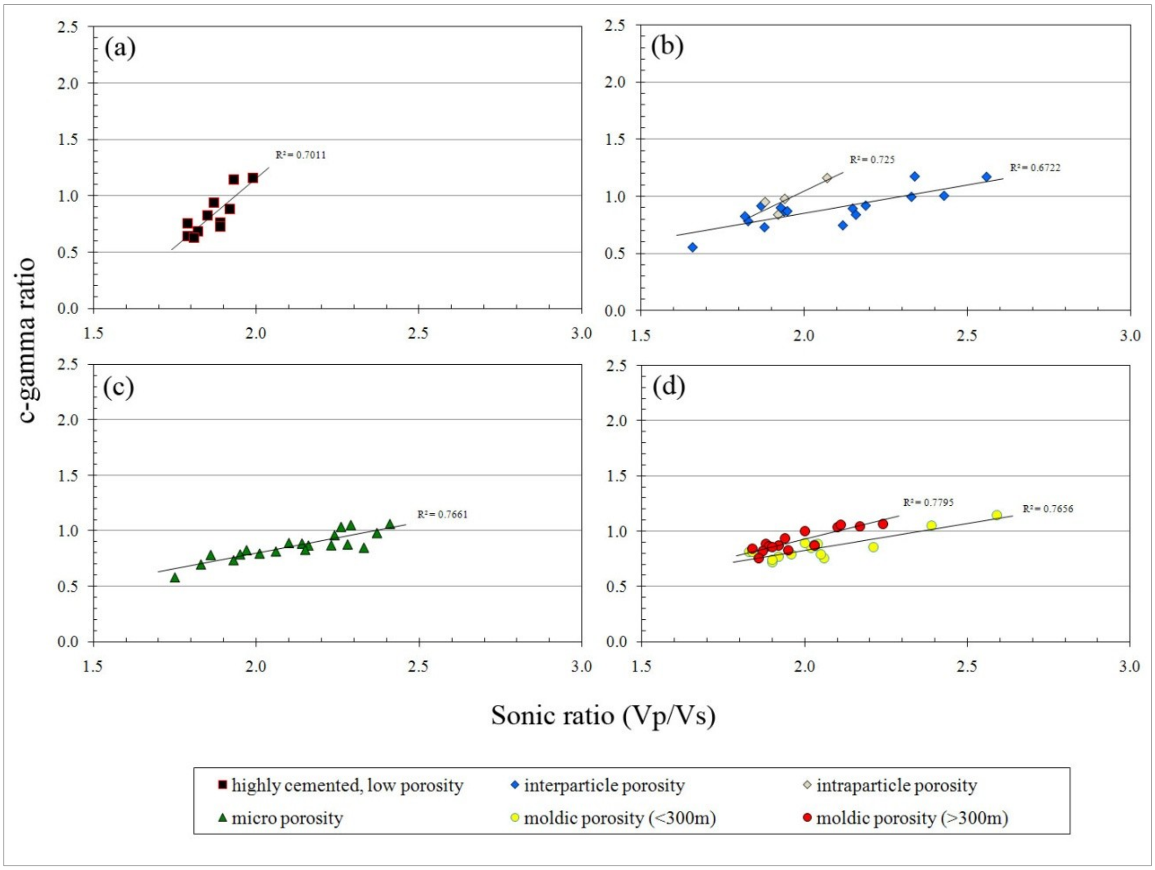

**Figure 3.8** Gamma ratio relative to sonic ratio. (a) highly cemented, low porosity, (b) interparticle and intraparticle porosity, (c) micro-porosity, (d) coarse and fine moldic porosity

## 3.3 Pore Stiffness Model

So far we related Sun (2000, 2004) model to lithology and respective carbonate pore structures. However, elastic parameters, such as frame and pore compressibilities in particular, are essentially important in quantification of pore structures in carbonates. Relating the velocity to elastic moduli, which are expressed as the intrinsic measures of the rock frame and pore space compressibilities, can be the best way to perform quantification of sonic measurements in terms of material properties. The two main elastic moduli are known as the shear and bulk frame moduli, which are functions of the porosity (Figure 2.14). The measured velocities depend on the pore fluid compressibilities, while the pore space may be filled with one or more fluids. The inversion of the velocities to the frame and fluid moduli may distinguish the fluid saturation effects, which can ascribe the different pore fluids (e.g., oil and gas from water).

Biot (1956) poroelasticity theory provides a general framework for prediction of sonic velocities,

$$\rho_c V_p^2 = K_\varphi + K_{dry} + \frac{4}{3}\mu \tag{3-13}$$

$$\rho_c = \varphi\rho_{fl} + (1-\varphi)\rho_m \tag{3-14}$$

$$\rho_c = \varphi\rho_{fl} + (1-\varphi)\rho_m \tag{3-15}$$

where;

$K_{fl}$ – pore space bulk modulus,

$K_{dry}$ – dry rock bulk modulus,

$\mu$ – wetted frame shear modulus,

$\rho_c$ – composite or total density,

$\rho_{fl}$ – fluid density,

$\rho_m$ – matrix density.

As seen from Equation (3-14), the dependency of shear wave velocity on fluid characteristics is rather weak and enters through $\rho_c$. The compressional velocity in Equation (3-13), however, involves the pore space modulus $K_\varphi$. Pore stiffness is the inverse of the rock space compressibility at a constant pore pressure (Russell and Smith, 2007). Betti-Rayleigh reciprocity theorem introduces a relationship where pore space stiffness, $K_\varphi$, is related to the dry rock bulk modulus, $K_{dry}$, the mineral bulk modulus, $K_m$, and the porosity (Mavko and Mukerji, 1995):

$$\frac{1}{K_{dry}} = \frac{1}{K_m} + \frac{\varphi}{K_\varphi} \tag{3-16}$$

The equation 3.16 is also the direct physical link between the dry and fluid-saturated moduli, and is therefore the basis of Gassmann's equation for fluid substitution. The pore space compressibility of a rock provides a model-independent descriptor of porosity and pore type effect on effective moduli (Baechle et al., 2006). Figure 3.9 is the crossplot of Kφ against porosity/velocity, although for certain pore types significant deviations are present. Densely cemented, indurated rocks, generally, have low porosities and high velocities, corresponding to higher pore stiffnesses in the diagram. Interparticle, fine moldic and micro-porosity on the contrary display the lowest Kφ values in the crossplots. Coarse moldic and intraparticle porosities show similar relationships to highly cemented, low porosity rocks, displaying one of the highest pore stiffness values. Even though creation of vuggy porosity will increase porosity, this will not necessarily increase the pore space compressibility. Hence, the pore space stiffness will be higher for most of these samples, as acoustic energy potentially bypasses the pore space in the surrounding stiff frame.

In order to quantify the velocity deviations at a given porosity Baechle et al. (2006) introduced a new variable – $k$, which represents the ratio of pore space stiffness over mineral modulus.

$$k = K_{\varphi} / K_{m} \tag{3-17}$$

Pore space stiffness ($k$) provides a non-linear porosity-bulk modulus trend of specific carbonate pore types. Constant $k$ values of 0.5, 1.0, and 2.0 generate trend lines in the normalized bulk modulus-porosity diagram (Figure 3.10). By generating constant $k$ trends in the diagram we can link normalized constant pore space stiffness values to endmember carbonate pore types. The dataset demonstrates a non-linear feeble relationship between pore space stiffness ($k$) and specific pore types over wide range of porosities. Carbonate rocks having only micro-porosity, fine moldic porosity (<300µm) and interparticle/intercrystalline pores generally manifest lower normalized pore space stiffness values; whereas highly cemented, low porosity rocks show distinctive higher values of around 0.2. Coarse moldic (>300µm) and intraparticle pores attenuate around $k$ trendlines, depending on their level of connectivity, which exhibit less accountable outcomes.

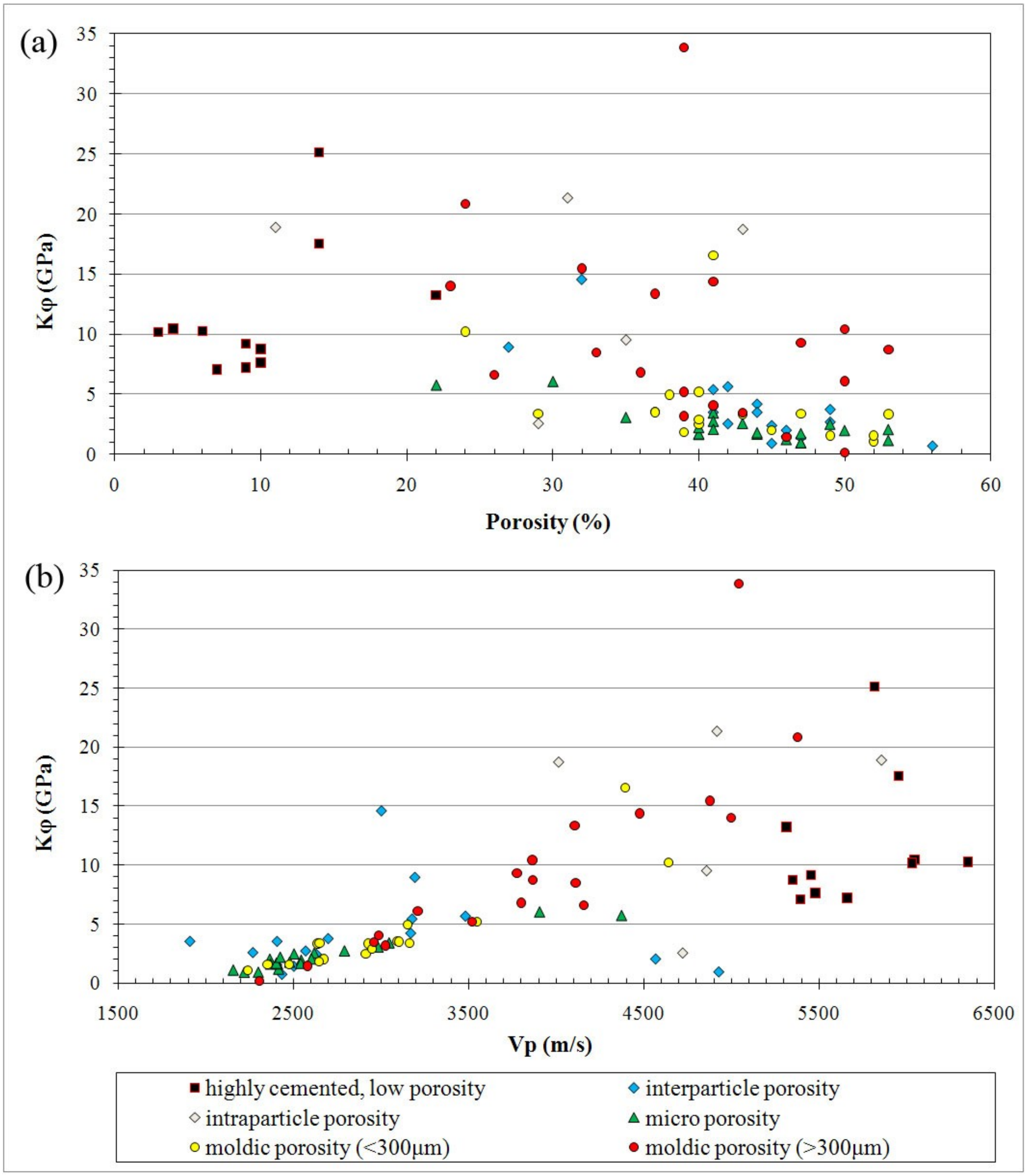

**Figure 3.9** Pore space compressibility ($K_{\varphi}$) relative to (a) porosity and (b) compressional velocity (Vp). $K_{\varphi}$ displays a general decreasing and increasing trends with porosity and Vp, respectively.

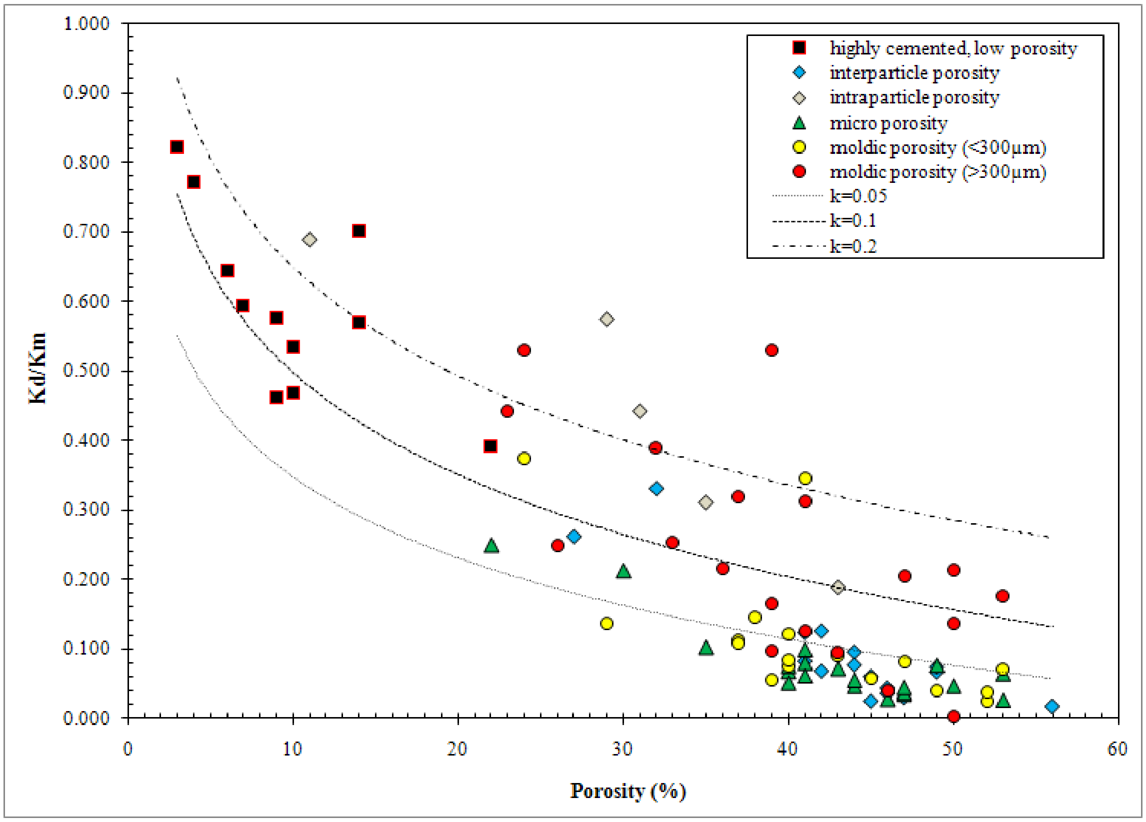

**Figure 3.10** Normalized bulk modulus and porosity diagram with constant pore stiffness (k) trend lines representing a non-linear relationship between pore space stiffness and specific pore types over wide range of porosities.

## 3.4 Frame Flexibility Factor and Pore Space Stiffness

So far our deterministic approach of individually linking Sun model (2000) and pore stiffness model to carbonate pore geometries has produced meaningful results which fit well with our qualitative pore structure observations. Nevertheless, finding a relationship between pore compressibility and frame flexibility factors could further delineate how porosity and pore geometries affect the mechanical response of porous carbonate medium to compressional motion.

As mentioned before, frame flexibility factors are independent of porosity, and the more flexible the frame is, the larger the $\gamma$ and $\gamma_\mu$ values would be for a given porosity. Physically, this also implies that the harder the formation (better coupling), the smaller the values of these frame flexibility factors would be as in intraparticle and moldic porosity rocks (Sun, 2000). Based on the equation derived from extended Biot (1956) theory, we can relate dry bulk modulus to the compressibility of the mineral matrix through bulk coupling coefficient – $\gamma$ (Sun, 2000):

$$K_d = K_m(1-\varphi)^\gamma \tag{3-18}$$

In retrospect, however pore space stiffness is the inverse of the pore space compressibility at a constant pore pressure and is related to the dry rock and mineral bulk modulus, along with porosity (Equation 3.16). In concert with the Equations 3.16 and 3.18 we can now relate pore space compressibility to bulk coupling coefficient as follows:

$$K_\varphi = \frac{\varphi K_m^2(1-\varphi)^\gamma}{K_m(1-(1-\varphi)^\gamma)} \tag{3-19}$$

Figure 3.11 shows that for a given porosity the pore space stiffness increases with decreasing frame flexibility factor. The peculiar manner in which the pore stiffness value shifts towards a higher value in low porosity carbonates with dense, regular cementation is attributable to high flexibility (better coupling) of the rock. Primary porosities (micro-porosity and interparticle/intercrystalline porosity) generally show gamma values between 4 and 6. Samples with micro- and interparticle porosity have less grain contacts and grain coupling due to lack of cementation, which results in an unconnected grain fabric, hence low resistance to uniform compression. Fine moldic pores have higher gamma values than coarse moldic ones, due to less rigid rock-frame and higher pore connectivity. Hence, fine moldic porosity falls within a range of high compressibility. Coarse moldic pores show two different behaviors. While some coarse moldic samples show higher gamma values and high pore stiffnesses, others exhibit lower gamma values and little pore compressibility due to strong and more rigid framework. Generally, samples with gamma values of 2-3, are all shallow water platform and reef deposits, which also correspond to higher velocities (Figure 3.9).

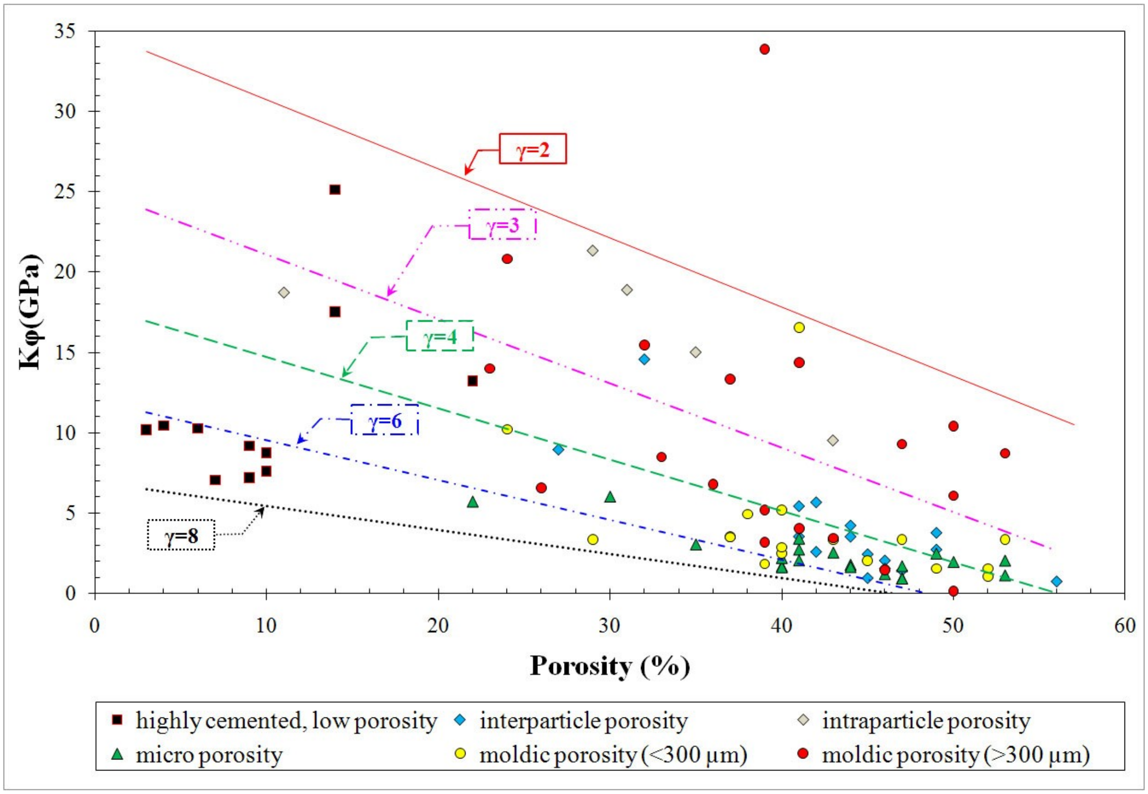

**Figure 3.11** Pore space compressibility versus porosity with respect to constant gamma values. General trend shows that the higher the gamma values the lower is the pore space stiffness of the rock.

The crossplot of pore space stiffness against frame stiffness factor (Figure 3.12) shows a very good correlation with reflection coefficient of 0.96. Rocks with intercrystalline, fine moldic and micro-porosity generally cluster at the lower left corner of the trend. Rocks with highly rigid framework and low permeabilities make up the higher right hand corner of the general trend. In Figure 3.12 we can also notice how highly cemented, low porosity rocks fall out of the general trendline. This could aid in discriminating the densely cemented, indurated rocks in carbonates with little to no permeabilities.

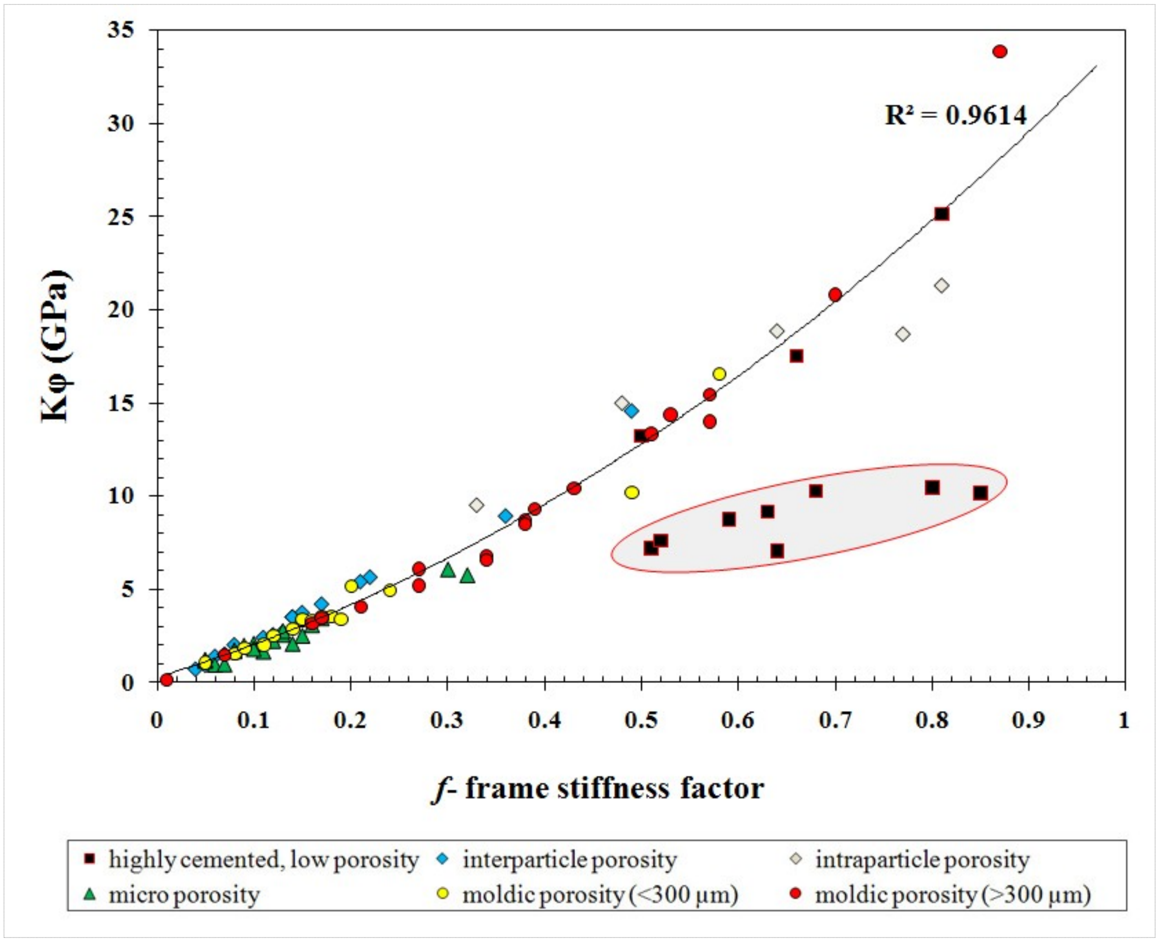

**Figure 3.12** Pore space stiffness versus frame stiffness factor. Notice how densely cemented, low porosity rocks fall out of the general trendline.

## 3.5 Conclusion

This section had a major focus on pore size and pore type effect on velocity with implication of carbonate rock physics models. With the application of Sun (2000, 2004) and Pore Stiffness models on Bahamian carbonate samples, we have come to meaningful results which fit well with our qualitative-pore structure observations.

The simplified carbonate rock-physics velocity model developed by Sun (2000) provides a key elastic parameter called “frame flexibility factors” which quantifies the effect of pore structure on elastic properties of carbonates. Our study shows that for core samples at a given porosity, the lower the frame flexibility factors the higher the sonic wave velocities. Frame flexibility factors less than 4 are generally either rocks with visible moldic pores or intraframe porosity, and samples with frame flexibility factors greater than 4 are sucrosic dolomites with dominant intercrystalline porosity, micro-porosity or densely cemented, low porosity rocks. Hence, for a given porosity generally higher gamma values relate to rocks with more grain contacts and coupling and lower gamma values relate to samples with rigid rock frames.

The $f$ parameter describing the stiffness and the rigidity of the rock frame under deformation shows that for core samples at a given porosity, the lower the frame stiffness factors the lower is the sonic wave velocities. , Hence lower $f$ (stiffness) and $f\mu$ (rigidity) values relate to rocks (micro- and intercrystalline porosity) which can deform easily under compressional and shear motion, whereas rocks with low frame stiffness factors (moldic, intraparticle porosity and highly cemented, low porosity) are in general insensitive to stress and show high elastic rigidity of the framework. Nevertheless, the frame stiffness factor against porosity diagram displays a larger scatter around best-fit curve, than frame rigidity factor. The large deviations are generally the product of variable elastic behavior of intraparticle and coarse moldic pores, which have self supporting framework with high elastic rigidity resulting in higher shear deformation and higher compressibilities.

The porosity independent physical parameter c (gamma ratio) has an average value of 0.86 for our samples. Gamma ratio that quantifies the shear deformation relative to compressibility shows general uniform relationship with Vp/Vs ratio, where large deviations from mean gamma value correspond to endmember sonic velocity ratios (either very high or very low).

Pore space stiffness model provides a non-linear porosity-bulk modulus relationship for carbonate pore types. Constant k ($K_{\varphi}/K_m$) values generate constant trend lines in the normalized bulk modulus-porosity diagram, providing a non-linear feeble relationship between pore space stiffness and specific pore types over wide range of porosities. Carbonate rocks having only micro-porosity, fine moldic porosity (<300µm) and interparticle/intercrystalline pores generally manifest lower normalized pore space stiffness values; whereas highly cemented, low porosity rocks show distinctive higher values of around 0.2.

Finding a relationship between pore compressibility and frame flexibility factors further delineated how porosity and pore geometries affect the mechanical response of a porous carbonate medium to compressional motion. The results imply that for a given porosity the pore space stiffness increases with decreasing frame flexibility factor.

Primary porosities (micro-porosity and interparticle/intercrystalline porosity) and fine moldic pores generally display low resistance to uniform compression, where rocks with coarse moldic and intraparticle porosities relate to low gamma and high pore stiffness values. Generally, samples, which fall between gamma values of 2 and 3 are all fast shallow water platform and reef deposits. The relationship of pore space stiffness with frame stiffness factor displays a general trend with reflection coefficient of 0.96. While rocks with intercrystalline, fine moldic and micro-porosity generally cluster at the lower left corner of the trendline, rocks with highly rigid framework and low permeabilities make up the higher right hand corner of the general trend. The crossplot of pore space stiffness with frame stiffness factor also aid in discriminating the densely cemented, indurated rocks in carbonates with little to no permeabilities.

# 4. THE EFFECTS OF PORE TYPES ON $CO_2$ FLUID SUBSTITUTION

## 4.1 Introduction

The previous two sections discussed the qualitative and quantitative interpretation of carbonate-specific pore types through their acoustic properties and rock physics models. The two techniques used for rock-physics analysis were Sun model (2000) and pore stiffness models (Baechle et al., 2006). The results imply that quantification of the pore geometries can be done based on the key elastic parameters, which are pure representations of the flexibility of the frame and connectivity of the pore space.

In this section, we perform a brief analysis of Gassmann's model in carbonates. The computation results indicate that carbonate samples do seem to suffer changes that are detectable in velocities and elastic properties. Gassmann's equation for fluid substitution is used for time-lapse seismic monitoring, which is an important part of any seismic attribute analysis, as it provides pilot computations for various fluid scenarios before the actual flooding process. Fluid replacement modeling is a procedure whereby the in-situ properties of a reservoir are replaced with alternate values from which seismic parameters such as compressional and shear wave velocities and density can be computed (Russell and Smith, 2007).

For this study we initially validate Gassmann's theory in carbonates and its assumptions. Following, we theoretically saturate the initially water saturated carbonate samples selected from GBB with oil. Then, we simulate the flooding of the same samples with $CO_2$ both in liquid and gas phase. GBB carbonate samples offer a great opportunity for this study, particularly due to their high porosities. As high porosities increase the volume of fluid in the rock, the large seismic responses and dry-frame compressibilities allow us to better sense the pore fluid. Bahamian samples consist of different pore types, porosities and permeabilities; nevertheless we must be careful in generalizing our results to all carbonates, as our samples are from a modern carbonate province with generally extremely high porosities.

## 4.2 Method

We use a time-lapse seismic monitoring technique to investigate the changes in carbonate rock properties induced by $CO_2$ and the effect of endmember carbonate pore types on the elastic properties of the saturated rock. Seismic monitoring of $CO_2$ saturated rocks provides a quantitative estimation of elastic properties for different pore types before and after the fluid substitution.

All GBB laboratory measurements were done on water saturated miniplug sampes (2.5 or 3.8cm in diameters) at different effective pressures. Initially, all carbonates are theoretically saturated with oil and the density, compressibility, and the rigidity of both oil and the rock are then computed. Later on, carbonates are saturated with the new fluid, which in this case is $CO_2$ in liquid and gas phase and the new densities and elastic moduli of rocks are computed thereafter.

The generally accepted method of doing the fluid replacement modeling is with modified Biot-Gassmann equations (Gassmann, 1951; Biot, 1956):

$$\frac{1}{C_{sat}-C_m}=\frac{1}{C_{dry}-C_m}+\frac{1}{C_{fl}-C_m}\frac{1}{\varphi} \tag{4-1}$$

where $C_{sat}$ is the compressibility of rock saturated with fluid, $C_{dry}$ is the compressibility of the dry tock frame, $C_m$ is the compressibility of the mineral matrix, $C_{fl}$ is the compressibility of the pore fluid, φ is the porosity of the rock.

There are many alternate forms of the Biot-Gassmann equation besides this one, but we find this form to be the easiest to work with when performing the fluid substitution modeling. Biot-Gassmann estimates the saturated compressibility ($C_{sat}$) through the compressibility of the matrix material ($C_s$), of the dry rock frame ($C_{dry}$), of the fluid ($C_{fl}$), and the rock porosity (φ). The compressibility of the rock is the inverse of the rock bulk modulus (stiffness) at a constant pore pressure. Equation (4-1) is used to simulate the fluid mixture into the pore space and obtain the final effective elastic properties for the saturated rock.

Despite the widespread use of this equation in fluid substitution scenarios, the applicability of Gassmann's equation in carbonates is still not well understood. Part of it is due to the violation of many assumptions for porous system that Gassmann's derivation is based on. One of the major assumptions behind this equation is shear modulus being independent of the pore fluid content:

$$\mu_{sat}=\mu_{dry} \tag{4-2}$$

where, μ is shear modulus of the rock. The major reasoning behind this is that fluids have a shear modulus of zero, so we expect the shear modulus of dry and fluid saturated rocks to remain unaltered. However, the grain contacts in carbonates can stiffen or weaken with fluid changes in the pore system, where shear modulus actually does change with saturation (Baechle et al., 2005; Adam et al., 2006). Thus, shear modulus in $CO_2$ saturated rocks should be well thought out before the calibration of Gassmann's equation for carbonates.

Later assumption indicates that the pore fluid has no chemical influence to the solid frame. Nevertheless, it is obvious that the injection of $CO_2$ will induce some physicochemical processes resulting in alterations within the rock frame. The pore-scale changes can either be pore-openings of some originally closed thin pores or fractures or increase the bulk density of the rock (Lumley et al., 2008; Vanorio et al., 2010). Subsequent assumption includes the porous frame being monomineralic. Considering that our pure carbonates have little variations in mineralogy, it will have little influence on our fluid substitution model. However, carbonates commonly have wider variety of textures and have relatively unstable mineralogy than clastic rocks. Other assumptions include the pores being in flow communication with each other and the pore pressure being in equilibrium between pores, which can be achieved at very low frequencies. Thus turning to the practical aspect of the matter, Gassmann's fluid substitution scheme might underpredict the time-lapse changes induced by fluid substitution (Vanorio et al., 2010). Despite all these assumptions behind Biot-Gassmann theory, beautify of equation (4.1) is its simplicity as well as the fact that the variables have physical meaning and can be directly measured.

Prior to delving into Gassmann substitution model, we must define the compressibility of the mineral matrix. Using the compositional lithology from core samples we can calculate the bulk modulus of the mineral matrix (inverse of the compressibility of the mineral matrix) via application of Voigt-Reuss–Hill (VRH) averaging of the mineral constituents. A VRH average is simply the average of the harmonic (Reuss average) and arithmetic (Voigt average) means of the mineral constituents (Smith et al., 2003). Carbonate samples from GBB are exclusively constituted of three endmember mineralogy of calcite, dolomite and aragonite. Hence, for a rock constituting of three minerals VRH average can be expressed as:

$$K_{Reuss} = \frac{F_1}{K_1} + \frac{F_2}{K_2} + \frac{F_3}{K_3} \tag{4-3}$$

$$K_{Voigt} = F_1 K_1 + F_2 K_2 + F_3 K_3 \tag{4-4}$$

$$K_{VRH} = \frac{1}{2}\ K_{Reuss} + K_{Voigt} \tag{4-5}$$

where $F_1$, $F_2$ and $F_3$ are volumetric fractions of three mineral components, and $K_1$, $K_2$ and $K_3$ are the bulk modulus of endmember calcite (76.8 GPa), dolomite (94.9 GPa) and aragonite (44.8 GPa).

The quality of our substitution model is also highly dependent on the accuracy of fluid parameters, especially the properties of $CO_2$ in liquid and gas phase. The $CO_2$ properties are estimated based on rock physics study of Wang et al. (1998) in McElroy field. In their study they used a $CO_2$ with purity >99.5% obtained from a commercial source, with critical temperature and pressure at 31 ºC (88 ºF) and 7.4 MPa (1070 psi) respectively (Wang et al., 1998). $CO_2$ behaves like a gas above the critical temperature, whereas below the critical temperature and above the critical pressure $CO_2$ will be in its liquid phase (Wang et al., 1998).

In general, the properties of $CO_2$ are dramatically different from properties of either water or oil (Wang and Nur, 1989). As seen from Figure 4.1, at higher injection pressures $CO_2$ density can reach the density of water, while its bulk modulus remains below that of water. The properties of $CO_2$ change rapidly between pore pressures of 1000 and 1500 psi. The gaseous phase of $CO_2$ occurs at pore pressures lower than 1000 psi, and it becomes liquid at pore pressures above 1000 psi. Compressional velocity of liquid $CO_2$ increases with increasing pore pressure, while the velocity of $CO_2$ gas phase decreases as pressure increases.

For our fluid substitution model nine core samples from both drillholes of Clino and Unda are selected. The first four samples have porosities between 39 and 41%, the later three have porosities between 33-35% and last two are lower porosity samples (23-24%), all of which are from different pore geometries with velocity measurements at 1000 and 2500 psi effective pressures (Table 4.1).

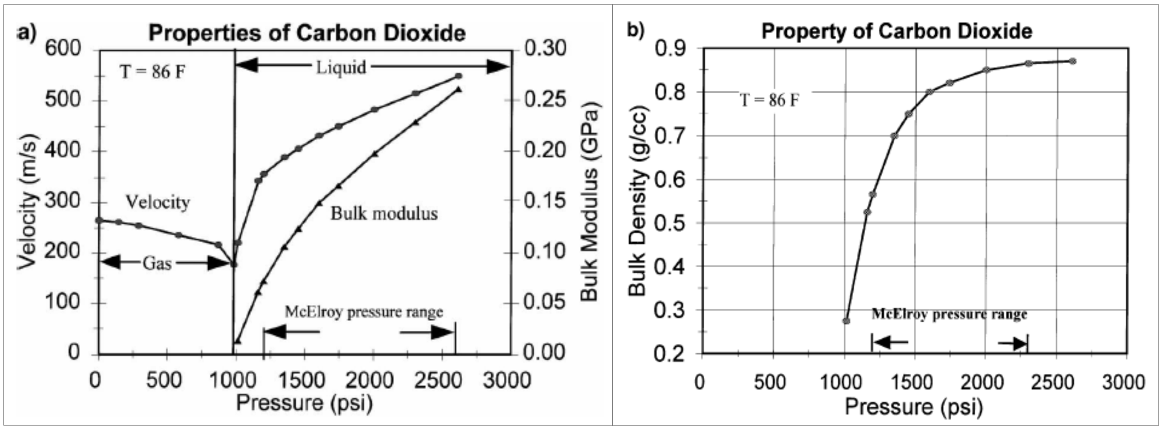

**Figure 4.1** Velocities (left y-axis), bulk moduli (right y-axis) (a), and bulk density (b) versus pressure in $CO_2$ at 86 ºF (30 ºC) (Wang et al., 1998).

**Table 4.1** Data table for nine core samples from GBB used in the substitution model.

| Sample | Porosity % | Pore type | Depositional environment | Vp (m/s) | Vs (m/s) | Vp (m/s) | Vs (m/s) |
|---|---|---|---|---|---|---|---|
| | | | | @1000psi | | @2500psi | |
| 17 | 39 | coarse moldic | platform | 5043 | 1930 | 5064 | 1948 |
| 18 | 41 | fine moldic | platform | 4392 | 1919 | 4376 | 1966 |
| 42 | 41 | interparticle | reef | 3192 | 1364 | 3330 | 1407 |
| 28 | 40 | micro-porosity | slope | 2368 | 983 | 2681 | 992 |
| 21 | 33 | coarse moldic | reef | 4110 | 2163 | 4135 | 2172 |
| 32 | 35 | micro-porosity | slope | 2983 | 1420 | 3112 | 1453 |
| 8 | 35 | intraparticle | reef | 4858 | 2580 | 4941 | 2588 |
| 2 | 23 | coarse moldic | platform | 4998 | 2601 | 5007 | 2612 |
| 49 | 24 | fine moldic | slope | 4641 | 2519 | 4058 | 2521 |

As seen from Figure 4.2 our selective samples for this study have completely different compressional and shear-wave velocities, even in rocks with the same porosity range. The pore types are representative of moldic, interparticle, intraparticle and micro-porosities. Figure 4.2 displays how frame flexibility factors also change with effective pressure. As indicated in Section 3, lower gamma values relate to better grain contacts with rigid rock frames. Hence, all velocity-pressure traces plotted in the graph (Figure 4.2) display in fact a systematic pattern of decreasing frame flexibility factors with increasing effective pressures due to better grain contacts and the closing of microcracks with increasing pressure (Table 4.2).

The compressional velocity against multiple effective pressure points (Figure 4.3) shows that apart from two lower porosity samples (2 and 49) all samples are pressure dependent. High porosity moldic rocks can reach maximum velocities during increasing pressures and suddenly begin to decrease above a critical pressure. This velocity decrease is due to continuous disintegration of the sample, destroying the partly cemented grain contacts that transmit the acoustic signal; however eventually velocity can increase again, because the newly formed fractures that reduce velocity in the first place are now being closed by the further increase in effective pressure (Anselmetti and Eberli, 2001). Slow samples of intercrystalline and micro-porosity show gentle increase in velocities with increasing pressure, as these samples are soft and unconsolidated.

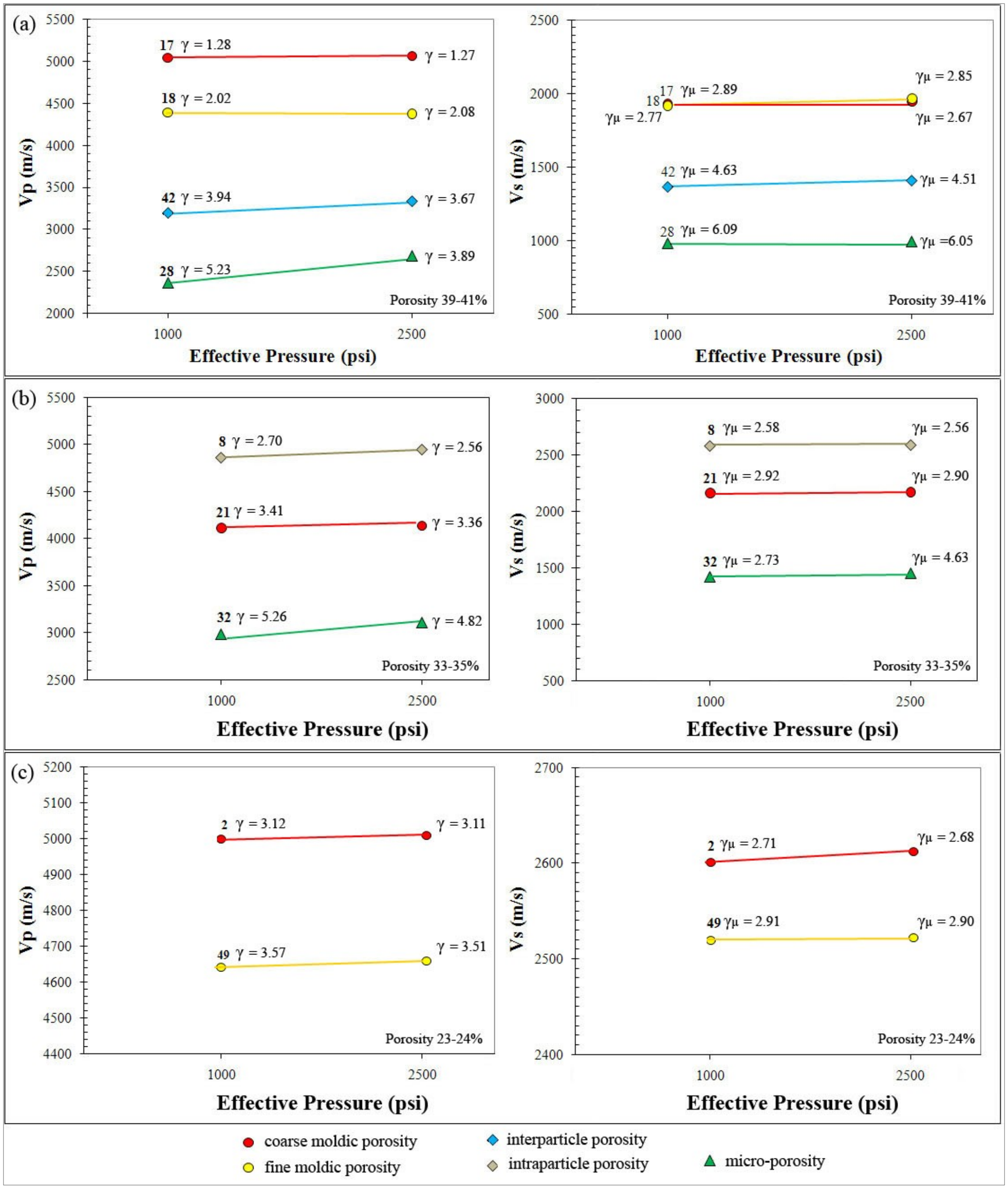

**Figure 4.2** Measured compressional and shear-wave velocities with respect to the frame flexibility factors at 1000 and 2500psi effective pressures. Porosities range as (a) 39-41%, (b) 33-35%, and (c) 23-24%.

**Table 4.2** Frame flexibility factors and gamma ratio for core samples used in the study of fluid substitution model.

| **Sample** | **φ %** | **Pore type** | **Depositional environment** | **γ** | **γμ** | **c** | **γ** | **γμ** | **c** |
|---|---|---|---|---|---|---|---|---|---|
| | | | | **@1000psi** | | | **@2500psi** | | |
| 17 | 39 | coarse moldic | Platform | 1.28 | 2.89 | 2.26 | 1.27 | 2.85 | 2.25 |
| 18 | 41 | fine moldic | Platform | 2.01 | 2.77 | 1.37 | 2.08 | 2.67 | 1.29 |
| 42 | 41 | interparticle | Reef | 3.94 | 4.63 | 1.18 | 3.67 | 4.51 | 1.23 |
| 28 | 40 | micro-porosity | Slope | 5.23 | 6.09 | 1.16 | 3.89 | 6.05 | 1.56 |
| 21 | 33 | coarse moldic | Reef | 3.41 | 2.92 | 0.86 | 3.36 | 2.90 | 0.86 |
| 32 | 35 | micro-porosity | Slope | 5.26 | 4.73 | 0.90 | 4.82 | 4.63 | 0.96 |
| 8 | 35 | intraparticle | Reef | 2.70 | 2.57 | 0.95 | 2.56 | 2.56 | 1.00 |
| 2 | 23 | coarse moldic | Platform | 3.11 | 2.71 | 0.87 | 3.11 | 2.68 | 0.86 |
| 49 | 24 | fine moldic | Slope | 3.57 | 2.91 | 0.82 | 3.51 | 2.90 | 0.83 |

In our substitution model pore pressure is subject to change for different fluid scenarios, while the effective pressure is kept constant (1000 psi and 2500 psi), as the pore pressure change is exactly balanced by an increase in confining pressure (Equation 4.6). Thus the controlling variable for velocity variation is effective pressure.

$$P_{eff} = P_c - P_{Pore} \tag{4-6}$$

where $P_{eff}$, $P_c$ and $P_{pore}$ are effective, confining and pore pressures respectively. The pore pressures for water saturated, oil saturated, $CO_2$ gas and liquid saturated rocks are taken at 300 psi, 500 psi, 1000 psi and 2000 psi respectively.

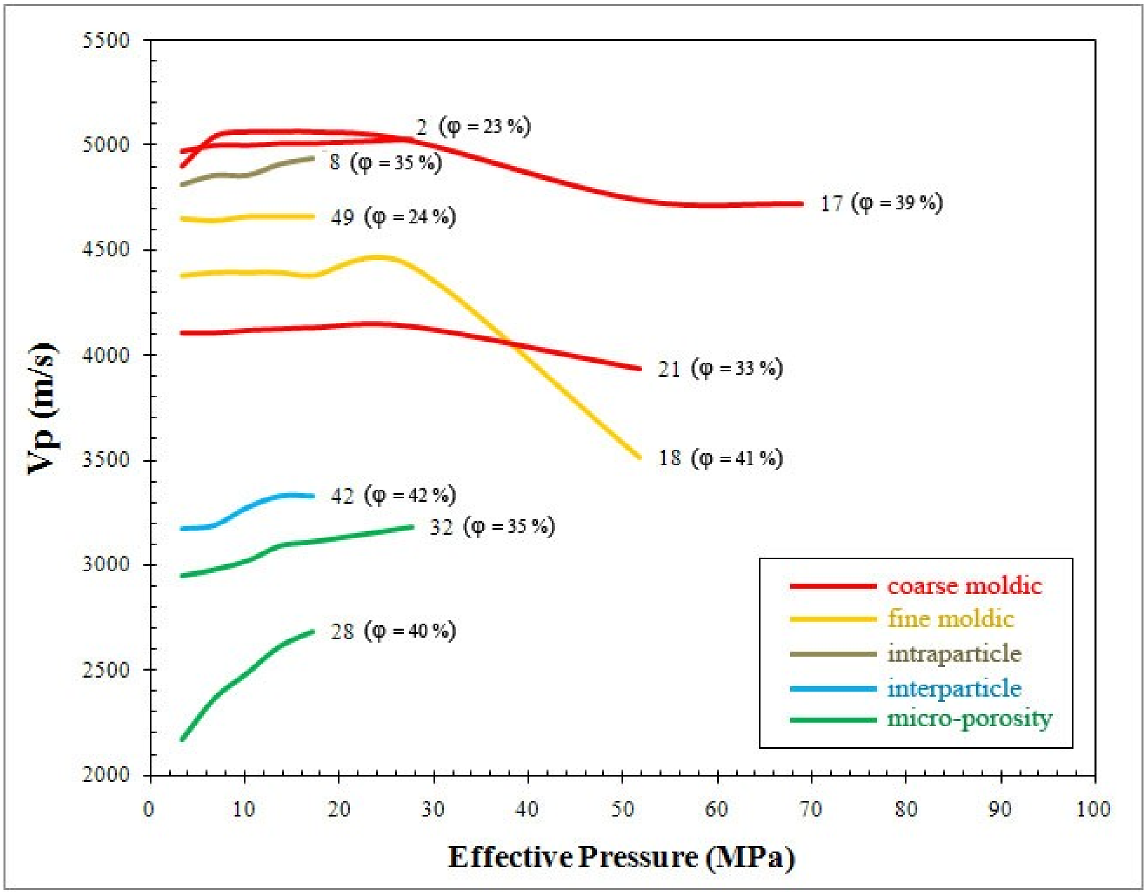

**Figure 4.3** Measured compressional velocities with different effective pressures, for core samples used in the study of the fluid substitution model.

## 4.3 Results

The simulated substitution of water-wet samples, with oil and later with $CO_2$ in gaseous and liquid phase results both in different compressibilities and velocities. Figure 4.4 displays the effect of fluid substitution on rock compressibilities for different fluid phase scenarios. $CO_2$ flooding decreases the bulk modulus for core samples used in this model at both effective pressure points (1000 psi and 2500 psi), the decrease being slightly more for $CO_2$ in gaseous phase (Tables 4.3 and 4.4).

The shear-wave velocities, however, increase with $CO_2$ substitution, as the density of each individual fluid phase decreases while shear modulus is kept constant (Figure 4.5). The increase in Vs for gas phase $CO_2$ saturation is much higher than for liquid $CO_2$. The reason behind this phenomenon is the change in rock densities being higher for $CO_2$ gas saturated rocks than for $CO_2$ liquid saturated samples (Tables 4.3 and 4.4). The amount of porosity is also important for density effect on velocity, as the grain-to-grain contacts are important factors for stiffening and weakening effects with fluid changes (Baechle et al., 2009). Therefore, higher porosities result in higher decrease in density and hence, in higher Vs. In concert, shear wave velocities is a function of $CO_2$ fluid phase (pore pressure), density and subsequently the total porosity.

The compressional-wave velocities show much unpredictable behavior than implied in compressibility and shear-wave velocities. As seen in Figure 4.6 all $CO_2$ liquid saturations (with pore pressures at 2000 psi) show a substantial decrease in Vp, whereas $CO_2$ gas saturation (with pore pressures at 1000 psi) can either decrease or increase depending on the pore types.

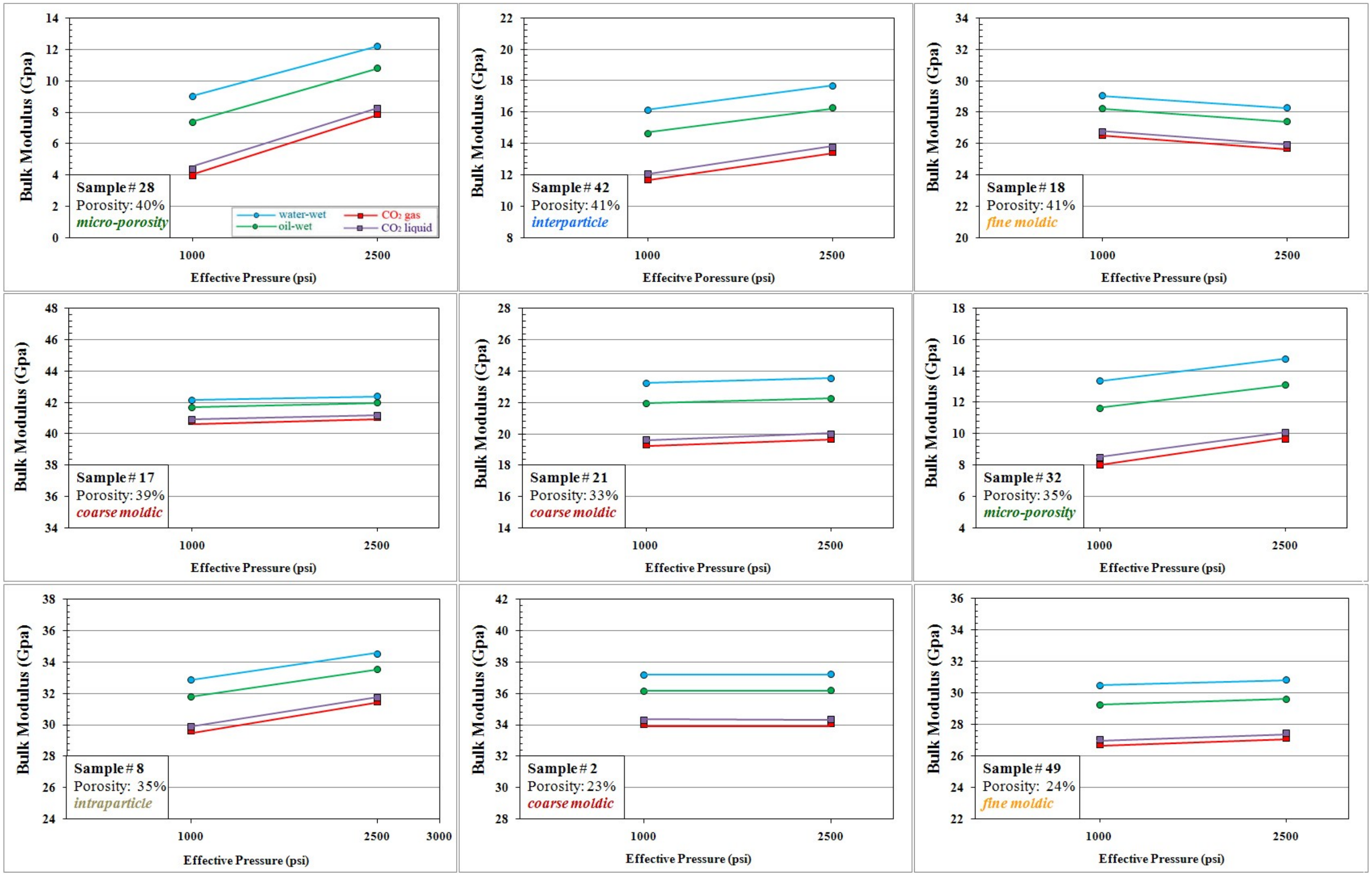

**Figure 4.4** Bulk modulus against effective pressure plot for different samples at different porosities. The samples are saturated with water, oil, $CO_2$ gas and $CO_2$ liquid respectively. The representative pore types are coarse moldic, fine moldic, interparticle, intraparticle and micro-porosities.

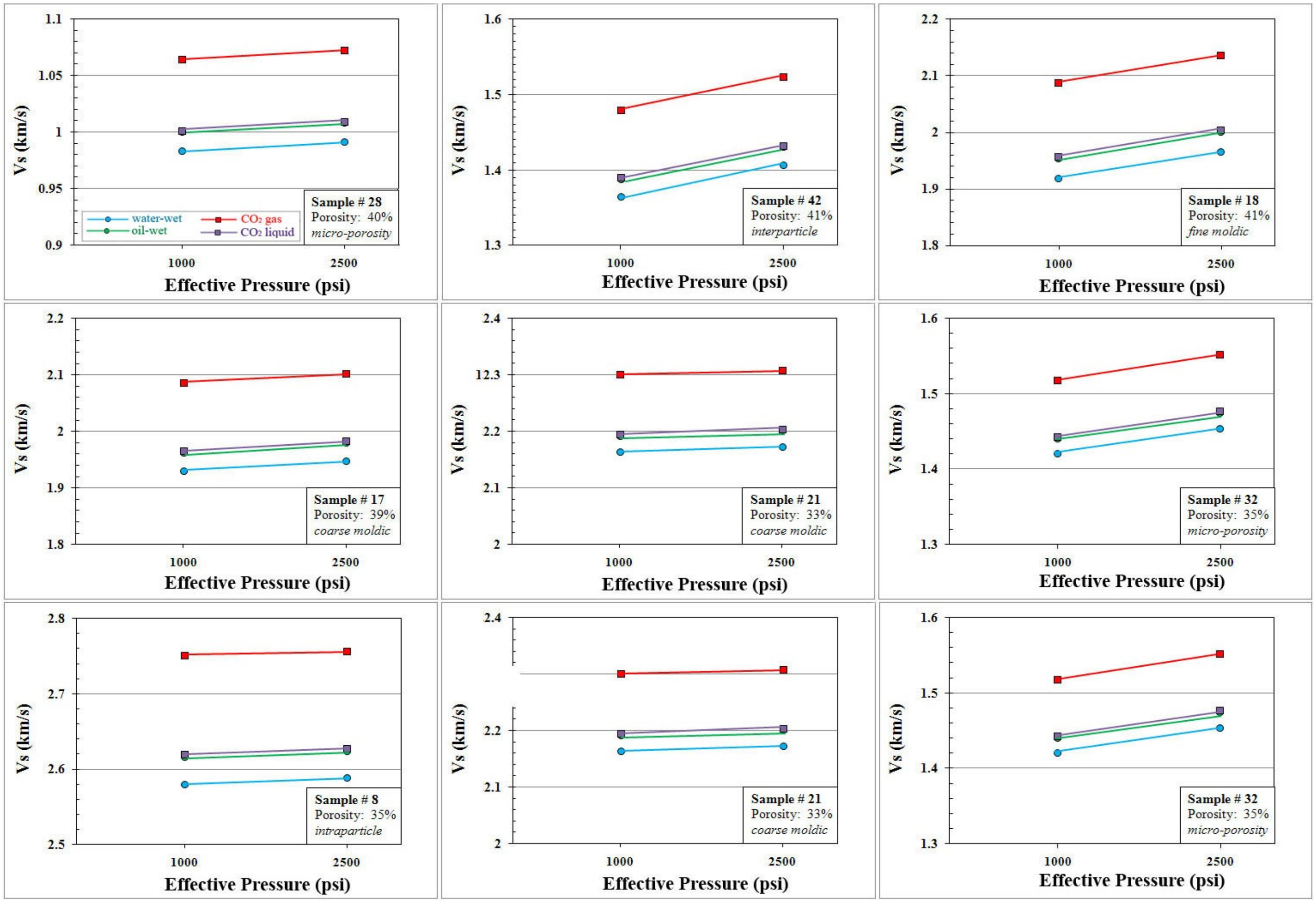

**Figure 4.5** Shear-wave velocities against effective pressure plot for different samples at different porosities. The samples are saturated with water, oil, $CO_2$ gas and $CO_2$ liquid respectively. The representative pore types are coarse moldic, fine moldic, interparticle, intraparticle and micro-porosities.

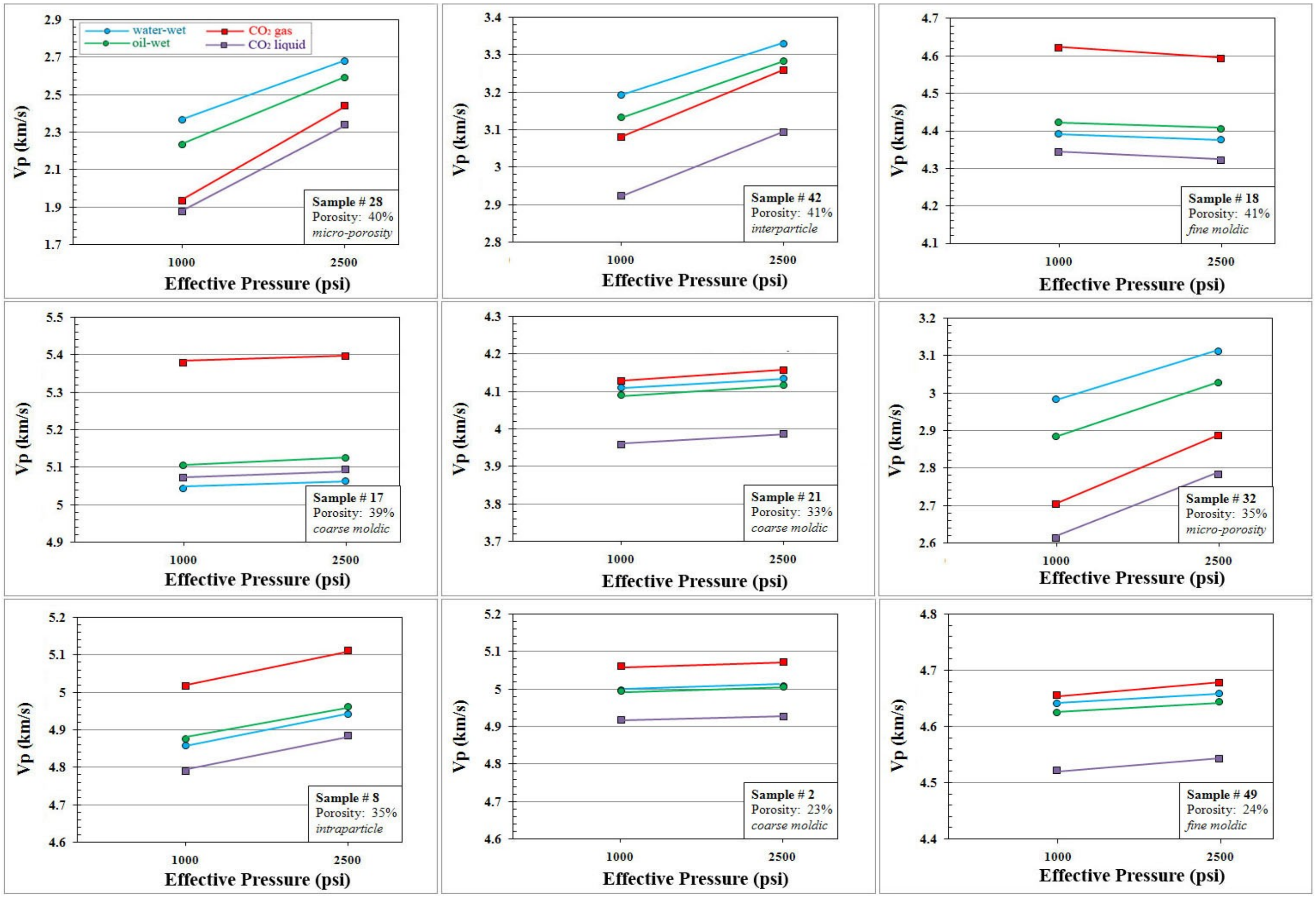

**Figure 4.6** Compressional-wave velocities against effective pressure plot for different samples at different porosities. The samples are saturated with water, oil, $CO_2$ gas and $CO_2$ liquid respectively. The representative pore types are coarse moldic, fine moldic, interparticle, intraparticle and micro-porosities.

Figure 4.6 implies that $CO_2$ gas saturated samples with moldic and intraparticle porosities (sample 18, 17, 21, 8, 2 and 49) show increase in compressional velocities; whereas micro-porosity and interparticle porosities (28, 42 and 32) show decrease in compressional velocities. For core samples that show decreasing compressional velocities with $CO_2$ gas saturation, the bulk modulus effect is much stronger than the density effect. It means that the decrease in bulk modulus after the $CO_2$ gas substitution is much higher than the decrease in rock densities (Tables 4.3 and 4.4). Therefore, the compressional velocities for those samples are markedly controlled by the profound effect of compressibility relative to density. On the contrary, the core samples saturated with $CO_2$ gas phase display an increase in P-wave velocity, which is a control of density effect, as the decrease in bulk modulus is substantially neglected in the equation (3.1).

As seen in Figure 4.6, $CO_2$ liquid saturated samples always show decrease in compressional velocities as the change in densities are very little which is a slight decrease (Table 4.3). This results in higher densities than implied in core samples saturated with $CO_2$ gas. Hence, in this fluid phase scenario, Vp values are being controlled by the bulk modulus effect rather than the density effect. Having said so, the much higher decreases in stiffness result in much more pronounced decrease in compressional velocities.

**Table 4.3** Effect of $CO_2$ substitution in liquid phase on Bulk Modulus (K) and density (ρ), grouped by effective pressures (calculated using the Gassmann equation).

| # | φ % | Pore type | K GPa | ρ g/cc | K % | ρ % | K GPa | ρ g/cc | K % | ρ % |
|---|---|---|---|---|---|---|---|---|---|---|
| | | | $P_{eff}$ @1000 psi | | | | $P_{eff}$ @2500 psi | | | |
| 17 | 39 | c. moldic | 40.90 | 1.99 | -1.91 | -0.25 | 41.17 | 1.99 | -1.87 | -0.25 |
| 18 | 41 | f. moldic | 26.74 | 1.94 | -5.19 | -0.27 | 25.89 | 1.94 | -5.52 | -0.27 |
| 42 | 41 | interparticle | 12.04 | 2.01 | -17.71 | -0.26 | 13.77 | 2.01 | -15.29 | -0.26 |
| 28 | 40 | micro | 4.39 | 2.01 | -40.19 | -0.26 | 8.24 | 2.01 | -23.61 | -0.26 |
| 21 | 33 | c. moldic | 19.61 | 2.12 | -10.56 | -0.20 | 19.99 | 2.12 | -10.26 | -0.20 |
| 32 | 35 | micro | 8.45 | 2.08 | -27.12 | -0.22 | 10.09 | 2.08 | -22.91 | -0.22 |
| 8 | 35 | intraparticle | 29.87 | 2.16 | -5.94 | -0.21 | 31.73 | 2.16 | -5.32 | -0.21 |
| 2 | 23 | c. moldic | 34.29 | 2.29 | -5.13 | -0.13 | 34.34 | 2.29 | -5.11 | -0.13 |
| 49 | 24 | f. moldic | 27.03 | 2.29 | -7.57 | -0.14 | 27.42 | 2.29 | -7.36 | -0.14 |

**Table 4.4** Effect of $CO_2$ substitution in gaseous phase on Bulk Modulus (K) and density (ρ), grouped by effective pressures (calculated using the Gassmann equation).

| # | φ % | Pore type | K GPa | ρ g/cc | K % | ρ % | K GPa | ρ g/cc | K % | ρ % |
|---|---|---|---|---|---|---|---|---|---|---|
| | | | $P_{eff}$ @1000 psi | | | | $P_{eff}$ @2500 psi | | | |
| 17 | 39 | c. moldic | 40.79 | 1.75 | -2.17 | -12.00 | 41.07 | 1.75 | -2.12 | -12.00 |
| 18 | 41 | f. moldic | 26.55 | 1.70 | -5.89 | -12.89 | 25.69 | 1.70 | -6.27 | -12.89 |
| 42 | 41 | interparticle | 11.69 | 1.77 | -20.13 | -12.45 | 13.43 | 1.77 | -17.38 | -12.45 |
| 28 | 40 | micro | 3.98 | 1.77 | -45.76 | -12.19 | 7.89 | 1.77 | -26.87 | -12.19 |
| 21 | 33 | c. moldic | 19.29 | 1.92 | -12.02 | -9.53 | 19.68 | 1.92 | -11.67 | -9.53 |
| 32 | 35 | micro | 8.02 | 1.87 | -30.86 | -10.27 | 9.68 | 1.87 | -26.07 | -10.27 |
| 8 | 35 | intraparticle | 29.62 | 1.95 | -6.75 | -9.89 | 31.48 | 1.95 | -6.04 | -9.89 |
| 2 | 23 | c. moldic | 34.04 | 2.15 | -5.83 | -6.16 | 34.08 | 2.15 | -5.81 | -6.16 |
| 49 | 24 | f. moldic | 26.72 | 2.14 | -8.62 | -6.43 | 27.11 | 2.14 | -8.38 | -6.43 |

The effects of $CO_2$ saturation on the velocities are calculated by:

$$Effect\ of\ flooding = \frac{CO_2 flooded\ velocity - Oil\ saturated\ velocity}{Oil\ saturated\ velocity}\ 100\% \qquad (4\text{-}7)$$

As mentioned before the $CO_2$ liquid flooding decreases the compressional velocities at all effective pressures due to a much pronounced effect of bulk modulus (Figure 4.7). The Vp decrease ranges from 0.6 to 16%, with the extend of the decrease being a strong function of pore types (Table 4.5). Samples 42, 32 and 28 with intercrystalline and micro-porosity show more decrease in Vp after being flooded with $CO_2$ in the liquid phase, while the decrease in Vp in samples with intraparticle and moldic pores is relatively small (<3.5%). The shear wave velocities after $CO_2$ liquid substitution always increase; Vs change increases with increasing porosities.

As seen in Figure 4.8, the compressional velocities after gaseous-phase $CO_2$ sequestration decrease for samples with interparticle and micro-porosity (28, 42 and 32). On the contrary, Vp increases for samples with moldic and intraparticle porosity (18, 17, 21, 82, 49). The Vp increase is a function of porosity for rocks saturated with $CO_2$ gas saturant. As mentioned before porosity is important for density effect on velocities; hence, Vp change for rocks with increasing compressional velocities is higher for high porosities and lower for low porosities (Table 4.6). The shear wave velocities after $CO_2$ gas substitution always increase, with that the increase being higher for high porosities.

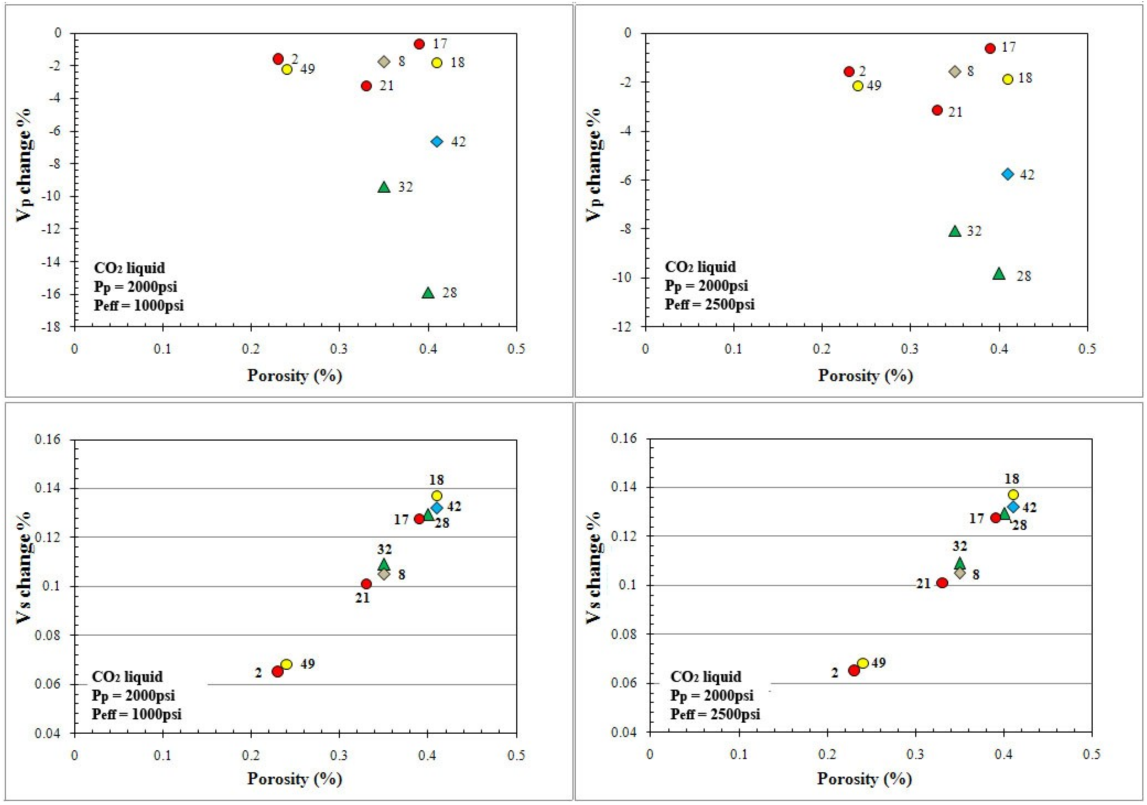

**Figure 4.7** Effects of *$CO_2$ liquid* flooding on Vp and Vs at different net effective pressures ($P_{eff}$). Each data point is labeled with the sample number.

**Table 4.5** Effect of $CO_2$ substitution in liquid phase on velocities, grouped by effective pressures (calculated using the Gassmann equation).

| # | φ % | Pore type | Vp m/s | Vs m/s | Vp % | Vs % | Vp m/s | Vs m/s | Vp % | Vs % |
|---|---|---|---|---|---|---|---|---|---|---|
| | | | $P_{eff}$ @1000 psi | | | | $P_{eff}$ @2500 psi | | | |
| 17 | 39 | c. moldic | 5072 | 1965 | -0.6 | 0.127 | 5095 | 1982 | -0.6 | 0.127 |
| 18 | 41 | f. moldic | 4343 | 1956 | -1.8 | 0.137 | 4322 | 2004 | -1.9 | 0.137 |
| 42 | 41 | interparticle | 2925 | 1390 | -6.6 | 0.132 | 3094 | 1432 | -5.8 | 0.132 |
| 28 | 40 | micro | 1878 | 1001 | -15.9 | 0.130 | 2338 | 1009 | -9.8 | 0.130 |
| 21 | 33 | c. moldic | 3959 | 2194 | -3.2 | 0.101 | 3988 | 2203 | -3.1 | 0.101 |
| 32 | 35 | micro | 2612 | 1442 | -9.4 | 0.109 | 2783 | 1476 | -8.1 | 0.109 |
| 8 | 35 | intraparticle | 4790 | 2619 | -1.7 | 0.105 | 4884 | 2627 | -1.6 | 0.105 |
| 2 | 23 | c. moldic | 4918 | 2625 | -1.6 | 0.065 | 4927 | 2636 | -1.6 | 0.065 |
| 49 | 24 | f. moldic | 4522 | 2543 | -2.2 | 0.068 | 4543 | 2546 | -2.2 | 0.068 |

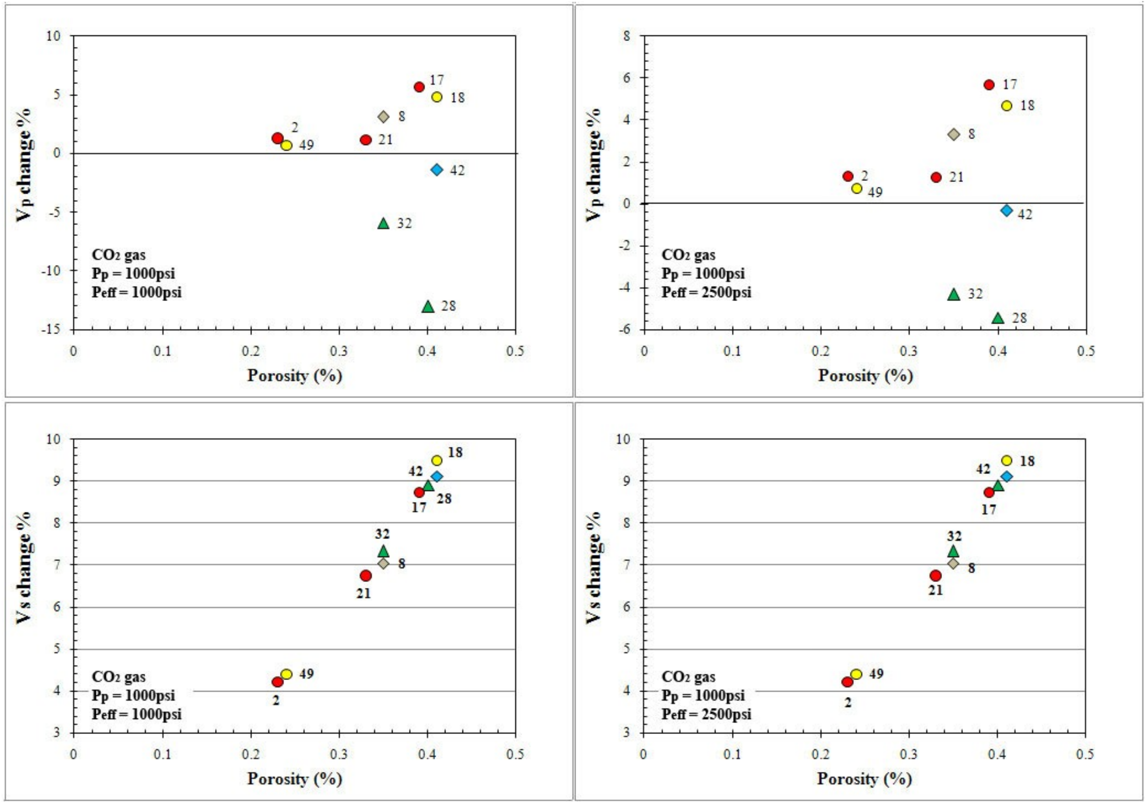

**Figure 4.8** Effects of *$CO_2$ gas* flooding on Vp and Vs at different net effective pressures ($P_{eff}$). Each data point is labeled with the sample number.

**Table 4.6** Effect of $CO_2$ substitution in gaseous phase on velocities, grouped by effective pressure (calculated using the Gassmann equation).

| # | φ % | Pore type | Vp m/s | Vs m/s | Vp % | Vs % | Vp m/s | Vs m/s | Vp % | Vs % |
|---|---|---|---|---|---|---|---|---|---|---|
| | | | $P_{eff}$ @1000 psi | | | | $P_{eff}$ @2500 psi | | | |
| 17 | 39 | c. moldic | 5394 | 2134 | 5.7 | 8.74 | 5418 | 2153 | 5.7 | 8.74 |
| 18 | 41 | f. moldic | 4634 | 2139 | 4.8 | 9.49 | 4611 | 2191 | 4.7 | 9.49 |
| 42 | 41 | interparticle | 3090 | 1514 | -1.4 | 9.11 | 3273 | 1561 | -0.3 | 9.11 |
| 28 | 40 | micro | 1943 | 1089 | -13 | 8.90 | 2452 | 1098 | -5.4 | 8.90 |
| 21 | 33 | c. moldic | 4138 | 2340 | 1.2 | 6.75 | 4169 | 2350 | 1.3 | 6.75 |
| 32 | 35 | micro | 2713 | 1546 | -5.9 | 7.33 | 2897 | 1582 | -4.3 | 7.33 |
| 8 | 35 | intraparticle | 5027 | 2800 | 3.1 | 7.04 | 5128 | 2808 | 3.3 | 7.04 |
| 2 | 23 | c. moldic | 5061 | 2734 | 1.3 | 4.21 | 5072 | 2746 | 1.3 | 4.21 |
| 49 | 24 | f. moldic | 4657 | 2654 | 0.7 | 4.41 | 4678 | 2657 | 0.7 | 4.41 |

## 4.4 Conclusion

This section delivers the computational results for $CO_2$ fluid substitution model in carbonates and performs a brief analysis for Gassmann's equation. The results demonstrate that carbonate samples seem to suffer changes due to the fluid substitution, detectable with sound waves and elastic moduli. The effect of $CO_2$ flooding on seismic properties of the rock depends on many factors, such as the compressibility contrast between the pore fluids before and after the substitution, the pore structure of the reservoir rock, the injection pressure and the reservoir pressure buildup and formation temperature (Wang et al., 1998).

In order to simulate different fluid substitution scenarios by contemplating 4 saturation conditions: (1) 100% brine (the in-situ fluid), (2) oil, (3) $CO_2$ gas, and (4) $CO_2$ liquid. This substitution model uses both $CO_2$ liquid and gas phase in order to separate pore pressure effect from $CO_2$ effect in carbonate pore types. The effective and pore fluid pressures are changed during each substitution cycle. As $CO_2$ liquid at 2000 psi pore pressure displaces oil in the rock it decreases the bulk modulus with little change in the bulk density of the reservoir rock. As a result, the Vp decreases, the change in velocity ranging from -0.6% to -16%. The shear wave velocities in rocks saturated with $CO_2$ liquid phase always increase (0.6% to 14%), while the change in Vs decreasing with decreasing porosity.

For gas phase $CO_2$ saturation, P-wave velocities display variable results depending on the carbonate pore types. In this fluid phase scenario, Vp displays significant decrease for samples with interparticle and micro-porosity rocks while increasing for samples with moldic and intraparticle porosity. The shear wave velocities after $CO_2$ gas substitution always increase with change being higher for high porosity rocks.

Even though in theory Gassmann's equation predicts that Vs essentially increases with $CO_2$ flooding, previous studies in laboratory measurements (Wang et al., 1998) have shown that Vs, in fact, decreases by approximately 1%. The shear-wave velocity prediction by Gassmann's theory is only controlled by the density contrast of the pore fluids before and after the substitution, as in theory shear modulus stays unaffected with saturation. However, the grain contacts in carbonates can stiffen or weaken with fluid changes in the pore system, where shear modulus actually does change with saturation. Furthermore, it is important to reckon the $CO_2$ induced physicochemical processes resulting in alterations within the rock frame. This will contribute in porosity changes, in which case, $\varphi$ parameter in Gassmann's equation will not be taken constant before and after the substitution. Thus, Gassmann's equation should be calibrated prior to using in any $CO_2$ fluid substitution computations in carbonates in order to avoid the assumptions of a constant porosity and shear modulus.

# 5. MAIN CONCLUSIONS AND RECOMMENDATIONS

This research reveals theoretical results of a quantitative study intended to evaluate the potential changes in carbonate acoustic and elastic properties after $CO_2$ sequestration. The dataset used in the study were core samples from two drillholes (Clino and Unda) drilled at the western margin of Great Bahama Bank. The Bahamian carbonates range from unconsolidated mud to lithified carbonates, exhibiting a wide range of pore types, rock textures and depositional environments, which provide an excellent flexibility for this study.

We observe that the rock age, mineralogy and origin had minor influence on velocity distributions in Bahamian carbonates. Even though these rocks exhibit limited mineralogy, the sonic velocities, however, show remarkably wide range of values. The main factors controlling these velocity variations are depositional environments, porosity and carbonate-specific pore types.

The depositional environments can have a direct influence on velocity distributions, where shallow water deposits generally show higher velocities compared to deeper water carbonates. This is due to the higher content of metastable minerals and coarse grain sizes in shallow platform and reef deposits. As the amount of metastable minerals (Aragonite and High-Mg Calcite) of non-skeletal origin, parallel with available pore space for fluid flow increase, they further stimulate the diagenetic processes. The velocity evolutions of GBB carbonates reveal that a sample passing through several diagenetic stages result in many different pore categories through its burial history, making the pore and pore-throat system more complex, thus yielding a wider range of velocity distributions.

Although, the porosity demonstrates a general trend with velocity, the characteristic influence of different pore types on elastic properties can further explain why rocks with the same porosity can have very different velocities. The results show that interparticle and micro-porosity rocks, which are generally not embedded in a rigid rock frame, result in lower velocities than certain moldic and intraframe porosities, which are considered as frame-forming pore types.

Porosity and permeability are two critical parameters that significantly affect estimates of reservoir properties. However, making such estimates in carbonates can especially be challenging. Therefore, an effective rock-physics model capable of quantifying the different pore types is required to effectively characterize the Bahamian carbonate rocks properties. By using a simplified carbonate rock-physics velocity model, previously introduced by Sun (2000), we are able to consider all governing factors important for carbonate reservoir characterization. The elastic parameters used in the model and referred to as frame flexibility factors offer a structural representation of the media. Since the frame flexibility factors are independent of porosity, they vary with other parameters such as geometry of porous media, the amount of fine grains, grain compaction and grain coupling. As a result, higher frame flexibility values relate to rocks with more grain contacts and coupling, while lower values associate with highly rigid rock frame. The gamma ratio ($c=\gamma_\mu/\gamma$), which is the other very important parameter introduced in the model, can also relate to acoustic behavior of rocks. The geometrical average of gamma ratio, approximated either from core plugs or even at the well location from logs in the studied field could be used to estimate the $\gamma_\mu$, or the pseudo-shear wave velocity (Vs) from sonic logs where the shear log data is not available, as previously explained by Sun (2004).

The stiffness ($f$) and rigidity ($f_\mu$) factors also serve as good quantitative indicators of pore types and reservoir rock properties. That being said, the lower $f/f_\mu$ values are generally associated with micro- and intercrystalline porosities, which deform easily under compressional and shear motion. On the contrary, moldic, intraparticle and highly cemented rocks, commonly insensitive to stress, show higher values of frame stiffness/rigidity factors.

We found that, the combined method of Sun and Pore Space Stiffness models may suggest a further enhancement in our carbonate reservoir characterization. The results reveal that for a given porosity the pore space stiffness increases with decreasing frame flexibility factors, which can aid in discriminating the poor carbonates of low permeabilities from highly permeable rocks.

In this thesis, we reveal our theoretical results through a brief analysis via Gassmann's model for available carbonate pore types. We demonstrate that all samples with endmember carbonate specific pore types seem to experience changes that are detectable on our velocities and elastic parameters. The results from our fluid substitution model suggest that the changes in density, compressibility and seismic properties of the rock are mostly governed by, both the pressure conditions and the carbonate pore types. A comparison between samples in the liquid and gaseous $CO_2$

saturated state showed significant variations. We observe that the ultrasonic $V_p$ velocities show a marked decrease in the order of 0.6 to 16% with liquid-phase $CO_2$ immersion. The shear wave velocities in rocks saturated with $CO_2$ liquid phase always increase (0.6% to 14%), and the change in Vs decreases with decreasing porosity.

For the gaseous-phase $CO_2$ state, $V_p$ shows a marked increase for samples with moldic and intraframe porosities, and decrease for samples with intercrystalline and micro-porosities. For the moldic and intraframe samples, the decrease in bulk modulus with immersion in $CO_2$ gas is much less than the decrease in bulk density. Hence, the Vp is controlled somewhat by the density effect, as the decrease in bulk modulus is substantially neglected in the Gassmann's equation. For intercrystalline and micro-porosity sample, the decrease in bulk modulus is much higher than bulk density, therefore, the compressional velocities for these samples evidently are controlled by the profound effect of compressibility relative to density. The $V_s$ velocities, on the other hand, always show an increase in values associated with the density change of $CO_2$ phases, and are mainly a function of porosity.

Geological sequestration of $CO_2$ has never been an easy task for the oil industry. Depending on the depth of storage, pore pressure and temperature $CO_2$ will behave in various phases. It may exist in the pore space of the subsurface rock both as in gaseous or liquid phase. Hence, the seismic monitoring of $CO_2$ sequestration at depth is highly dependent on the $CO_2$ as a pore fluid, where its elastic properties can vary significantly across the pressure and temperature ranges. Hence, the detailed knowledge of the $CO_2$

properties need to be known in order to effectively model the elastic properties of rocks saturated in $CO_2$.

It is important to acknowledge all the assumptions by Gassmann's equation that is in violation with carbonates. Hence, certain errors may be present in our results. Firstly, it needs to be taken into consideration that $CO_2$ is not an inert fluid, so it can react with the rock matrix to alter or dissolve the rock frame leading to secondary porosities. Secondly, turning to the practical aspect of the matter there is a substantial violation in Gassmann's assumption of a constant shear modulus, especially in carbonate rocks. The grain contacts in carbonates can stiffen or weaken with fluid changes in the pore system, where shear modulus actually does change with saturation. Both the non-constant porosity with time and non-constant shear modulus reflect an inconsistency with Gassmann's model. Thus, Gassmann's fluid substitution scheme might underpredict the time-lapse changes induced by $CO_2$ substitution. Hence, further experimental studies need to be conducted to confirm with our theoretical results.

Nevertheless, this work provides significant results that could be a guide for future researches on time-lapse seismic monitoring of carbonates following $CO_2$ injection at depth. As preliminary results, these findings look promising. To conclude with, this research represents a theoretical attempt that will assist future researchers in better understanding the effect of rock types on seismic monitoring of $CO_2$ sequestration in carbonates.

# REFERENCES

Adam, L., M. Batzle, and I. Brevik, 2006, Gassmann's fluid substitution and shear modulus variability in carbonates at laboratory seismic and ultrasonic frequencies: Geophysics, **71**, 173–183.

Ahr, W.M., 2008, Geology of Carbonate Reservoirs: John Wiley & Sons, New York.

Anselmetti, F.S., 1994, Physical Properties and Seismic Response of Carbonate Sediments and Rocks: Ph.D. dissertation, Eidgenössische Technische Hochschule Zürich.

Anselmetti, F.S. and G.P. Eberli, 1993, Controls on sonic velocity in carbonates: Pure and Applied Geophysics, **141**, 287-323.

Anselmetti, F.S. and G.P. Eberli, 2001, Sonic velocity in carbonates–a combined product of depositional lithology and diagenetic alterations, *in* R.N. Ginsburg, eds., Subsurface Geology of a Prograding Carbonate Platform Margin, Great Bahama Bank: Results of the Bahamas Drilling Project, Tulsa, OK, 191-216.

Anselmetti, F.S., S.M. Luthi, and G.P. Eberli, 1998, Quantitative characterization of carbonate pore systems by digital image analysis: AAPG Bulletin, **82**, 1815-1836.

Baechle, G. T., R. J. Weger, G. P. Eberli, J. L. Massaferro, and Y.F. Sun, 2005, Changes of shear moduli in carbonates rocks: implications for Gassmann applicability: The Leading Edge, **24**, 507–510.

Baechle, G.T., R.J Weger, G.P. Eberli, and A. Colpaert, 26th-28th, April, 2006, Bergen, Norway, Pore size and pore type effects on velocity - Implication for carbonate rock physic model: The Sound of Geology Workshop.

Baechle, G.T., G.P. Eberli, R.J. Weger, and J.L. Massaferro, 2009, Changes in dynamic shear moduli of carbonate rocks with fluid substitution: Geophysics, **74**, E135-E147.

Batzle, M. and Z. Wang, 1992, Seismic properties of pore fluids: Geophysics, **57**, 1396-1408.

Biot, M.A., 1956, Theory of propagation of elastic waves in a fluid-saturated porous solid. I. low-frequency range: The Journal of the Acoustical Society of America, **28**, 168-178.

Blatt, H., G. Middleton, and R. Murray, 1980, Origin of Sedimentary Rocks: Prentice Hall, Inc., Englewood Cliffs, N. J.

Choquette, P.W. and L.C. Pray, 1970, Geologic nomenclature and classification of porosity in sedimentary carbonates: AAPG Bulletin, **54**, 207-250.

Dou, Q. and Y.F. Sun, 2008, Rock-physics-based Heterogeneity Characterization of a Carbonate Reservoir in Permian Basin: 79th Annual International Meeting, SEG.

Eberli, G.P., G.T. Baechle, F.S. Anselmetti, and M.L. Incze, 2003, Factors controlling elastic properties in carbonate sediments and rocks: The Leading Edge, **22**, 654-660.

Gardner, G.H.F., L.W. Gardner, and A.R. Gregory, 1974, Formation velocity and density: The diagnostic basics for stratigraphic traps: Geophysics, **39**, 770-780.

Gartner, G.L.B., J. Massaferro, M.R. Nasser, J. Leguijt, K.V.d. Kolk, H. Hillgartner, W. Asyee, G.P. Eberli, R. Weger, and Y.F. Sun, 3rd-5th, December, 2008, Kuala Lumpur, Malaysia, Obtaining Permeability From Seismic Data-A New Breakthrough in Carbonate Reservoir Modeling: International Petroleum Technology Conference.

Gassmann, F., 1951, Elastic waves through a packing of spheres: Geophysics, **16**, 673-685.

Ginsburg, R.N., 2001, The Bahamas Drilling Project: Backgroung and Acquisition of Cores and Logs, *in* R.N. Ginsburg, eds., Subsurface Geology of a Prograding Carbonate Platform Margin, Great Bahama Bank: Results of the Bahamas Drilling Project, Tulsa, OK, 3-13.

Hamilton, E.L., 1980, Geoacoustic modeling of the sea floor: The Journal of the Acoustical Society of America, **68**, 1313-1340.

Hamilton, E.L., G. Shumway, H.W. Menard, and C.J. Shipek, 1956, Acoustic and other physical properties of shallow-water sediments off San Diego: The Journal of the Acoustical Society of America, **28**, 1.

Japsen, P., 1993, Influence of lithology and neogene uplift on seismic velocities in Denmark: Implications for depth conversion of maps AAPG Bulletin **77**, 194-211.

Kenter, J.A.M., R.N. Ginsburg, and S.R. Troelstra, 2001, Sea-Level-Driven Sedimentation Patterns on the Slope and Margin, *in* R.N. Ginsburg, eds., Subsurface Geology of a Prograding Carbonate Platform Margin, Great Bahama Bank: Results of the Bahamas Drilling Project, Tulsa, OK, 61-100.

Kumar, M. and D.-h. Han, 2005, Pore shape effect on elastic properties of carbonate rocks: SEG Expanded Abstracts, **24**, 1477-1480.

Lumley, D., 2010, 4D seismic monitoring of $CO_2$ sequestration: The Leading Edge, **29**, 150-155.

Lumley, D., D. Adams, R. Wright, D. Markus, and S. Cole, 2008, Seismic monitoring of $CO_2$ geo-sequestration: realistic capabilities and limitations: SEG Expanded Abstracts, **27**, 2841-2845.

Marion, D., A. Nur, H. Yin, and D. Han, 1992, Compressional velocity and porosity in sand-clay mixtures: Geophysics, **57**, 554-563.

Massaferro, J.L., F.S. Anselmetti, G.P. Eberli, G.T. Baechle, G.B. Gartner, and Y.F. Sun, 2002, Effects on pore types on velocity and permeability in carbonates: Shell International Exploration and Production B.V., 37-39.

Massaferro, J.L., G.P. Eberli, G.T. Baechle, R. Weger, and Y.F. Sun, 2004, Effects on pore types on velocity and permeability in carbonate rocks: Applications of sun model to core-log-seismic inversion: Final game changer report: Shell International Exploration and Production B.V.,

Mavko, G. and T. Mukerji, 1995, Seismic pore space compressibility and Gassmann's relation: Geophysics, **60**, 1743-1749.

Melim, L.A., P.K. Swart, and R.G. Maliva, 2001, Meteoric and marine-burial diagenesis in the subsurface of Great Bahama Bank, *in* R.N. Ginsburg, eds., Subsurface Geology of a Prograding Carbonate Platform Margin, Great Bahama Bank: Results of the Bahamas Drilling Project, Tulsa, OK, 137-161.

Murphy, W., A. Reischer, and K. Hsu, 1993, Modulus decomposition of compressional and shear velocities in sand bodies: Geophysics, **58**, 227-239.

Pickett, G.R., 1963, Acoustic character logs and their applications in formation evaluation Transactions of the Society of Petroleum Engineers of Aime, **228**, 659-667.

Rafavich, F., C.H.S.C. Kendall, and T.P. Todd, 1984, The relationship between acoustic properties and the petrographic character of carbonate rocks: Geophysics, **49**, 1622-1636.

Raymer, L.L., E.R. Hunt, and J.S. Gardner, 1980, An improved sonic transit time-to-porosity transform: Society of Professional Well Log Analysts.

Russell, B.H., K. Hedlin, F.J. Hilterman, and L.R. Lines, 2003, Fluid-property discrimination with AVO: A Biot-Gassmann perspective: Geophysics, **68**, 29-39.

Russell, B.H. and T. Smith, 2007, The relationship between dry rock bulk modulus and porosity–An empirical study: CREWES Research Report, **19**,

Sayers, C.M., 2008, The elastic properties of carbonates: The Leading Edge, **27**, 1020-1024.

Schlanger, S.O. and R.G. Douglas, 1974, The pelagic ooze-chalk-limestone transition and its implications for marine stratigraphy, *in* K.J. Hsu and H.C. Jenkins, eds., Pelagic sediments on land and under the sea: Special Publication International Association of Sedimentologists, John Wiley & Sons, New York, 117-148.

Schlumberger, 2007, Carbonate Reservoirs, http://www.slb.com/~/media/Files/industry_challenges/carbonates/brochures/cb_carbonate_reservoirs_07os003.ashx, accessed 3 September 2010.

Siggins, A.F., 2006, Velocity-effective stress response of CO2-saturated sandstones: Exploration Geophysics, **37**, 60-66.

Smith, T.M., C.H. Sondergeld, and C.S. Rai, 2003, Gassmann fluid substitutions: A tutorial: Geophysics, **68**, 430-440.

Sun, Y.F., 1994, On the Foundations of the Dynamical Theory of Fractured Porous Media and the Gravity Variations Caused by Dilatancies: Ph.D. dissertation, Columbia University.

Sun, Y.F., 2000, Core-log-seismic integration in hemipelagic marine sediments on the eastern flank of the Juan de Fuca Ridge: Ocean Drilling Program, Scientific results, **168**, 21-35.

Sun, Y.F., 2004, Seismic signatures of rock pore structure: Applied Geophysics, **1**, 42-49.

Vanorio, T., G. Mavko, S. Vialle, and K. Spratt, 2010, The rock physics basis for 4D seismic monitoring of $CO_2$ fate: Are we there yet?: The Leading Edge, **29**, 156-162.

Vernik, L. and A. Nur, 1992, Petrophysical classification of siliciclastics for lithology and porosity prediction from seismic velocities: AAPG Bulletin, **76**, 1295-1309.

Wang, Z., M.E. Cates, and R.T. Langan, 1998, Seismic monitoring of a $CO_2$ flood in a carbonate reservoir: A rock physics study: Geophysics, **63**, 1604-1617.

Wang, Z.J., W.K. Hirsche, and G. Sedgwick, 1991, Seismic velocities in carbonate rocks: Journal of Canadian Petroleum Technology, **30**, 112-122.

Wang, Z. and A. Nur, 1990, Dispersion analysis of acoustic velocities in rocks: The Journal of the Acoustical Society of America, **87**, 2384-2395.

Wang, Z. and A.M. Nur, 1989, Effects of $CO_2$ flooding on wave velocities in rocks with hydrocarbons: SPE Reservoir Engineering, **4**, 429-436.

Weger, R.J., G.P. Eberli, G.T. Baechle, J.L. Massaferro, and Y.-F. Sun, 2009, Quantification of pore structure and its effect on sonic velocity and permeability in carbonates: AAPG Bulletin, **93**, 1297-1317.

Wyllie, M.R.J., A.R. Gregory, and G.H.F. Gardner, 1958, An experimental investigation of factors affecting elastic wave velocities in porous media: Geophysics, **23**, 459-493.

Xu, S. and M.A. Payne, 2009, Modeling elastic properties in carbonate rocks: The Leading Edge, **28**, 66-74.

Xue, Z. and T. Ohsumi, 2004, Seismic wave monitoring of $CO_2$ migration in water-saturated porous sandstone: Exploration Geophysics, **35**, 25-32.

# APPENDIX A

The dataset from measured plugs of core samples of two drillholes (Clino and Unda) from Great Bahama Bank (Anselmetti and Eberli, 1993). The displayed acoustic properties are measured at a confining and pore fluid pressures of 10 MPa and 2 MPa, respectively (effective pressure = 8 MPa). Depths are in meters below mudpit (mbmp).

| Well | Sample | Depth | Original type of | Pore types | wet bulk | K | φ | LMC | Dolomite | Aragonite | Vp | Vs |
|---|---|---|---|---|---|---|---|---|---|---|---|---|
| | Number | mbmp | sediments | | density g/cc | mD | % | % | | | (m/s) @ | 8 Mpa |
| CLINO | 19 | 104.0 | *Halimeda*-packstone | highly cemented, low porosity | 2.47 | | 14 | 100 | 0 | 0 | 5818 | 2930 |
| CLINO | 24 | 211.4 | wackestone | | 2.55 | <0.01 | 9 | 95 | 0 | 5 | 5454 | 2887 |
| CLINO | 62 | 219.7 | skeletal wackestone to packstone | | 2.60 | | 7 | 73 | 6 | 21 | 5394 | 2918 |
| CLINO | 26 | 256.1 | skeletal packstone, redalgaes | | 2.54 | 0.01 | 10 | 98 | 0 | 2 | 5350 | 2836 |
| UNDA | 7 | 292.9 | skeletal grainstone | | 2.61 | 0.8 | 14 | 0 | 100 | 0 | 5953 | 3187 |
| UNDA | 10 | 344.9 | skeletal grainstone | | 2.73 | < 0.01 | 6 | 0 | 100 | 0 | 6350 | 3490 |
| CLINO | 63 | 351.1 | skeletal grainstone | | 2.68 | | 9 | 7 | 93 | 0 | 5661 | 3158 |
| UNDA | 92 | 351.7 | skeletal grainstone | | 2.46 | | 22 | 8 | 92 | 0 | 5314 | 2968 |
| CLINO | 29 | 355.1 | skeletal to peloidal grainstone | | 2.68 | <0.01 | 4 | 86 | 11 | 3 | 6045 | 3150 |
| UNDA | 12 | 357.5 | skeletal grainstone | | 2.68 | < 0.01 | 3 | 91 | 1 | 8 | 6031 | 3118 |
| CLINO | 30 | 367.8 | no original grains preserved | | 2.62 | <0.01 | 10 | 46 | 54 | 0 | 5478 | 3025 |
| UNDA | 80 | 112.4 | skeletal (?) grainstone | interparticle and intercrystalline porosity | 2.03 | | 44 | 25 | 75 | 0 | 3168 | 1632 |
| UNDA | 78 | 118.5 | peloidal pack to grainstone | | 1.79 | | 56 | 56 | 20 | 24 | 2433 | 1467 |
| UNDA | 38 | 135.0 | skeletal paleoidal grainstone | | 1.90 | | 49 | 85 | 10 | 5 | 2568 | 1100 |
| UNDA | 85 | 262.3 | peloidal to skeletal packstone | | 1.99 | | 45 | 65 | 35 | 0 | 2629 | 1222 |
| UNDA | 41 | 269.4 | only few echinoderms preseved | | 1.99 | 678 | 47 | 1 | 97 | 0 | 2501 | 1328 |
| UNDA | 86 | 271.0 | only few echinoderms preseved | | 2.08 | | 42 | 9 | 91 | 0 | 3481 | 1803 |
| UNDA | 5 | 279.5 | skeletal packstone | | 1.96 | | 46 | 44 | 56 | 0 | 2403 | 1113 |
| UNDA | 6 | 285.9 | nothing preserved | | 1.96 | | 49 | 0 | 100 | 0 | 2697 | 1052 |
| UNDA | 84 | 288.2 | miliolids and echinoderms | | 2.00 | | 46 | 42 | 58 | 0 | 1907 | 1138 |
| UNDA | 89 | 307.3 | only few echinoderms preseved | | 2.12 | | 41 | 1 | 99 | 0 | 3176 | 1738 |
| UNDA | 42 | 309.8 | no original grains preserved | | 2.09 | 571 | 41 | 1 | 97 | 2 | 3192 | 1364 |
| UNDA | 43 | 316.1 | only few algaes preseved | | 2.35 | | 27 | 1 | 97 | 2 | 4567 | 2511 |
| UNDA | 9 | 321.9 | only few algaes preseved | | 2.02 | | 46 | 0 | 100 | 0 | 2405 | 991 |
| UNDA | 88 | 332.9 | few skeletal grains preserved | | 2.06 | | 44 | 0 | 100 | 0 | 3001 | 1536 |
| UNDA | 44 | 337.0 | only few red algaes preserved | | 2.25 | | 32 | 15 | 85 | 0 | 4928 | 2632 |
| UNDA | 13 | 377.5 | skeletal packstone | | 1.97 | 137 | 45 | 72 | 24 | 4 | 2267 | 1072 |
| CLINO | 67 | 552.3 | *Globigerina* wackestone | | 2.03 | | 42 | 65 | 35 | 0 | 2700 | 1234 |
| CLINO | 46 | 26.3 | coral | intraparticle porosity | 2.26 | | 29 | 36 | 0 | 64 | 4722 | 2414 |
| CLINO | 58 | 55.6 | coral | | 2.19 | | 31 | 100 | 0 | 0 | 4917 | 2380 |
| CLINO | 47 | 111.5 | coral | | 2.52 | 63 | 11 | 99 | 1 | 0 | 5855 | 3053 |
| UNDA | 87 | 302.4 | coral | | 2.08 | | 43 | 0 | 100 | 0 | 4015 | 2066 |
| UNDA | 8 | 303.0 | coral, encrusting red algea | | 2.23 | | 35 | 0 | 100 | 0 | 4858 | 2580 |
| UNDA | 81 | 137.7 | peloidal to skeletal packstone (?) | micro-porosity | 2.02 | | 41 | 91 | 6 | 3 | 3046 | 1546 |
| UNDA | 83 | 141.5 | peloidal to skeletal packstone (?) | | 2.22 | | 30 | 87 | 6 | 7 | 3905 | 2102 |
| UNDA | 82 | 200.0 | skeletal to peloidal packstone | | 1.89 | | 50 | 73 | 27 | 0 | 2544 | 1266 |
| CLINO | 25 | 236.2 | *Globigerina* packstone | | 1.91 | | 49 | 59 | 1 | 40 | 2503 | 1095 |
| CLINO | 27 | 291.3 | wackestone with few globigerinas | | 1.97 | 0.9 | 47 | 40 | 1 | 58 | 2219 | 1076 |
| CLINO | 50 | 317.9 | mudstone | | 1.85 | | 53 | 45 | 0 | 55 | 2365 | 1048 |
| CLINO | 28 | 330.6 | *Globigerina* wackestone | | 2.08 | | 40 | 44 | 1 | 55 | 2368 | 983 |
| UNDA | 90 | 354.1 | skeletal packstone to wackestone | | 2.02 | | 46 | 0 | 100 | 0 | 2415 | 1250 |
| UNDA | 91 | 357.9 | muddy wackestone | | 1.95 | | 47 | 26 | 6 | 68 | 2299 | 1182 |
| CLINO | 32 | 510.5 | *Globigerina*-echinoderm packstone | | 2.15 | 31 | 35 | 87 | 10 | 3 | 2983 | 1420 |
| CLINO | 69 | 528.2 | *Globigerina* packstone | | 1.98 | | 43 | 96 | 4 | 0 | 2618 | 1104 |
| CLINO | 68 | 535.3 | *Globigerina* (blackened) packstone | | 2.02 | | 41 | 94 | 6 | 0 | 2791 | 1306 |
| CLINO | 33 | 535.9 | *Globigerina*-echinoderm packstone | | 1.99 | 153 | 44 | 90 | 10 | 0 | 2409 | 1055 |
| CLINO | 53 | 548.0 | laminated *Globigerina* packstone | | 1.84 | | 53 | 72 | 28 | 0 | 2156 | 924 |
| CLINO | 34 | 605.3 | *Globigerina* wackestone | | 1.94 | 131 | 47 | 79 | 18 | 3 | 2402 | 1079 |
| CLINO | 35 | 623.6 | wackestone with *Globigerinas* | | 2.05 | 39 | 41 | 82 | 15 | 3 | 2602 | 1205 |
| CLINO | 70 | 624.8 | coarse *Globigerina* packstone | | 2.05 | | 40 | 83 | 17 | 0 | 2541 | 1180 |
| CLINO | 71 | 656.8 | laminated wackestone-packstone | | 2.37 | | 22 | 89 | 11 | 0 | 4373 | 2502 |
| CLINO | 74 | 665.6 | laminated *Globigerina* packstone | | 2.37 | | 40 | 78 | 1 | 21 | 2424 | 1080 |
| CLINO | 73 | 675.7 | *Globigerina* packstone | | 2.37 | | 44 | 82 | 2 | 16 | 2478 | 1356 |

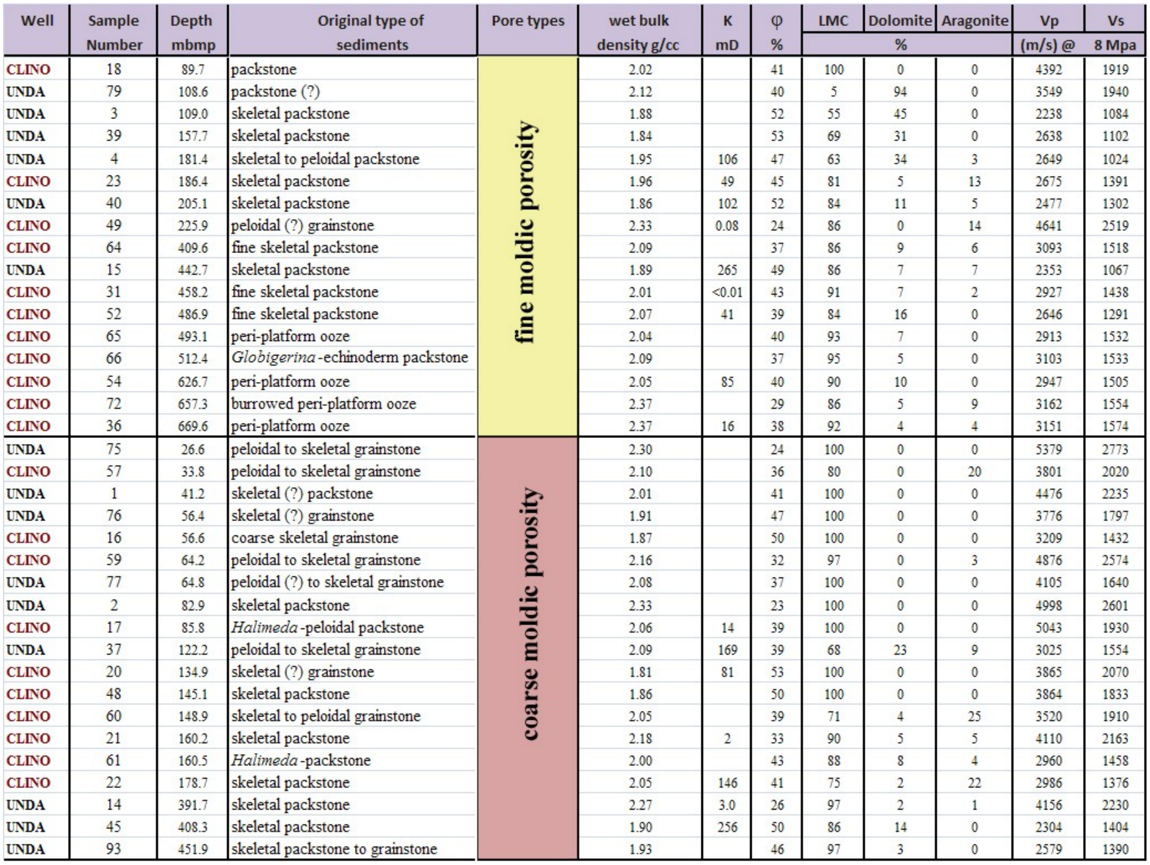

| Well | Sample | Depth | Original type of | Pore types | wet bulk | K | φ | LMC | Dolomite | Aragonite | Vp | Vs |
|---|---|---|---|---|---|---|---|---|---|---|---|---|
| | Number | mbmp | sediments | | density g/cc | mD | % | % | | | (m/s) @ | 8 Mpa |
| **CLINO** | 18 | 89.7 | packstone | **fine moldic porosity** | 2.02 | | 41 | 100 | 0 | 0 | 4392 | 1919 |
| **UNDA** | 79 | 108.6 | packstone (?) | | 2.12 | | 40 | 5 | 94 | 0 | 3549 | 1940 |
| **UNDA** | 3 | 109.0 | skeletal packstone | | 1.88 | | 52 | 55 | 45 | 0 | 2238 | 1084 |
| **UNDA** | 39 | 157.7 | skeletal packstone | | 1.84 | | 53 | 69 | 31 | 0 | 2638 | 1102 |
| **UNDA** | 4 | 181.4 | skeletal to peloidal packstone | | 1.95 | 106 | 47 | 63 | 34 | 3 | 2649 | 1024 |
| **CLINO** | 23 | 186.4 | skeletal packstone | | 1.96 | 49 | 45 | 81 | 5 | 13 | 2675 | 1391 |
| **UNDA** | 40 | 205.1 | skeletal packstone | | 1.86 | 102 | 52 | 84 | 11 | 5 | 2477 | 1302 |
| **CLINO** | 49 | 225.9 | peloidal (?) grainstone | | 2.33 | 0.08 | 24 | 86 | 0 | 14 | 4641 | 2519 |
| **CLINO** | 64 | 409.6 | fine skeletal packstone | | 2.09 | | 37 | 86 | 9 | 6 | 3093 | 1518 |
| **UNDA** | 15 | 442.7 | skeletal packstone | | 1.89 | 265 | 49 | 86 | 7 | 7 | 2353 | 1067 |
| **CLINO** | 31 | 458.2 | fine skeletal packstone | | 2.01 | <0.01 | 43 | 91 | 7 | 2 | 2927 | 1438 |
| **CLINO** | 52 | 486.9 | fine skeletal packstone | | 2.07 | 41 | 39 | 84 | 16 | 0 | 2646 | 1291 |
| **CLINO** | 65 | 493.1 | peri-platform ooze | | 2.04 | | 40 | 93 | 7 | 0 | 2913 | 1532 |
| **CLINO** | 66 | 512.4 | *Globigerina* -echinoderm packstone | | 2.09 | | 37 | 95 | 5 | 0 | 3103 | 1533 |
| **CLINO** | 54 | 626.7 | peri-platform ooze | | 2.05 | 85 | 40 | 90 | 10 | 0 | 2947 | 1505 |
| **CLINO** | 72 | 657.3 | burrowed peri-platform ooze | | 2.37 | | 29 | 86 | 5 | 9 | 3162 | 1554 |
| **CLINO** | 36 | 669.6 | peri-platform ooze | | 2.37 | 16 | 38 | 92 | 4 | 4 | 3151 | 1574 |
| **UNDA** | 75 | 26.6 | peloidal to skeletal grainstone | **coarse moldic porosity** | 2.30 | | 24 | 100 | 0 | 0 | 5379 | 2773 |
| **CLINO** | 57 | 33.8 | peloidal to skeletal grainstone | | 2.10 | | 36 | 80 | 0 | 20 | 3801 | 2020 |
| **UNDA** | 1 | 41.2 | skeletal (?) packstone | | 2.01 | | 41 | 100 | 0 | 0 | 4476 | 2235 |
| **UNDA** | 76 | 56.4 | skeletal (?) grainstone | | 1.91 | | 47 | 100 | 0 | 0 | 3776 | 1797 |
| **CLINO** | 16 | 56.6 | coarse skeletal grainstone | | 1.87 | | 50 | 100 | 0 | 0 | 3209 | 1432 |
| **CLINO** | 59 | 64.2 | peloidal to skeletal grainstone | | 2.16 | | 32 | 97 | 0 | 3 | 4876 | 2574 |
| **UNDA** | 77 | 64.8 | peloidal (?) to skeletal grainstone | | 2.08 | | 37 | 100 | 0 | 0 | 4105 | 1640 |
| **UNDA** | 2 | 82.9 | skeletal packstone | | 2.33 | | 23 | 100 | 0 | 0 | 4998 | 2601 |
| **CLINO** | 17 | 85.8 | *Halimeda* -peloidal packstone | | 2.06 | 14 | 39 | 100 | 0 | 0 | 5043 | 1930 |
| **UNDA** | 37 | 122.2 | peloidal to skeletal grainstone | | 2.09 | 169 | 39 | 68 | 23 | 9 | 3025 | 1554 |
| **CLINO** | 20 | 134.9 | skeletal (?) grainstone | | 1.81 | 81 | 53 | 100 | 0 | 0 | 3865 | 2070 |
| **CLINO** | 48 | 145.1 | skeletal packstone | | 1.86 | | 50 | 100 | 0 | 0 | 3864 | 1833 |
| **CLINO** | 60 | 148.9 | skeletal to peloidal grainstone | | 2.05 | | 39 | 71 | 4 | 25 | 3520 | 1910 |
| **CLINO** | 21 | 160.2 | skeletal packstone | | 2.18 | 2 | 33 | 90 | 5 | 5 | 4110 | 2163 |
| **CLINO** | 61 | 160.5 | *Halimeda* -packstone | | 2.00 | | 43 | 88 | 8 | 4 | 2960 | 1458 |
| **CLINO** | 22 | 178.7 | skeletal packstone | | 2.05 | 146 | 41 | 75 | 2 | 22 | 2986 | 1376 |
| **UNDA** | 14 | 391.7 | skeletal packstone | | 2.27 | 3.0 | 26 | 97 | 2 | 1 | 4156 | 2230 |
| **UNDA** | 45 | 408.3 | skeletal packstone | | 1.90 | 256 | 50 | 86 | 14 | 0 | 2304 | 1404 |
| **UNDA** | 93 | 451.9 | skeletal packstone to grainstone | | 1.93 | | 46 | 97 | 3 | 0 | 2579 | 1390 |

# APPENDIX B

Frame Flexibility factors and gamma ratio values calculated from Sun (2000) model for all 89 carbonate samples from GBB.

| Well | Sample Number | Depth mbmp | Pore types | γ | γμ | c | Kφ |
|---|---|---|---|---|---|---|---|
| CLINO | 19 | 104.0 | highly cemented, low porosity | 2.36 | 2.73 | 1.157 | 25.133 |
| CLINO | 24 | 211.4 | | 5.83 | 4.44 | 0.762 | 9.17 |
| CLINO | 62 | 219.7 | | 7.21 | 5.92 | 0.821 | 7.062 |
| CLINO | 26 | 256.1 | | 5.93 | 4.3 | 0.725 | 8.743 |
| UNDA | 7 | 292.9 | | 3.74 | 3.51 | 0.939 | 17.544 |
| UNDA | 10 | 344.9 | | 7.13 | 4.89 | 0.686 | 10.272 |
| CLINO | 63 | 351.1 | | 8.2 | 5.27 | 0.643 | 7.208 |
| UNDA | 92 | 351.7 | | 3.77 | 2.83 | 0.751 | 13.226 |
| CLINO | 29 | 355.1 | | 6.35 | 5.61 | 0.883 | 10.449 |
| UNDA | 12 | 357.5 | | 6.45 | 7.37 | 1.143 | 10.167 |
| CLINO | 30 | 367.8 | | 7.18 | 4.49 | 0.625 | 7.61 |
| UNDA | 80 | 112.4 | interparticle and intercrystalline porosity | 4.04 | 3.51 | 0.869 | 4.213 |
| UNDA | 78 | 118.5 | | 4.89 | 2.72 | 0.556 | 0.723 |
| UNDA | 38 | 135.0 | | 4 | 3.98 | 0.995 | 2.71 |
| UNDA | 85 | 262.3 | | 4.68 | 4.18 | 0.893 | 2.42 |
| UNDA | 41 | 269.4 | | 5.49 | 4.01 | 0.730 | 1.409 |
| UNDA | 86 | 271.0 | | 3.8 | 3.42 | 0.900 | 5.661 |
| UNDA | 5 | 279.5 | | 5.35 | 4.49 | 0.839 | 1.526 |
| UNDA | 6 | 285.9 | | 3.85 | 4.5 | 1.169 | 3.759 |
| UNDA | 89 | 307.3 | | 4.71 | 3.69 | 0.783 | 3.526 |
| UNDA | 42 | 309.8 | | 3.95 | 4.63 | 1.172 | 5.417 |
| UNDA | 43 | 316.1 | | 4.25 | 3.51 | 0.826 | 8.948 |
| UNDA | 9 | 321.9 | | 5.05 | 5.07 | 1.004 | 2.028 |
| UNDA | 88 | 332.9 | | 4.41 | 3.84 | 0.871 | 3.518 |
| UNDA | 44 | 337.0 | | 2.86 | 2.62 | 0.916 | 14.584 |
| UNDA | 13 | 377.5 | | 6.13 | 4.58 | 0.747 | 0.932 |
| CLINO | 67 | 552.3 | | 4.91 | 4.51 | 0.919 | 2.571 |
| CLINO | 46 | 26.3 | intraparticle porosity | 1.62 | 2.95 | 1.821 | 21.319 |
| CLINO | 58 | 55.6 | | 2.2 | 2.55 | 1.159 | 18.875 |
| CLINO | 47 | 111.5 | | 3.2 | 2.68 | 0.838 | 18.711 |
| UNDA | 87 | 302.4 | | 2.96 | 2.89 | 0.976 | 9.524 |
| UNDA | 8 | 303.0 | | 2.71 | 2.57 | 0.948 | 15.006 |
| UNDA | 81 | 137.7 | micro-porosity | 4.39 | 3.63 | 0.827 | 3.428 |
| UNDA | 83 | 141.5 | | 4.35 | 3.41 | 0.784 | 6.042 |
| UNDA | 82 | 200.0 | | 4.43 | 3.53 | 0.797 | 1.976 |
| CLINO | 25 | 236.2 | | 3.83 | 4.04 | 1.055 | 2.495 |
| CLINO | 27 | 291.3 | | 5.32 | 4.34 | 0.816 | 0.934 |
| CLINO | 50 | 317.9 | | 3.65 | 3.79 | 1.038 | 2.058 |
| CLINO | 28 | 330.6 | | 5.29 | 5.63 | 1.064 | 1.648 |
| UNDA | 90 | 354.1 | | 5.85 | 4.31 | 0.737 | 1.218 |
| UNDA | 91 | 357.9 | | 5.22 | 4.12 | 0.789 | 0.957 |
| CLINO | 32 | 510.5 | | 5.3 | 4.73 | 0.892 | 3.067 |
| CLINO | 69 | 528.2 | | 4.7 | 4.62 | 0.983 | 2.555 |
| CLINO | 68 | 535.3 | | 4.8 | 4.26 | 0.888 | 2.749 |
| CLINO | 33 | 535.9 | | 5.31 | 4.67 | 0.879 | 1.665 |
| CLINO | 53 | 548.0 | | 4.85 | 4.12 | 0.849 | 1.138 |
| CLINO | 34 | 605.3 | | 4.91 | 4.28 | 0.872 | 1.711 |
| CLINO | 35 | 623.6 | | 5.3 | 4.61 | 0.870 | 2.072 |
| CLINO | 70 | 624.8 | | 5.84 | 4.85 | 0.830 | 1.698 |
| CLINO | 71 | 656.8 | | 5.59 | 3.25 | 0.581 | 5.74 |
| CLINO | 74 | 665.6 | | 5.07 | 4.88 | 0.963 | 2.22 |
| CLINO | 73 | 675.7 | | 5.01 | 3.5 | 0.699 | 1.799 |

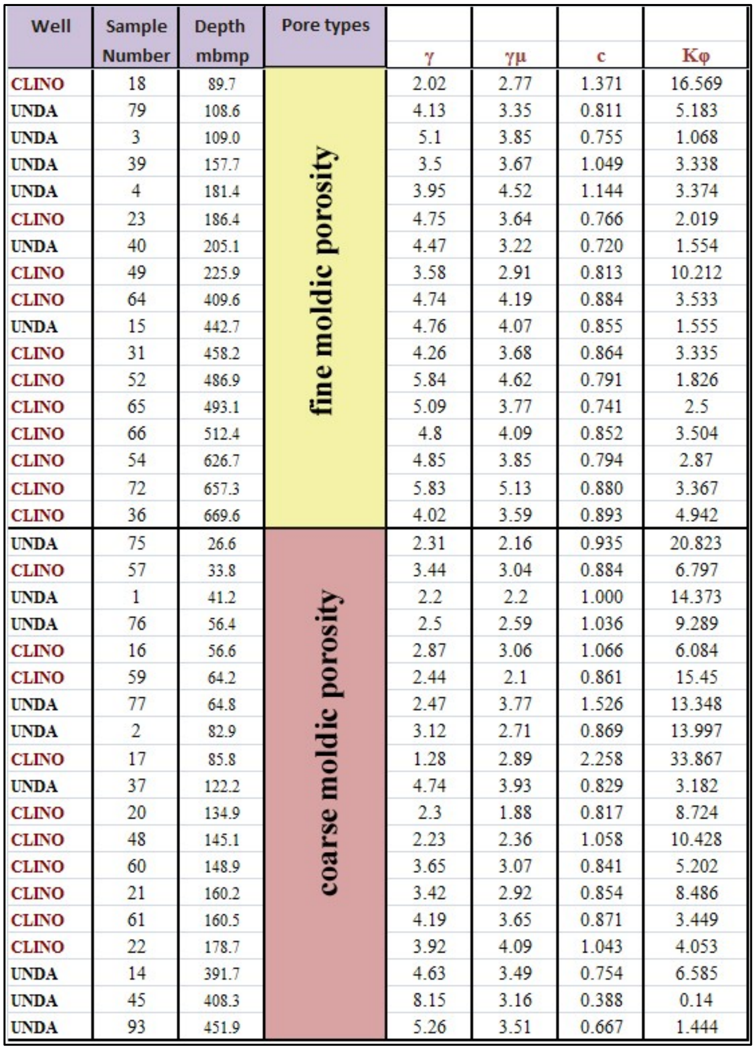

| Well | Sample Number | Depth mbmp | Pore types | $\gamma$ | $\gamma\mu$ | $c$ | $K\varphi$ |
|---|---|---|---|---|---|---|---|
| CLINO | 18 | 89.7 | fine moldic porosity | 2.02 | 2.77 | 1.371 | 16.569 |
| UNDA | 79 | 108.6 | | 4.13 | 3.35 | 0.811 | 5.183 |
| UNDA | 3 | 109.0 | | 5.1 | 3.85 | 0.755 | 1.068 |
| UNDA | 39 | 157.7 | | 3.5 | 3.67 | 1.049 | 3.338 |
| UNDA | 4 | 181.4 | | 3.95 | 4.52 | 1.144 | 3.374 |
| CLINO | 23 | 186.4 | | 4.75 | 3.64 | 0.766 | 2.019 |
| UNDA | 40 | 205.1 | | 4.47 | 3.22 | 0.720 | 1.554 |
| CLINO | 49 | 225.9 | | 3.58 | 2.91 | 0.813 | 10.212 |
| CLINO | 64 | 409.6 | | 4.74 | 4.19 | 0.884 | 3.533 |
| UNDA | 15 | 442.7 | | 4.76 | 4.07 | 0.855 | 1.555 |
| CLINO | 31 | 458.2 | | 4.26 | 3.68 | 0.864 | 3.335 |
| CLINO | 52 | 486.9 | | 5.84 | 4.62 | 0.791 | 1.826 |
| CLINO | 65 | 493.1 | | 5.09 | 3.77 | 0.741 | 2.5 |
| CLINO | 66 | 512.4 | | 4.8 | 4.09 | 0.852 | 3.504 |
| CLINO | 54 | 626.7 | | 4.85 | 3.85 | 0.794 | 2.87 |
| CLINO | 72 | 657.3 | | 5.83 | 5.13 | 0.880 | 3.367 |
| CLINO | 36 | 669.6 | | 4.02 | 3.59 | 0.893 | 4.942 |
| UNDA | 75 | 26.6 | coarse moldic porosity | 2.31 | 2.16 | 0.935 | 20.823 |
| CLINO | 57 | 33.8 | | 3.44 | 3.04 | 0.884 | 6.797 |
| UNDA | 1 | 41.2 | | 2.2 | 2.2 | 1.000 | 14.373 |
| UNDA | 76 | 56.4 | | 2.5 | 2.59 | 1.036 | 9.289 |
| CLINO | 16 | 56.6 | | 2.87 | 3.06 | 1.066 | 6.084 |
| CLINO | 59 | 64.2 | | 2.44 | 2.1 | 0.861 | 15.45 |
| UNDA | 77 | 64.8 | | 2.47 | 3.77 | 1.526 | 13.348 |
| UNDA | 2 | 82.9 | | 3.12 | 2.71 | 0.869 | 13.997 |
| CLINO | 17 | 85.8 | | 1.28 | 2.89 | 2.258 | 33.867 |
| UNDA | 37 | 122.2 | | 4.74 | 3.93 | 0.829 | 3.182 |
| CLINO | 20 | 134.9 | | 2.3 | 1.88 | 0.817 | 8.724 |
| CLINO | 48 | 145.1 | | 2.23 | 2.36 | 1.058 | 10.428 |
| CLINO | 60 | 148.9 | | 3.65 | 3.07 | 0.841 | 5.202 |
| CLINO | 21 | 160.2 | | 3.42 | 2.92 | 0.854 | 8.486 |
| CLINO | 61 | 160.5 | | 4.19 | 3.65 | 0.871 | 3.449 |
| CLINO | 22 | 178.7 | | 3.92 | 4.09 | 1.043 | 4.053 |
| UNDA | 14 | 391.7 | | 4.63 | 3.49 | 0.754 | 6.585 |
| UNDA | 45 | 408.3 | | 8.15 | 3.16 | 0.388 | 0.14 |
| UNDA | 93 | 451.9 | | 5.26 | 3.51 | 0.667 | 1.444 |

# VITA

Name: Elnara Mammadova

Address: Department of Geology
c/o Dr. Yuefeng Sun
Texas A&M University
College Station, Texas 77843-3115

Email Address: elnara.mammadova@gmail.com

Education: B.S., Geophysics, Azerbaijan State Oil Academy, 2008